Thermo-mechanical and fracture assessment by FE modeling for the critical components of the DEMO nuclear fusion reactor

Alessandro Cuccurullo

UNIVERSITY OF SALERNO

DEPARTMENT OF INDUSTRIAL ENGINEERING

Ph.D. Course in Industrial Engineering
Curriculum in Mechanical Engineering - XXXVIII Cycle

Thermo-mechanical and fracture assessment by FE modeling for the critical components of the DEMO nuclear fusion reactor

Supervisor
Prof. Roberto Citarella

Ph.D. student
Alessandro Cuccurullo

Scientific Referees
Prof. Jeong-Ha You
Prof. Stefano Valvano
Ph.D. Course Coordinator
Prof. Massimo De Santo

Sommario

Abbreviations

A	Area
BB	Breeding Blanket
BC	Boundary conditions
CAD	Computer Aided Design
DEMO	DEMOnstration power plant
EM	Electromagnetic
FE	Finite element
HKM	Hybrid Kinematic Manipulator
IC	Initial conditions
IVT	Inner vertical target
ITER	International thermonuclear experimental reactor
LEFM	Linear elastic fracture mechanics
MPS	Maximum principal stress
NoC	Normal operating conditions
OVT	Outer vertical target
RM	Remote Maintenance
SIF	Stress intensity factor
VV	Vacuum vessel
VDE	Vertical disruption event
h	Film coefficient / hour

Abstract

Nuclear fusion represents one of the most promising pathways toward sustainable, large-scale, and low-impact energy production. However, the extreme operational conditions within fusion reactors, characterized by elevated temperatures, intense neutron irradiation, and severe mechanical and magnetic loads, pose significant challenges for the structural integrity and long-term reliability of reactor components.

This doctoral work has been developed along two complementary and parallel research lines, conducted respectively within the academic framework of the University of Salerno and in collaboration with the engineering company LT Calcoli as part of an industrial partnership.

Within the academic research, the focus was placed on fracture mechanics applied to the divertor of the *DEMO (DEMOnstration power plant)* fusion reactor, one of its most critical structural components. A comprehensive finite element (*FE*) model was developed to capture the thermo-mechanical response of the divertor under realistic operating loads. Using submodeling and Linear Elastic Fracture Mechanics (*LEFM*) approaches, stationary semi-elliptical cracks were introduced to assess stress intensity factors (*SIFs*) and identify the most critical regions. The study was further extended to simulate crack propagation under multi-step loading conditions, allowing fatigue life estimation through Paris' law and the prediction of the number of cycles required to reach critical crack sizes. Additionally, a multi-crack growth analysis was performed to investigate the simultaneous presence of two cracks located in adjacent critical regions. Finally, an elastoplastic material model was implemented to evaluate the deviation of the structural response from the

linear elastic assumption. The obtained results identified the most vulnerable divertor zones and demonstrated the sensitivity of crack growth to thermal gradients and combined loading effects.

In parallel, the industrial research conducted with LT Calcoli focused on the thermo-mechanical design and analysis of a robotic arm intended for the maintenance of the *DEMO* Breeding Blanket, operating under severe thermal conditions. The study assessed the structural response of the manipulator to high heat conductive and convective fluxes originating respectively from the Blanket and the surrounding environment and explored design and material optimization strategies to enhance heat resistance and achieve a more uniform temperature distribution.

Beyond the specific results obtained in each research line, the original contribution of this work lies in the development of an integrated methodology for assessing the structural integrity of fusion reactor components under realistic operational conditions. The combined use of the submodeling techniques, fracture mechanics and lifetime assessment analyses establishes a predictive framework capable of capturing complex loading interactions and realistic operating conditions more accurately than conventional approaches.

The integration of these two research directions yields a comprehensive contribution to the structural safety, durability, and maintainability of next-generation fusion reactors, supporting their reliable and sustainable development.

INTRODUCTION

The growing instability of global energy markets, accentuated by geopolitical crises and disruptions in supply chains, has highlighted the need for a secure, sustainable, and resilient energy system. The volatility of fossil fuel prices and concerns about energy security further underscore the urgency of transitioning toward alternative energy sources that are reliable and environmentally sustainable [1]. The surge in oil and gas prices, together with concerns about the availability of natural resources, has led many countries to reconsider their energy policies and to seek solutions that reduce dependence on non-renewable sources.

Moreover, as highlighted in global reports on the future of energy, the rapid economic and demographic growth expected in the coming decades will result in a significant increase in energy demand [2]. Developing nations, with their growing need for electricity to power industry, transportation, and housing, face the challenge of ensuring access to abundant and clean energy without compromising the environment or citizens' health. This makes the search for clean and plentiful energy sources a crucial challenge for the planet's future.

In this context, nuclear fusion emerges as one of the most promising solutions. Unlike nuclear fission, which is currently used in conventional nuclear power plants, nuclear fusion does not produce long-lived radioactive waste and does not involve the related risks associated with managing nuclear waste. Furthermore, fusion has the potential to provide a virtually unlimited supply of energy, harnessing the most abundant and easily accessible fuels, such as the hydrogen isotope deuterium, which can be extracted from seawater [3]. This could significantly reduce dependence on finite mineral resources such as coal, gas, and uranium, and contribute to greater global energy security.

Nuclear fusion could also have a significant impact on combating climate change, as it provides a carbon-free source of energy capable of supporting growing energy demand without contributing to global warming. If fusion technologies manage to overcome the existing technical and economic challenges, they could radically transform the global energy landscape,

contributing to greater diversification of energy sources, higher price stability, and reduced greenhouse gas emissions.

Ongoing research in this field, such as that being conducted at the *International Thermonuclear Experimental Reactor* (*ITER*) project in France [4], is crucial to moving closer to commercial nuclear fusion. Although we are still far from achieving practical large-scale fusion, technological developments in recent years have been encouraging. Advances in materials resistant to high temperatures, magnetic confinement systems, and plasma management suggest that within the next few decades, we may be able to harness this energy source efficiently and safely.

Nuclear fusion, therefore, is not only a promise for the future but an urgent necessity for building an energy system that meets the global challenges of sustainability and security. With the support of targeted government policies and investments in research and development, nuclear fusion could become one of the keys to solving the global energy crisis and ensuring a more sustainable future for generations to come. However, harnessing fusion energy on an industrial scale presents significant scientific and engineering challenges that must be addressed to ensure its feasibility as a commercial energy source.

Nuclear fusion, the process that powers the sun and other stars, involves the merging of light atomic nuclei, typically isotopes of hydrogen such as deuterium and tritium, to form heavier elements, releasing enormous amounts of energy in the process. This reaction occurs naturally under the extreme temperatures and pressures found in stellar cores. Reproducing these conditions on Earth represents a formidable challenge, as it requires reaching temperatures exceeding 100 million degrees Celsius, high enough to overcome the natural repulsion between positively charged nuclei. Achieving such temperatures is a crucial milestone but also presents tremendous engineering difficulties.

At these extreme temperatures, matter exists in the form of plasma, an ionized state in which atoms are separated into their fundamental components, electrons and nuclei. This plasma must be confined in such a way that particles can collide frequently enough for fusion to occur, while preventing contact with the reactor walls, which would cool the plasma and dissipate its energy.

To achieve this, scientists create a state of matter known as plasma, in which atoms are ionized, separating electrons from nuclei and generating a collection of charged particles that can be controlled by magnetic fields. The challenge lies in developing an effective magnetic confinement system

capable of withstanding the extreme temperature and instability conditions of plasma. Magnetic confinement reactors, such as *tokamaks [5]*, use powerful magnetic fields to trap the plasma in a doughnut-shaped configuration. However, maintaining plasma stability for extended periods remains a major challenge, as even slight instabilities can cause plasma loss and potentially damage the reactor.

In addition to magnetic confinement, continuous heating mechanisms are required to reach and sustain the necessary plasma temperature. These techniques further increase the plasma's temperature but also add complexity to reactor design and operation. Moreover, as the plasma approaches the required temperature, it must be kept stable long enough for a controlled fusion reaction to occur. This demands sophisticated feedback systems capable of rapidly adjusting magnetic fields and heating parameters in real time.

The goal is to contain and stabilize the plasma long enough for fusion reactions to take place, producing energy that can be efficiently harnessed. This involves developing solutions to manage the immense heat and energy generated by fusion, which far exceed those produced by traditional energy sources. Designing materials capable of withstanding such extreme heat and radiation represents another major engineering challenge.

The potential of nuclear fusion lies in its ability to provide a virtually inexhaustible and clean source of energy, producing zero greenhouse gas emissions and minimal radioactive waste.

However, achieving these technological milestones requires not only overcoming scientific challenges but also developing robust engineering solutions that can scale fusion reactors for commercial energy production.

The work carried out during the Ph.D. years focused on the structural and thermo-mechanical performance assessment of components within the *DEMO* fusion reactor, with particular emphasis on the divertor and remote maintenance systems for Breeding Blanket sectors. The study addressed key challenges related to high thermal, mechanical, and electromagnetic loads, as well as the extreme conditions that structural materials must withstand over the operational lifetime of the reactor.

The main objectives of this thesis are collocated within this scenario. On one hand, the research aimed to investigate the fracture behavior of the DEMO divertor under various loading conditions, including pressure, thermal, electromagnetic, and combined loads, with the goal of predicting crack nucleation points, growth, and the component lifetime. On the other hand, the

thesis focused on the design and analysis of remote maintenance systems for the breeding blanket, evaluating their thermal performance under steady-state and transient conditions.

The scientific and technological motivations for this work stem from the need to ensure safe, efficient, and long-lasting operation of *DEMO* components exposed to extreme environments. The divertor, as a plasma-facing component, experiences high thermal fluxes and particle loads, while structural and cooling systems must maintain integrity and performance over extended periods. Similarly, the remote maintenance systems play a critical role in reactor operation, enabling maintenance and replacement of components without compromising safety or operational continuity.

The thesis is structured as follows: after this introduction, Chapter 1 provides an initial overview of the *DEMO* reactor and its main components. Chapter 2 presents the adopted *FE DEMO* divertor configuration, including loading conditions, material properties, and boundary conditions. Chapters 3, 4, and 5 detail the static crack analysis, crack growth assessment, and lifetime evaluation, respectively, while Chapters 6 and 7 focus on multiple crack effects and plastic material modeling, performed to validate the results previously obtained within the *LEFM* framework.

Chapter 8 describes the schematization of the Remote Maintenance problem, characterizing the second part of this thesis work, and Chapter 9 addresses the design and analysis of the remote maintenance systems for the *DEMO* breeding blanket, including theoretical and numerical models, FE simulations, model validation, sensitivity analyses, and preliminary results. Chapter 10 reports the first results obtained for the simplified structure after model validation, and Chapter 11 presents the results for the real, more complex 3D structure.

1. The DEMO project

In the pursuit of sustainable fusion energy, *EUROfusion*, the European consortium dedicated to nuclear fusion research, plays a crucial role in driving the development of fundamental scientific and technological advancements. The strategic plan of the consortium outlines the essential steps for the transition from experimental fusion to commercial fusion [6], defining a progressive and well-structured roadmap to achieve fusion reactors capable of generating energy at an industrial scale. The first major milestone of this plan is the completion of the *ITER* reactor, *Figure 1* [7], a facility designed to demonstrate that nuclear fusion can indeed provide a reliable and sustainable source of energy. *ITER*, representing an unprecedented scientific and engineering endeavor, is expected to operate for about two decades, during which it will serve as a testbed for the principles and technologies that will be fundamental to future fusion reactors [8]. Over this period, *ITER* will provide crucial data and insights to refine plasma confinement techniques, manage materials exposed to intense radiation, and control nuclear fusion reactions, thus creating a vital knowledge base for the next steps.

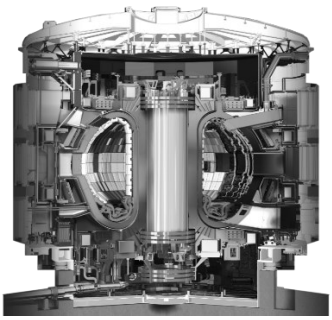

Figure 1 – ITER nuclear reactor detail

1.1 DEMO reactor overview

The experience gained with *ITER* will directly guide the subsequent development of the European Demonstration Reactor, better known as *DEMO* (*Figure 2*, [9]). This represents the next decisive step toward achieving nuclear fusion on a commercial scale. The *DEMO* reactor will be the first fusion plant capable of generating *net energy*, that is, producing more energy than it consumes, and feeding it into the electrical grid. This achievement is fundamental to demonstrate not only the scientific feasibility of fusion but also its economic viability.

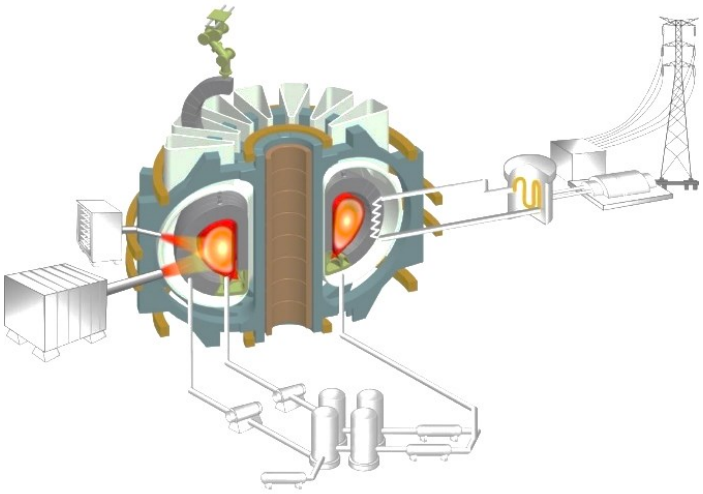

Figure 2 – DEMO power plant idea

The realization of *DEMO* will require detailed design work and careful evaluation of engineering solutions—from reactor architecture to plasma control and management technologies, to energy production and distribution systems. Its construction and operational startups are expected by the end of the century, representing a milestone toward the adoption of nuclear fusion as a primary, reliable, and clean energy source.

Beyond its construction and operation, the *DEMO* program will include a series of advanced experiments and tests to optimize reactor design and address the complex challenges that will emerge during the transition to large-scale production. This phase will demand vast resources and international collaboration, with continuous investment in research, development, and innovation. The ultimate goal is to make nuclear fusion a safe, economical, and sustainable energy source for the future, one that can significantly reduce greenhouse gas emissions and ensure a global energy supply capable of meeting the challenges of increasing demand.

The DEMO project

The realization of *DEMO* will be the culmination of decades of research and development, but its implications are immense. This facility will not only demonstrate the technical feasibility of nuclear fusion on a commercial scale but will also serve as a cornerstone for the future energy industry. With appropriate policies and sustained public and private investment, the success of *DEMO* could mark a turning point in the transition to a new era of clean and abundant energy, helping to ensure global energy security and environmental sustainability for future generations.

1.2 Advanced materials in fusion reactors

The development and characterization of structural materials capable of withstanding the extreme environments within fusion reactors are crucial for ensuring both efficiency and longevity. Fusion reactors, particularly those based on magnetic confinement, such as tokamaks, operate under conditions far more severe than conventional energy systems (*Figure 3*, [10]). The plasma inside the reactor reaches temperatures exceeding 100 million degrees Celsius, while surrounding components are subjected to high thermal loads, intense neutron irradiation, and significant mechanical stresses.

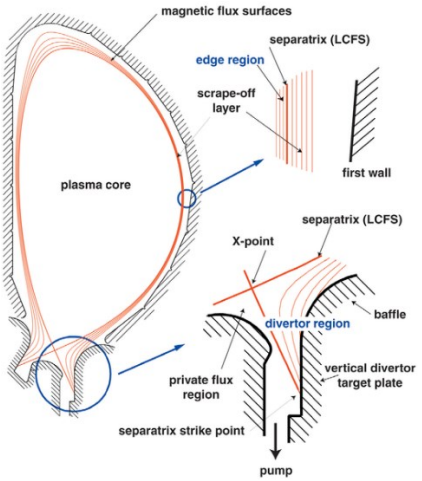

Figure 3 – Poloidal cross-section of a DEMO tokamak plasma

These extreme conditions pose unique challenges for the materials that make up the reactor's structural components, imposing stringent requirements in terms of strength, durability, and the ability to maintain performance over time. Among the key components (*Figure 4*) subjected to the most critical thermal and mechanical stresses are the first wall of the breeding blanket and the divertor.

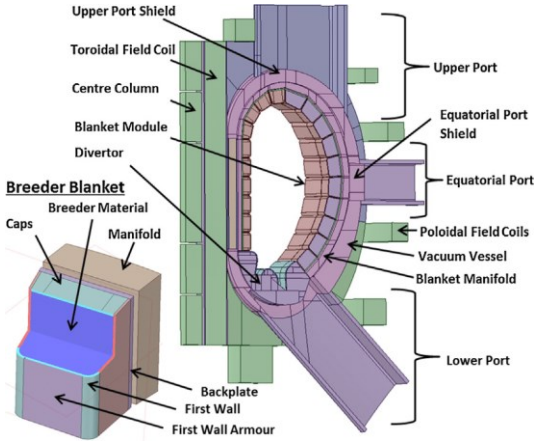

Figure 4 – DEMO reactor main components

Each of these components faces extremely demanding conditions that require innovative and highly resilient materials.

The first wall (*Figure 4*, [11]) serves as the initial barrier between the plasma and the reactor structure. Directly exposed to intense heat fluxes and high-energy particles, including neutrons, the first wall must withstand extreme heat without degradation. It must also resist the damaging effects of neutron irradiation, which can cause atomic displacements and material weakening over time.

The breeding blanket (*Figure 4*) is the component positioned directly behind the first wall and plays a crucial role in both energy conversion and fuel production. Its primary function is to breed tritium, one of the fuels required for fusion reactions, through interactions with the high-energy neutrons generated in the plasma. Additionally, the blanket absorbs a significant portion of the thermal energy released during fusion, transferring it to the cooling system for power generation. The materials used in the breeding blanket must therefore combine neutron multiplication, thermal conductivity, and structural resilience, ensuring long-term reliability under intense irradiation, high thermal loads, and mechanical stresses.

Currently, materials such as tungsten and carbon-based composites are at the center of research efforts, as they exhibit promising thermal and irradiation-resistant properties. Tungsten, for example, is known for its high heat resistance and low sputtering rate (loss of particles under bombardment), while carbon composites offer advantages in heat management and durability, though they still require improvement to better withstand neutron impacts.

The DEMO project

The divertor (*Figure 5*, [12]) is an essential component designed to remove excess heat and particles from the plasma, diverting them away from sensitive areas of the reactor. This part of the system is subjected to thermal fluxes far greater than those experienced by the first wall, often exceeding temperatures of 1000°C. Due to these extreme conditions, the divertor also undergoes rapid thermal cycling, which can cause thermal fatigue and material degradation. Therefore, thermal fatigue resistance is a key property for divertor materials, alongside the ability to resist damage caused by high-energy neutrons produced during fusion reactions. Materials used in the divertor must endure repeated heating and cooling cycles without compromising their structural integrity [13,14,15]. In modern designs, Eurofer97, a reduced-activation ferritic-martensitic (RAFM) steel, is increasingly used in structural subcomponents of the divertor, replacing the previously considered AISI 316L. This substitution is motivated by Eurofer97's lower neutron-induced activation, better resistance to swelling and irradiation damage, and its ability to maintain mechanical strength and dimensional stability under high neutron fluxes, making it more suitable for DEMO divertor components exposed to intense radiation and thermal loads. [16]. The use of advanced refractory materials, such as carbon-based composites or high-strength metal alloys, is a critical area of study aimed at improving the durability and reliability of these components under thermal and mechanical stress [17].

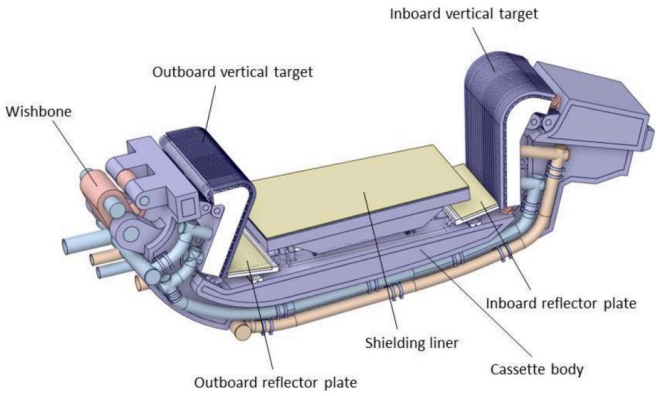

Figure 5 – DEMO Divertor scheme

1.3 Nuclear irradiation and impact on materials

Another major concern involves the impact of neutron irradiation. Fusion reactions generate high-energy neutrons that interact with materials, causing atomic displacements, hardening, and embrittlement [18]. This radiation damage is one of the main challenges, as it can significantly reduce the lifespan of materials used in the first wall, divertor, and other reactor

components. Neutron irradiation can also alter mechanical properties such as strength and toughness, thereby compromising reactor safety and reliability. To address these issues, it is essential to develop advanced materials capable of withstanding such damage without compromising overall performance. Radiation-resistant metal alloys, ceramic matrix composites, and carbon-based materials designed to resist radiation-induced degradation are rapidly evolving fields of research.

1.4 Sustainability and material innovation

To ensure that fusion reactors can operate safely and efficiently over extended periods, careful selection and engineering of structural materials are essential. Research focuses on advanced alloys, composites, and ceramics that not only resist heat and radiation but also provide long operational lifespans, minimizing the need for maintenance and frequent replacement. Furthermore, research into cooling and thermal management technologies is crucial to ensure that reactor components can endure extreme thermal stresses without compromising system efficiency. In summary, the development of materials resistant to neutron irradiation, thermal, and mechanical stresses is one of the most critical challenges for the success of nuclear fusion as a sustainable energy source. Overcoming these challenges will require continuous innovation, investment in research and development, and strong international collaboration to ensure that fusion reactors can operate safely, efficiently, and reliably over time.

Chapter 1

PART 1:

DIVERTOR FRACTURE

ASSESSMENT

2.Adopted divertor configuration

2.1 DEMO divertor loading conditions

The divertor is one of the key components of a nuclear fusion reactor, serving to re-move the heat generated by the plasma through the fluid refrigerant system. Under these conditions, the divertor is subjected to multiple types of loads, including:

• Thermal loads, due to the particle and radiative flux from the plasma;

• Internal pressure loads, generated by the coolant circulating in the cooling circuits that maintain component temperature stability;

• Electromagnetic (*EM*) loads, arising from plasma currents and confinement magnetic fields;

• Neutron irradiation, which induces material damage;

• Swelling, i.e., material expansion caused by radiation damage.

The adopted *DEMO* divertor configuration features two separate coolant circuits [*19,20*], with the following operating pressures: 5 MPa for the Inner and Outer Vertical Targets (*IVT* and *OVT*), and 15.5 MPa for the other components (*Figure 6*).

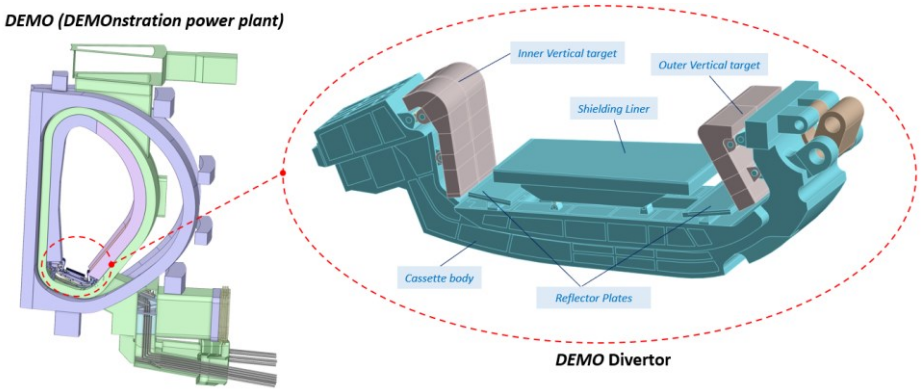

Figure 6 – DEMO divertor components

The analysis begins with a global model of the divertor, in which pressure, thermal and *EM* loads are applied independently:

- In the pressure load case, the stress scenario produced on the vertical target by the refrigerant fluid pressure, equal to 5 MPa, is analyzed (*Figure 7*).

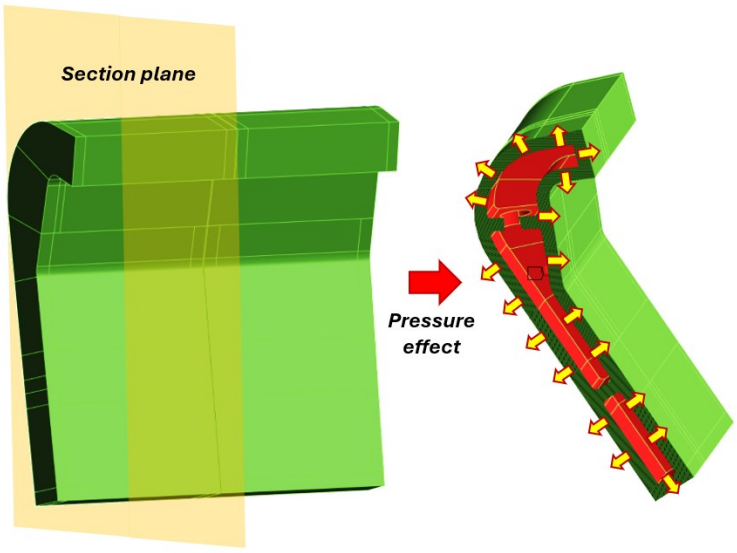

Figure 7 - Pressure due to the refrigerant system

During the thermal load case, the nodal temperatures obtained from a thermo-fluid dynamics analysis at the *Normal Operating Conditions* (*NoC*) [19] are applied as thermal loads (*Figure 8*). These temperatures were first computed through a dedicated thermo-fluid dynamic simulation and

subsequently exported in terms of nodal temperature distributions. The resulting temperature maps were then imported into the structural finite element model and applied at the corresponding spatial coordinates.

Due to the unavoidable differences between the meshes used in the thermo-fluid dynamic and structural analyses, the respective nodal locations did not coincide exactly. Therefore, a mapping procedure based on a "weighted triangulation" interpolation was employed by *Ansys Workbench* to transfer the thermal field from the source mesh to the target structural mesh.

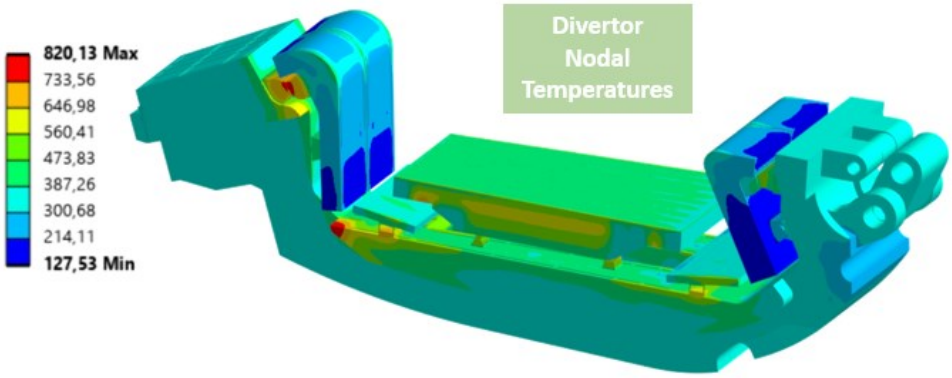

Figure 8 – Nodal temperatures [°C] applied in the thermal load case

During a vertical disruption event (*VDE*), a plasma instability in which the plasma column rapidly moves in the vertical direction and loses confinement, the divertor assembly is subjected to significant induced Lorentz forces. The time evolution of these resultant forces acting on the divertor assembly is taken from Ref. [21].

The critical time instant is defined as the load step at which the resultant Lorentz force on the divertor reaches its maximum value. The nodal forces and their corresponding coordinates were subsequently extracted and used in the following analyses. A resume of the applied loads in the two analyses is reported in *Table 1*:

LOAD CASE	*IVT Pressure loads*	*IVT Thermal loads*	*IVT EM loads*
Pressure	5 MPa	No thermal loads	No *EM* loads
Thermal	No pressures	Nodal Temperatures extracted by [20]	No *EM* loads

EM	No pressures	No thermal loads	Nodal forces extracted by [21]
Combined	5 MPa	Nodal Temperatures extracted by [20]	No *EM* loads

Table 1 – Scheme of the loads applied in the two studied analyses

2.2 Materials

The support brackets, the cassette body, the reflector plates together with the *OVT* and the *IVT* are made of *Eurofer97* (*Figure 9*), whose properties are taken from *RCC-MRx* [22]. The *Inconel 718* elastic material, whose mechanical properties are taken from *SDC-IC* [23], is used for the support links. The connection between the vertical target body and the cassette body is achieved through support brackets, pins, and links: both the *IVT* and *OVT* supports consist of two rows of brackets, one set attached to the target body and the other attached to the cassette side; these are connected via matching pins and links. A general joint is defined between the faces of the support bracket and the pin to prevent reciprocal sliding.

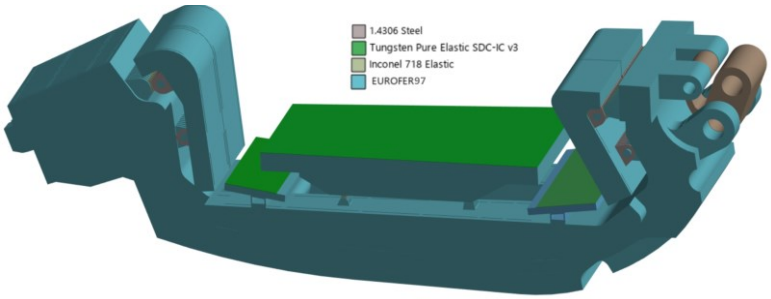

Figure 9 – Adopted materials and details of the IVT connections

2.3 Boundary conditions

In the global model, two boundary conditions are applied (*Figure 10*):

- A fixed support is assigned to the two ‘noses’ of the cassette body.
- An initial displacement is imposed on the wishbone to simulate a pre-load [24] equal to 100 kN (acting in the direction of the red line).

Adopted divertor configuration

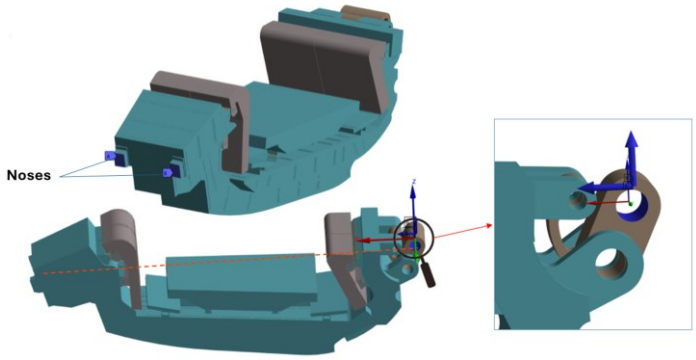

Figure 10 – Global boundary conditions details

3.Static crack analysis

In order to rigorously analyze crack propagation within the components of the divertor, it is necessary to introduce the theoretical foundations of Linear Elastic Fracture Mechanics, a discipline that allows for the description and quantification of the behavior of materials containing defects under linear elastic conditions. This theory assumes that, even in the presence of discontinuities, the surrounding material behaves in an elastic and linear manner.

Subsequently, based on the theoretical foundations just introduced, the numerical operations performed on the *FE* model of the component will be described in detail. In particular, the procedure for introducing static cracks within the *FE* sub-models using the *FRANC3D* software will be illustrated, and the local response of the material will be analyzed in terms of the distribution of the stress intensity factor K. This approach makes it possible to accurately evaluate the behavior of the component in the presence of initial defects, simulating realistic operating scenarios. The same steps are followed by Giannella et al. [25], who adopted a LEFM-based crack propagation framework using the software ABAQUS in combination with FRANC3D to model crack initiation and growth scenarios in welded steel joints, demonstrating the effectiveness of this approach in capturing long crack propagation phases.

3.1 Concepts of linear elastic fracture mechanics

One of the fundamental aspects of *LEFM* is the description of stress concentration near the crack tip, an area where, according to classical elasticity theory, stresses theoretically tend to infinity. To overcome this limitation, *LEFM* introduces the concept of the Stress Intensity Factor (*SIF*),

which provides a quantitative measure of the singularity of the stress field around the crack.

The *SIF*, commonly denoted as K, depends on the geometry of the component, the loading configuration, and the crack length, and it is divided into three main modes of crack opening:

Mode I (opening mode – tensile opening): the most relevant in practical applications, where the crack faces move apart due to a normal tensile stress.

Mode II (sliding mode – in-plane shear): where the crack opens due to a tangential shear stress.

Mode III (tearing mode – out-of-plane shear): associated with shear stresses perpendicular to the crack plane.

In the context of *LEFM*, the behavior of the material near the crack tip can be analytically described through the Westergaard and Irwin solutions, which are derived from the equations of plane elasticity. In the presence of a crack, a stress singularity arises approaching the crack tip.

For Mode I (opening perpendicular to the crack plane), the stress field near the crack tip can be expressed in polar coordinates by eqs. (1-3):

$$\sigma_{xx}(r,\theta) = \frac{K_I}{\sqrt{2\pi r}} cos\left(\frac{\theta}{2}\right)\left[1 - sin\left(\frac{\theta}{2}\right) sin\left(\frac{3\theta}{2}\right)\right] \quad (1)$$

$$\sigma_{yy}(r,\theta) = \frac{K_I}{\sqrt{2\pi r}} \cos\left(\frac{\theta}{2}\right)\left[1 + \sin\left(\frac{\theta}{2}\right) \sin\left(\frac{3\theta}{2}\right)\right] \quad (2)$$

$$\tau_{xy}(r,\theta) = \frac{K_I}{\sqrt{2\pi r}} \sin\left(\frac{\theta}{2}\right) \cos\left(\frac{\theta}{2}\right) \cos\left(\frac{3\theta}{2}\right) \quad (3)$$

where,

- K_I is the Mode I Stress Intensity Factor;
- $r \rightarrow 0$ represents the region near the crack tip, where stresses theoretically diverge;
- θ is the angle with respect to the crack axis.

These expressions show that the stresses behave as $\sigma \sim 1/\sqrt{r}$, highlighting the singularity around the crack tip. However, the *LEFM* approach is considered valid only as long as local plastic deformation (at crack tip) remains confined and does not extend beyond a certain region.

A simplified form for classical cases (such as a central crack in an infinite plate under uniform tension) is given by eq. (4):

$$K_I = \sigma\sqrt{\pi a} \tag{4}$$

In real and more complex geometries, the value of K is corrected by a geometric factor Y (eq. (5)), which can be determined analytically, experimentally, or through *FE* simulation:

$$K_I = \mathrm{Y} \cdot \sigma\sqrt{\pi a} \tag{5}$$

The crack is considered stable as long as (eq. (6)):

$$K_I < \mathrm{K_{IC}} \tag{6}$$

where K_{IC} is the fracture toughness of the material, the critical value beyond which unstable crack propagation occurs. This property is experimentally determined and represents a fundamental design limit.

The main objective of the analysis is to study the variability of stress intensity factor K as a function of different geometric and loading parameters. In particular, the goal is to investigate the evolution of K with respect to changes in crack length, orientation relative to the principal stress field, and location within the component.

This parametric analysis makes it possible to identify the most critical configurations for crack propagation and provides a quantitative framework for assessing the component's sensitivity to the presence of initial defects under realistic operating conditions.

3.2 Analysis workflow

The present study addresses the structural analysis of an extremely complex component, the divertor, a key element in fusion reactors, subjected to particularly severe loading conditions. The divertor is modeled in its entirety through a *FE* analysis, which includes all its structural subcomponents: the vertical target supports, reflector plates, shielding liner, wishbone, cassette body, and nose. The primary objective is to gain a highly detailed understanding of the behavior of these components under the combined action of various loads. The loads considered in the global model include electromagnetic stresses, thermal loads, and internal mechanical pressures. The global *FE* analysis provides a comprehensive overview of the stress state within the divertor, thereby allowing the identification of

potentially critical areas that are more susceptible to crack initiation and propagation.

Based on the global results, the submodeling technique is then applied to isolate the critical components and analyze them with higher local resolution, while maintaining mechanical consistency with the global model through the application of appropriate boundary conditions. This phase serves a dual purpose: on the one hand, it enables detailed investigation of geometrical features and local load distributions; on the other, it establishes the foundation for the fracture analysis itself.

On these sub-models, an external procedure is implemented using the *FRANC3D* software, specifically designed for fracture mechanics analysis. In this initial stage, static cracks are introduced, modeled with semi-elliptical geometries of varying orientations and dimensions (*Figure 11*), in correspondence to the areas identified as critical. The analysis focuses on calculating the Stress Intensity Factor (*SIF*), a key parameter in Linear Elastic Fracture Mechanics (*LEFM*), as it quantifies the local stress field at the crack tip. The *SIF* value provides crucial information on the crack's severity and its tendency to propagate under a given load.

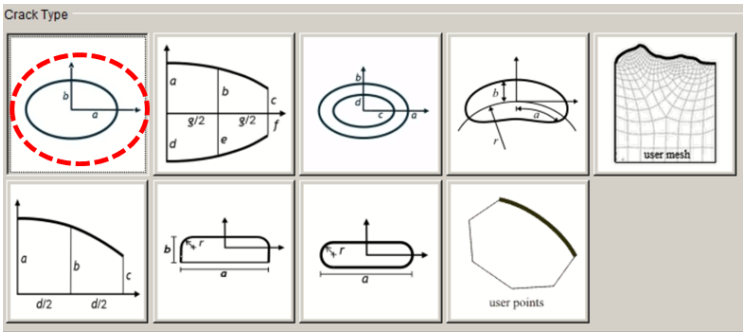

Figure 11 - Crack types that can be analyzed using FRANC3D

This process is carried out in particular on the *IVT* of the divertor, across different load cases, mechanical, thermal, electromagnetic, and combined pressure-thermal, while varying the position and orientation of the introduced cracks.

By applying this approach to each component of the divertor, it is possible to construct a highly detailed overall picture of the divertor's fracture response and that of its individual subsystems. This provides fundamental insights for the design, maintenance, and long-term reliability of the entire system.

3.3 Analyzed configurations

This chapter presents the results of the fracture analysis conducted on *IVT* of the divertor. As a preliminary step, the results from the global *FE* model corresponding to the considered load case were examined in order to identify the critical regions of the component where significant peaks of the calculated principal stresses occur. These areas represent potential crack initiation sites and were therefore selected as locations for the insertion of semi-elliptical cracks within the corresponding sub-models.

Assuming crack nucleation at critical points, once these points are identified, cracks are introduced and their growth evaluated, followed by a simplified fatigue analysis. To achieve greater accuracy in the study of individual components without significantly increasing computation times, the submodeling technique is employed. This methodology, in the field of the structural integrity [26], allows for a locally refined mesh by focusing on a single component, enhancing result resolution and enabling detailed analysis of subcomponents.

3.3.1 Pressure load case

From the global analysis, the displacements, plotted in *Figure 12*, are obtained and subsequently applied as boundary conditions to the *IVT* sub-model, transferred through the plate surfaces highlighted by the red circle. However, to fully define the sub-model, it is not sufficient to apply the displacements on the cut surfaces, coming from the global model resolution, but it is also necessary to account for external forces and thermal loads acting directly on the sub-model itself, such as:

- Internal pressures or surface loads that act on the component;
- Temperature fields or thermal gradients that generate thermal strains within the sub-model.

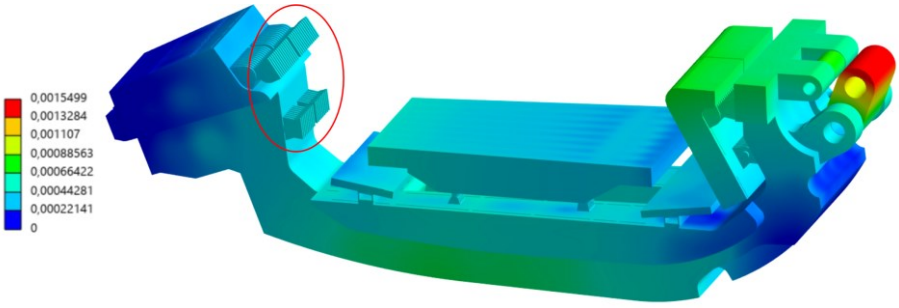

Figure 12 – Displacements [m] computed in the global model (pressure load case)

Static crack analysis

As shown in the case of the *IVT*, the comparison of maximum principal stress (*MPS)* between the global model and the sub-model indicates that the stress contours retain the same shape, but with slightly different values (*Figure 13*). Thanks to the submodeling analysis, it is possible to identify the critical point of the component, that is, the region potentially most susceptible to crack initiation (*Figure 14*).

At this point, a semi-elliptical crack is introduced using the *FRANC3D* software, with a depth arbitrarily set to 1/4 of the local wall thickness and an aspect ratio of 1/3 (*Figure 15*). The plane experiencing the highest stress at the identified critical location is presented in *Figure 16*. Initially, the crack is oriented in the plane parallel to the lower surface of the *IVT* and passing through the critical point. This will be referred to as the "0° crack". In *Figure 17* the crack and its associated stress state are shown. The analyzed crack is subsequently rotated first by 45° and then by 90° relative to its original plane (*Figure 18*, *Figure 19*).

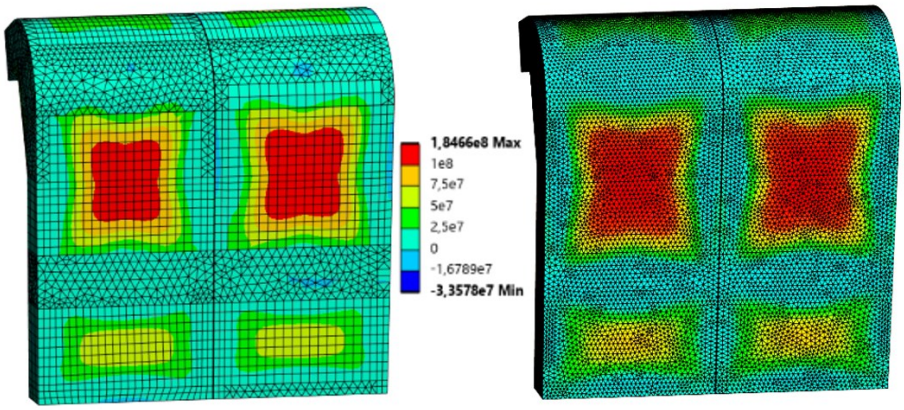

Figure 13 – Comparison between MPS [Pa] of the IVT in the global model (on the left) and sub-model (on the right)

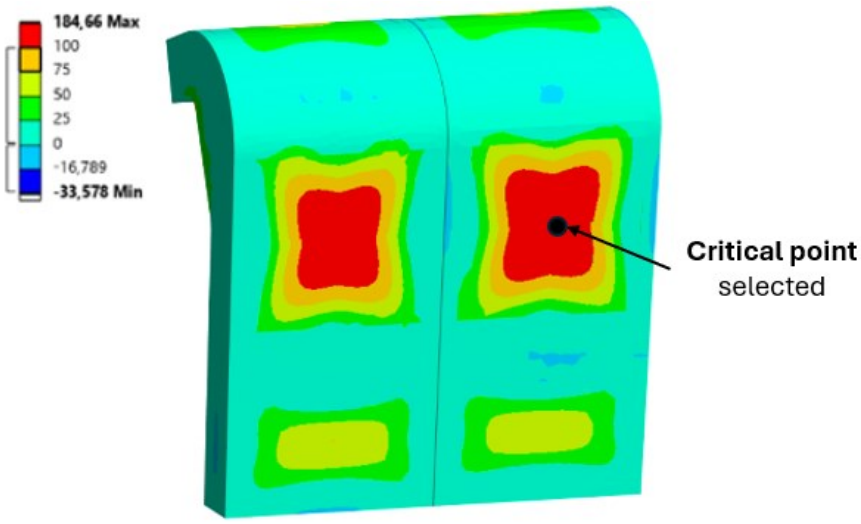

Figure 14 – Identification of the critical point in the IVT in terms of MPS [Pa] during the pressure load case

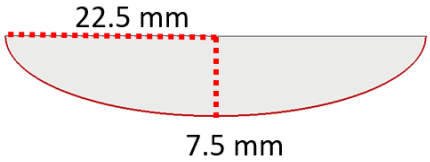

Figure 15 – Initial crack size

Static crack analysis

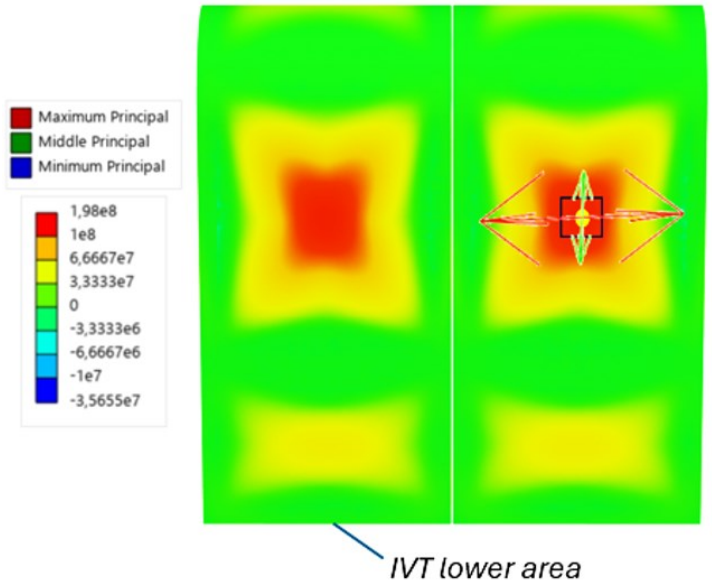

Figure 16 – Critical crack location for the pressure load case

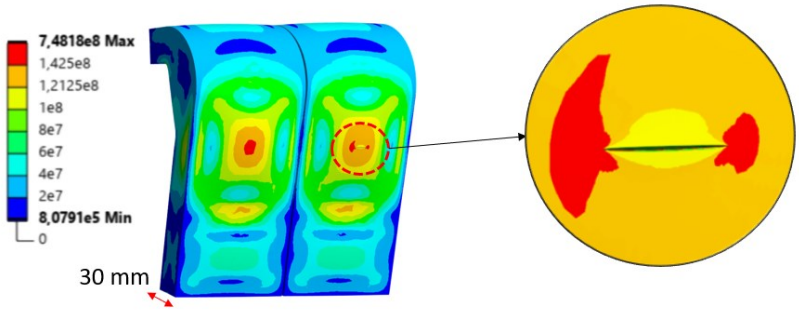

Figure 17 – 0° Crack detail and corresponding Von Mises stress state [Pa]

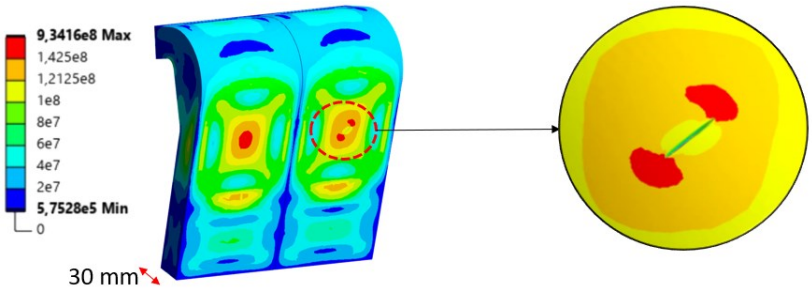

Figure 18 - 45° Crack detail and corresponding Von Mises stress state [Pa]

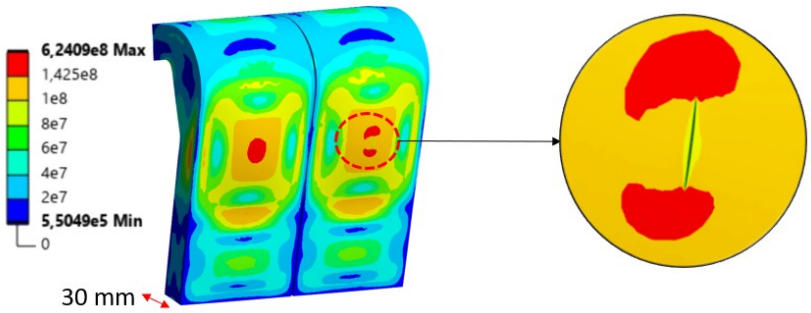

Figure 19 - 90° Crack detail and corresponding Von Mises stress state [Pa]

Then, using the M-integral method [27,28] implemented in *FRANC3D*, it is possible to calculate for the modeled cracks the three *SIFs* contributions separately (*Figure 20*): K_I, K_{II}, K_{III}, corresponding to the crack opening modes *I*, *II*, and *III* (*Figure 21, Figure 22, Figure 23*).

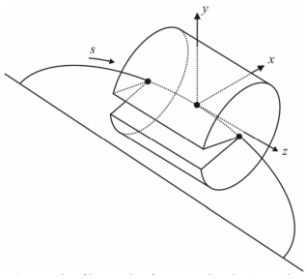

Figure 20 - Domain of integration for computing the 3D M-integral

The M-integral is a fracture mechanics-based method used to evaluate the stress intensity factors (SIFs) for three-dimensional cracks. It is an extension of the classical J-integral and is specifically formulated to separate the contributions of the three crack opening modes: mode I (tensile opening), mode II (in-plane shear), and mode III (out-of-plane shear). In this approach, a closed contour or a thin volume surrounding the crack front is defined, and the integral of the elastic energy density is computed using the nodal displacements and stresses obtained from the *FEM* solution (eq. (7)):

$$M_i = \int_\Gamma \left(\frac{1}{2}\sigma_{ij}\varepsilon_{ij}n_i - \sigma_{ij}\cdot\frac{\delta u_j}{\delta x_k}n_k\right) d\Gamma \qquad (7)$$

where:

- $i = I, II, III$ indicates the crack mode,

Static crack analysis

- The first term is the strain energy density, $W = \frac{1}{2}\sigma_{ij}\varepsilon_{ij}$,
- $\sigma_{ij}$and $\varepsilon_{ij}$are the stress and strain tensors,
- $u_j$are the nodal displacements,
- $n_i$is the outward normal to the integration contour Γ.

The stress intensity factors are then obtained from the M-integral values through the relationship (eq. (8)):

$$K_i = \sqrt{E' \cdot M_i} \tag{8}$$

The key advantage of the M-integral is its ability to provide mode-separated SIFs along the entire crack front, even in complex 3D geometries and under combined loading conditions, including mechanical and thermal effects. The computed M-integral values are then converted into the corresponding stress intensity factors K_I, K_{II} and K_{III}, which represent the local fracture driving forces. This method is particularly suitable for use with *FRANC3D*, where it can be applied as a post-processing tool on *FEM* models to evaluate crack propagation potential and assess the structural integrity of components under realistic operational loads.

The results show that as the crack approaches the vertical configuration, there is an increase in the Mode *I SIF* and a decrease in the Mode *II* and Mode *III SIFs*. This confirms the premise that the 90° configuration is the most critical, as the crack is positioned orthogonally to the *MPS* calculated at the critical point (*Figure 16*).

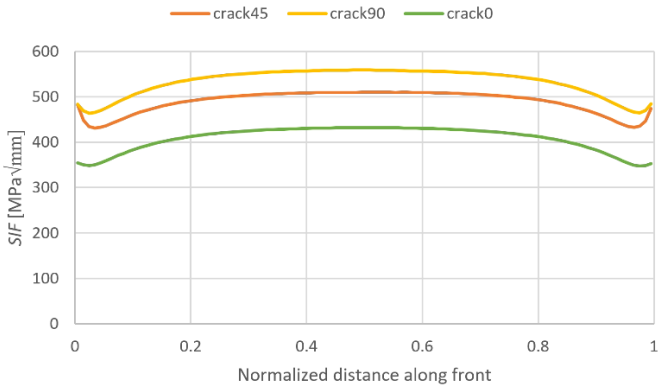

Figure 21 – K_I results by the three cracks configurations

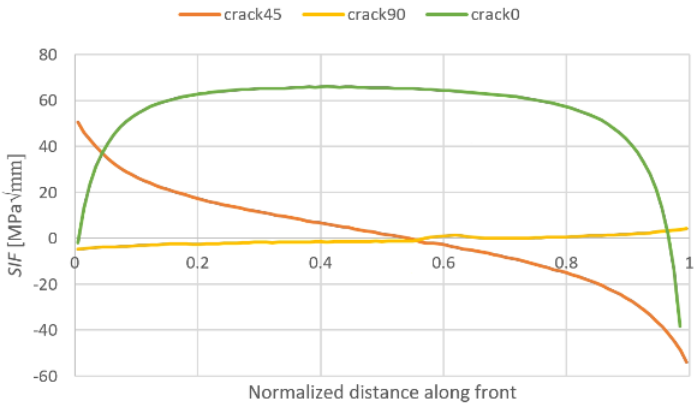

Figure 22 – K_{II} results by the three cracks configurations

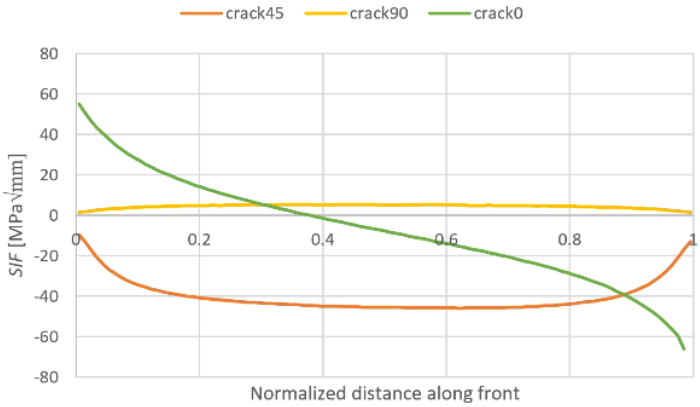

Figure 23 - K_{III} results by the three cracks configurations

3.3.2 Thermal load case

In addition to the pressure load case analysis, a thermal load case scenario is considered, in which only thermal loads are applied. In this scenario, the nodal temperature fields are imported from a previous thermo-fluid dynamic analysis representative of the *NoC*, that is, the steady-state operating conditions of the reactor. *Figure 24* shows the temperature fields applied to the *IVT*. The application of these temperature distributions allows the reproduction of the actual effects of thermal gradients that develop during divertor operation, where intense heat fluxes occur in the plasma-exposed areas and volumetric thermal loads arise. These thermal gradients generate significant stress states that can be a critical factor in the initiation and propagation of cracks. First, the global displacements are reported in *Figure*

25, and the red circle shows the boundary conditions transferred to the *IVT* sub-model. In this case as well, starting from the global analysis, the *MPS* are evaluated and subsequently recalculated using the *submodeling* technique on individual subcomponents.

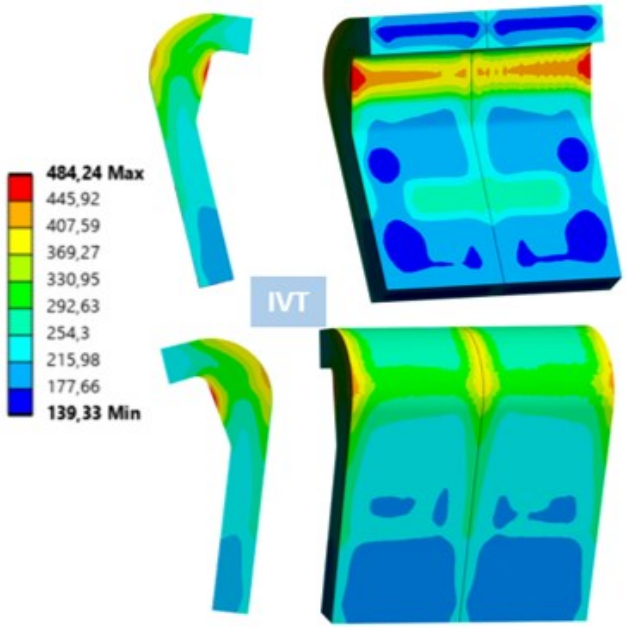

Figure 24 – Nodal temperatures [°C] applied to the divertor during the thermal load case

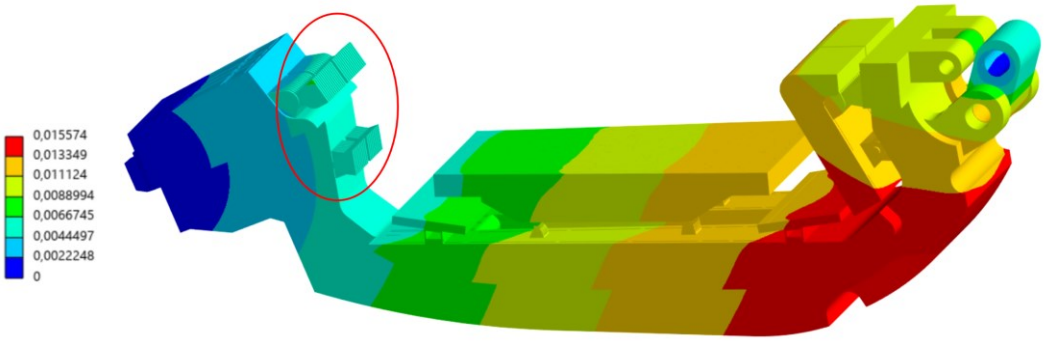

Figure 25 – Displacement magnitudes [m] computed in the global model (thermal load case)

Figure 26 shows the most critical orientation in terms of *MPS* among the various possibilities, highlighting that the maximum principal stress lies along the line indicated by the two red arrows. Therefore, the crack expected to be

critical is the one positioned orthogonally to this line. The objective is to identify the areas of the most critical model in terms of potential Mode *I* crack openings and then proceed with a detailed fracture analysis. A clarification concerns the selection of the critical point, which is not chosen in the most stressed area of the model. The areas highlighted in red in the contour plot were not selected as critical, since they are affected by the imposed boundary conditions acting on the submodel, which prevent any modification of the geometry or the mesh. *Figure 27* shows the placement of the crack in the model and the two tips that define it.

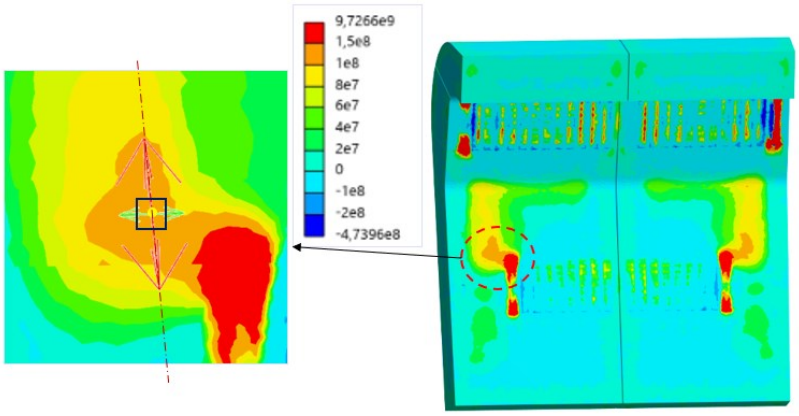

Figure 26 – MPS [Pa] computed in the IVT submodel (thermal load case)

The calculated *SIF* is shown in *Figure 28* and refers to the most critical case of the thermal load case, consisting of a crack inclined at 0° (as inferred from the critical orientation shown in *Figure 26)*. This results in K_I values much higher than those calculated in the pressure load case. Moreover, the asymmetry of the curve is due to the fact that one of the two crack tips is closer to the red-colored zone in the contour plot, which indicates a more critical state of stress.

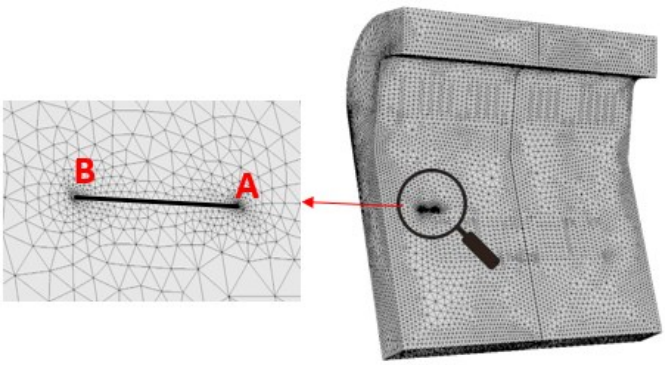

Figure 27 – Position of the critical crack

Static crack analysis

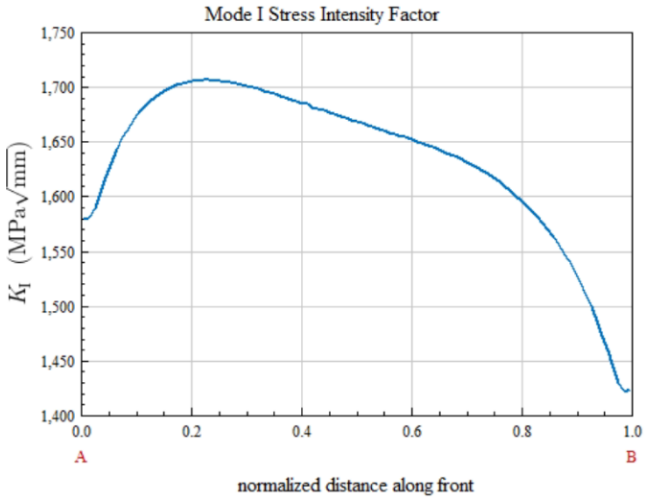

Figure 28 - K_I computed in the critical point for the "0° crack"

3.3.3 *EM* load case

The *EM* load case is analyzed to quantify the impulsive Lorentz forces resulting effects on the *IVT* and compare it to the previous cases. The displacements determined by this loading condition are represented in *Figure 29*:

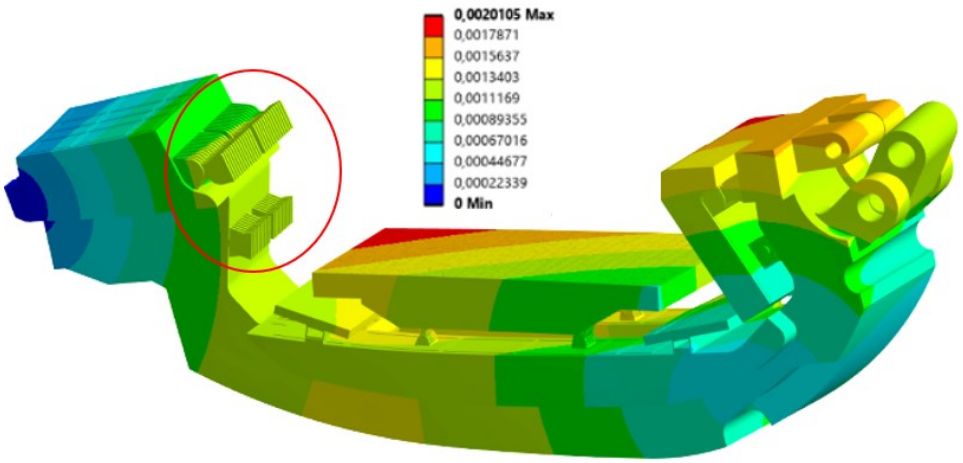

Figure 29 – Displacement magnitudes [m] computed in the global model (EM load case)

In *Figure 30* the resulting *MPS* are showed in the uncracked configuration of the *IVT*, and a critical "red" area is highlighted; In *Figure 31* is reported the

cracked configuration, remeshed thanks to the *FRANC3D* software and the corresponding maximum principal stress distribution in the component, while in *Figure 32* the *SIF* along the crack front is plotted.

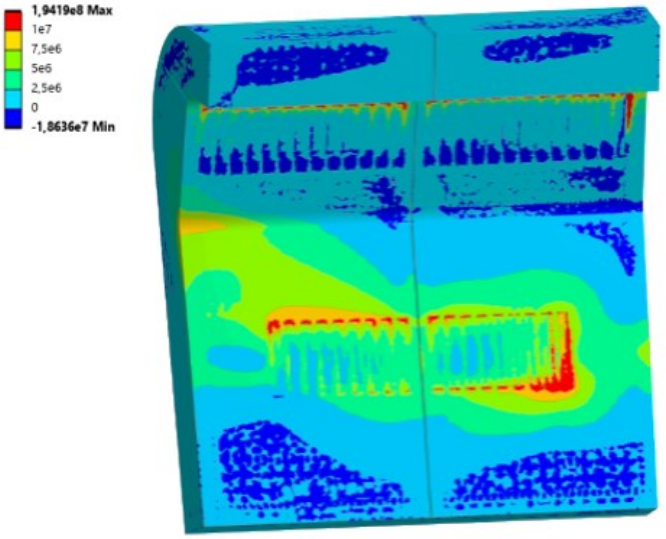

Figure 30 – MPS [Pa] in the uncracked IVT configuration

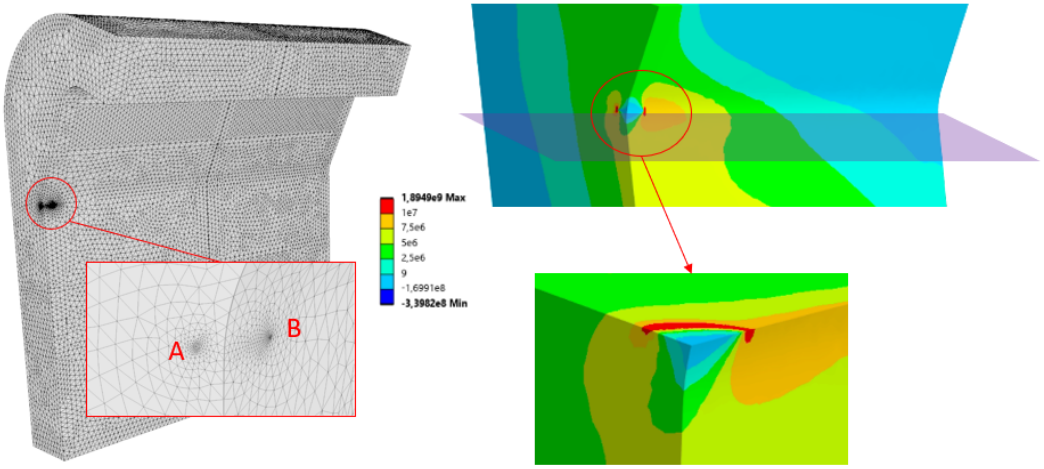

Figure 31 – Critical point identification and MPS [Pa] plot of the cracked IVT

Static crack analysis

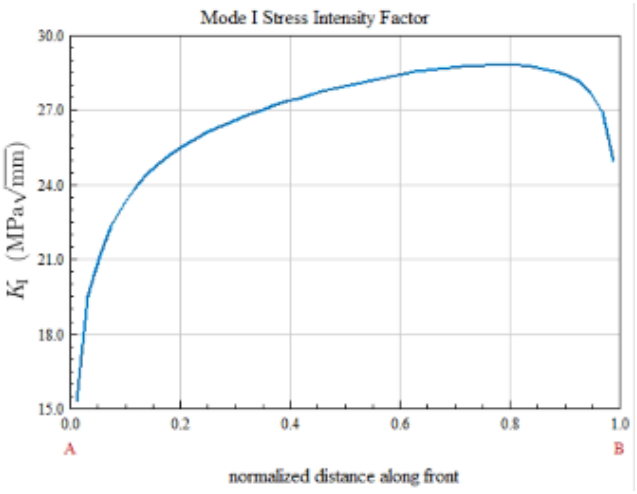

Figure 32 - K_I computed in the critical point

3.3.4 Combined pressure-thermal load case

The last load case analyzed consists of applying both pressure and thermal loads simultaneously, more specifically considering a configuration in which the pressure remains continuously active while the thermal load is applied cyclically through on–off cycles (*Figure 33*).

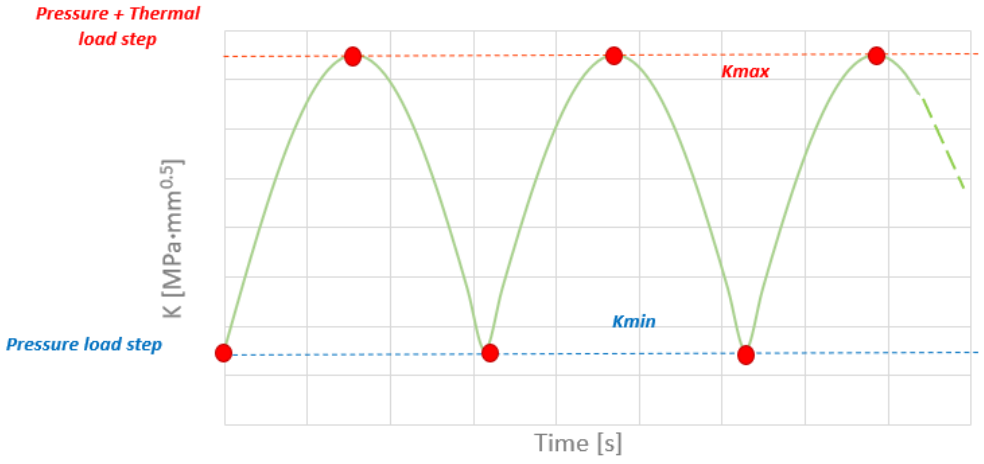

Figure 33 – Loading configurations of the combined load case

A first image of the condition when both the loads are active is given by *Figure 34.* In this configuration it is possible to look at the displacements determined over all the structure by this *combined* load case.

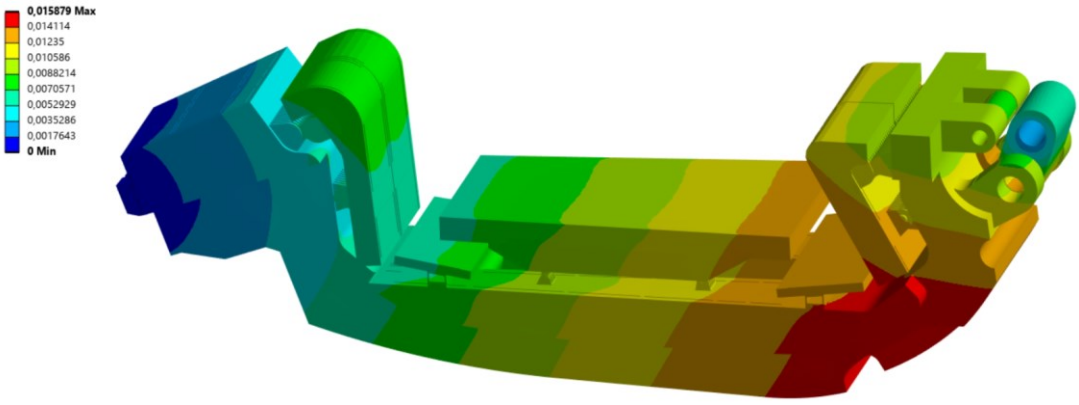

Figure 34- Displacement magnitudes [m] computed in the global model (combined load case)

In *Figure 35*, the focus is placed on the *MPS* evaluated on the *IVT*, and the region of interest within the component is highlighted. Section planes are employed to isolate a limited region of the *IVT*, as the combined application of pressure and thermal loads in this load case results in a significantly higher computational cost (*Figure 35*).

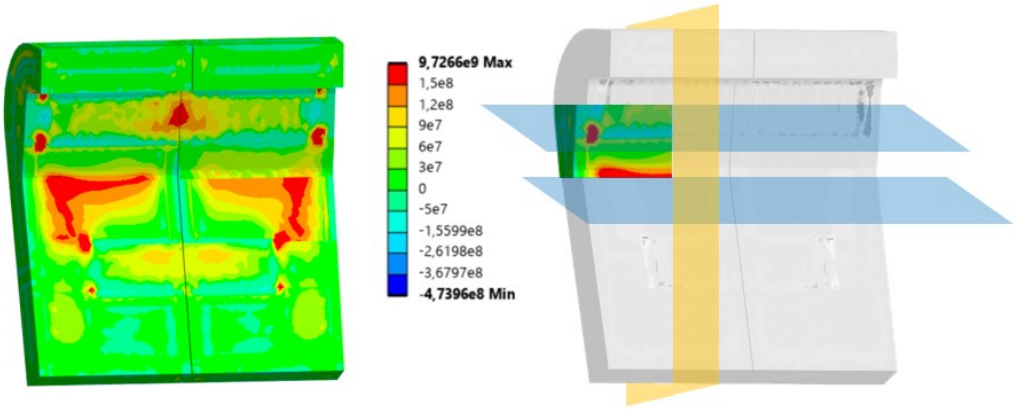

Figure 35 - MPS [Pa] external distribution and sub-model extraction

In *Figure 36* it is clearly showed the extracted *IVT* sub-model and the respective Von Mises stress distribution.

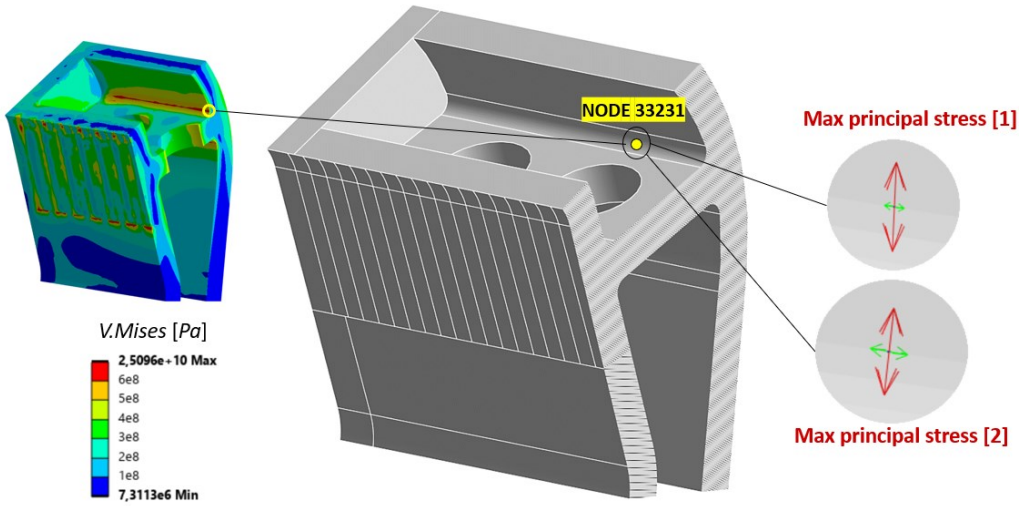

Figure 36 – Detail of the sub-model: Von Mises stresses [Pa] and local maximum principal stress direction in the two analyzed configurations

In the following *Figure 37* and *Figure 38* the mode *I SIFs* are reported for the first load step with only pressure applied and for the second one with the addition of the thermal load.

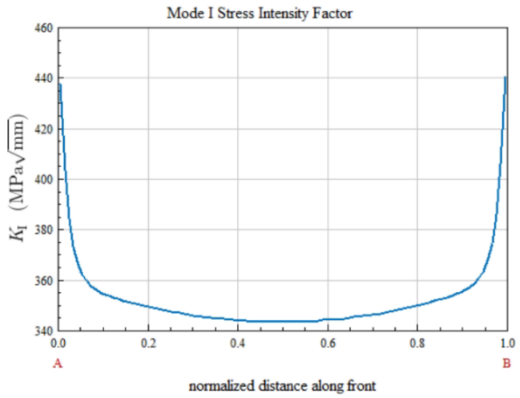

Figure 37 - K_I computed in the critical point (pressure load step)

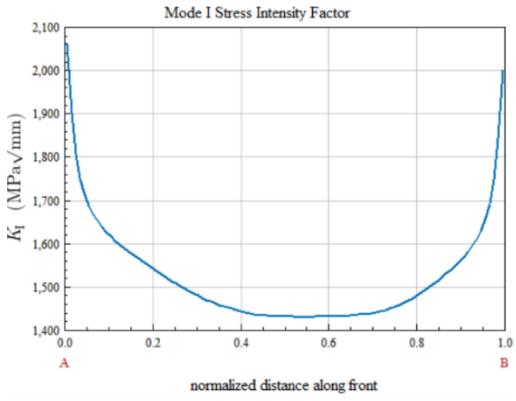

Figure 38 - K_I computed in the critical point (pressure + thermal load step)

4. Crack growth analysis

4.1 Analysis workflow

The simulation is performed using the *FRANC3D* software, which allows evaluation of crack evolution based on local stress fields and component geometry. An underlying phenomenon, influencing crack propagation, is crack kinking, i.e., the deflection of the crack from its original plane (*Figure 39*).

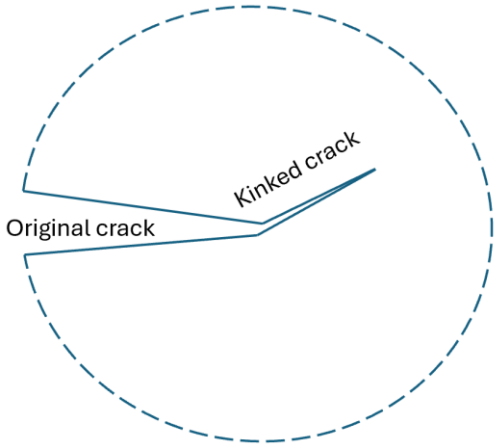

Figure 39 – Crack kinking principle

This behavior is governed by the *Maximum Tensile Stress* (*MTS*) criterion of *Erdogan* and *Sih* [29], according to which the crack tends to deflect orthogonally to the direction in which the maximum principal stress occurs. In other words, the local orientation where the principal stress reaches its maximum determines the preferential direction of crack propagation. This criterion allows for a realistic prediction of the crack front orientation, even in the presence of non-uniform or complex stress fields.

The results of crack growth are evaluated for the most critical configuration of the two analyzed load cases, corresponding to the point and orientation of the crack identified during the static crack analysis phase.

The propagation of the previously introduced crack was simulated in five incremental steps of 0.2 mm each, resulting in a total crack advancement of 1 mm (*Figure 40*). For the pressure and thermal load cases an increment of 0.2 mm was selected to investigate the crack growth under each individual loading condition. Conversely, in the *combined* load case, a larger propagation increment was adopted to evaluate the number of cycles required to produce more substantial crack extensions, thereby assessing the component's behavior under more realistic and cumulative service conditions.

Crack propagation is investigated for all the previously defined load cases, with the exception of the EM case, as its loading condition is stochastic in nature and not representative of regular operating scenarios. Moreover, the electromagnetic (EM) loading is inherently transient and dynamic, being associated with fast plasma events and rapid current variations. A detailed dynamic analysis of the EM case is beyond the scope of the present work; for this aspect, the reader is referred to Zhang et al. (2023) [30], who investigated the dynamic structural response of the DEMO divertor under electromagnetic loading.

4.1.1 Pressure load case analysis

In the pressure load case, the following *Figure 40* shows the step-by-step evolution of the crack, while the figures from *Figure 41* to *Figure 44* highlight the resulting *SIFs*.

Figure 40 – Crack growth analyzed

Crack growth analysis

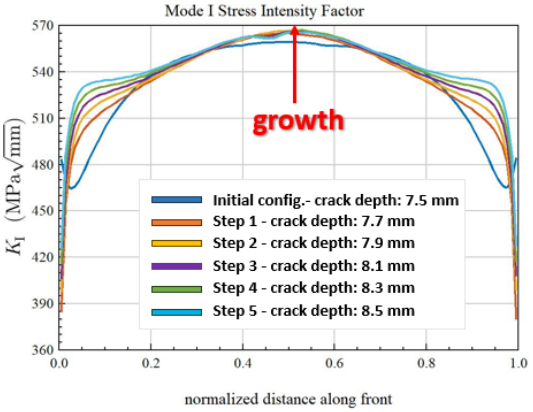

Figure 41 – K_I related to the 90° crack growth (configuration of Figure 19)

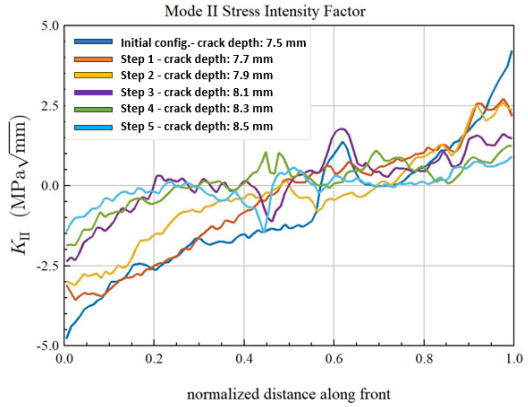

Figure 42 – K_{II} related to the 90° crack growth (configuration of Figure 19)

As can be seen from the graph in *Figure 44*, the K_I values initially increase but then tend to decrease. This seemingly counterintuitive behavior can be explained by analyzing what happens within the thickness of the wall in which the crack is embedded (*Figure 45*): it can be observed, in fact, that as the crack propagates, the central part of its front approaches a region with a decreasing stress field.

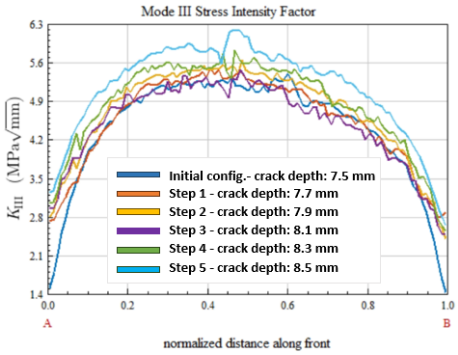

Figure 43 – K_{III} related to the 90° crack growth (configuration of Figure 19)

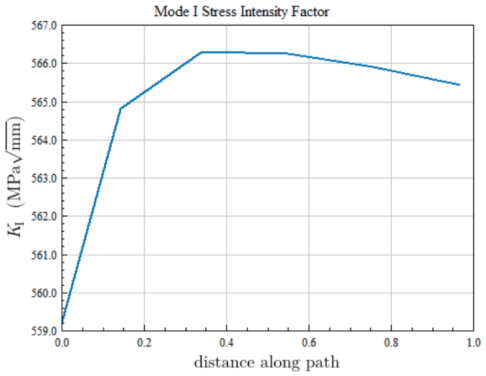

Figure 44 – Peak values of K_I along the middle crack front obtained from the crack growth

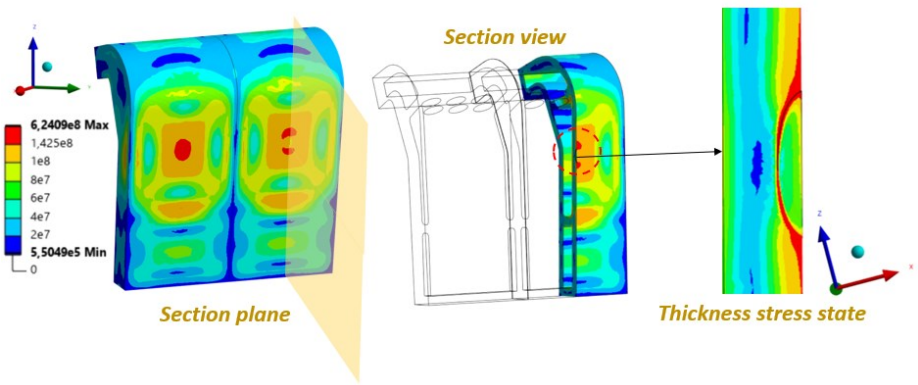

Figure 45 – Detail of the Von Mises contour plot [Pa] for the critical configuration of the "pressure load case"

Crack growth analysis

4.1.2 Thermal load case analysis

Performing the same steps for the thermal load case yields the following results (*Figure 46*, *Figure 47*, *Figure 48*, *Figure 49*):

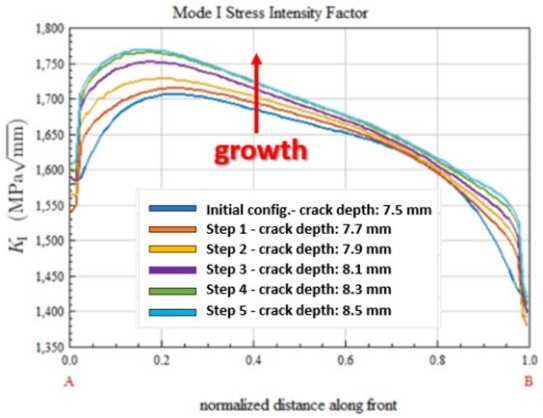

Figure 46 - K_I related to the 0° crack growth (critical configuration)

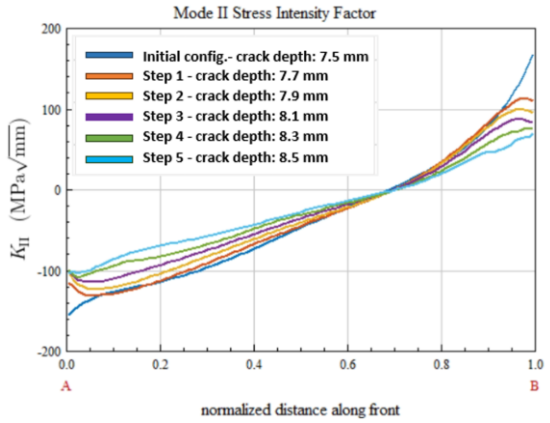

Figure 47 - K_{II} related to the 0° crack growth (critical configuration)

It can also be observed here that the Mode *I SIF* tends to increase during crack propagation, while the Mode *II* and *III SIFs* remain an order of magnitude lower. In *Figure 49*, unlike what is observed in the pressure load case, the graph shows a monotonically increasing trend of maximum Stress Intensity Factor along the propagation always in correspondence of the crack front point defined by a normalized distance of 0.15 (*Figure 50*).

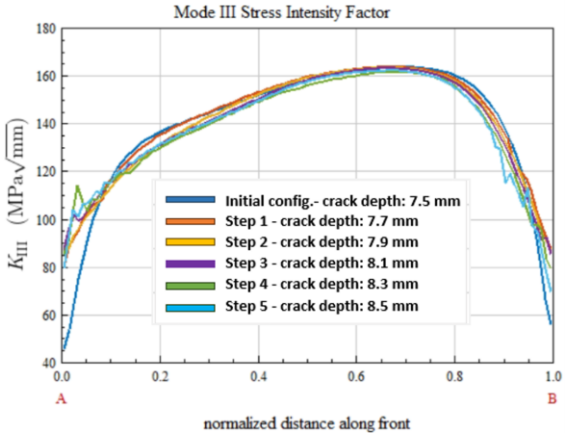

Figure 48 - K_{III} related to the 0° crack growth (critical configuration)

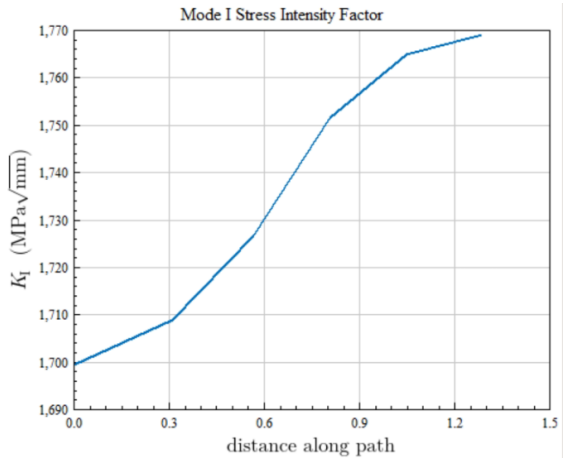

Figure 49 - Peak values of KI along the normalized distance of 0.15

Figure 50 - Path corresponding to the normalized distance of 0.15 along the crack front

4.1.3 Combined pressure and thermal load case analysis

The crack growth of the *combined* load case is structured in two load steps, as described in the previous chapter (§3.3.4). In the first one, only the pressure

loading is switched on, while in the second the thermal contribution is added. To investigate the stress intensity factor behavior for larger crack sizes, the crack is propagated in 0.5 mm increments instead of the 0.2 mm used in the other load cases. The obtained results are showed in *Figure 51*, *Figure 52* and *Figure 53*.

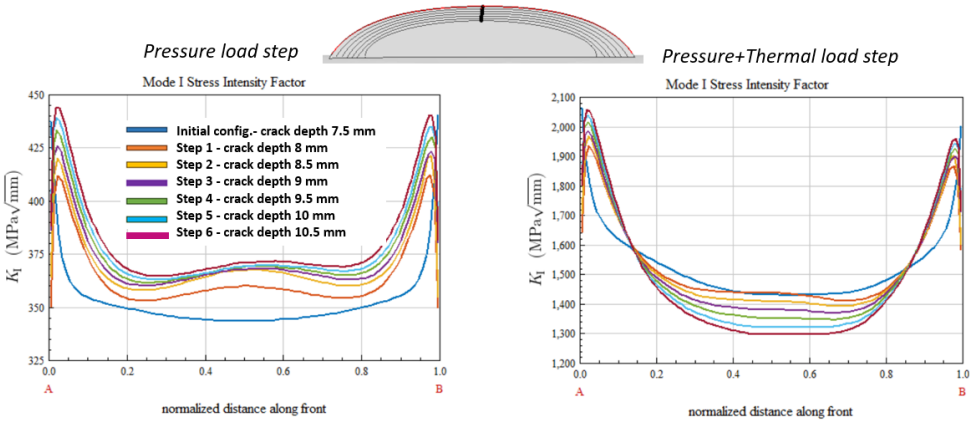

Figure 51 – Crack growth for the combined load case (K_I)

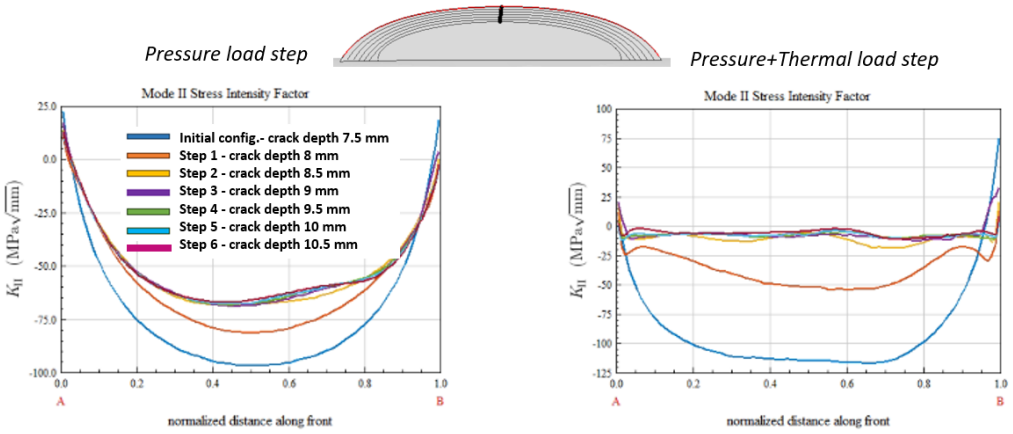

Figure 52 – Crack growth for the combined load case (K_{II})

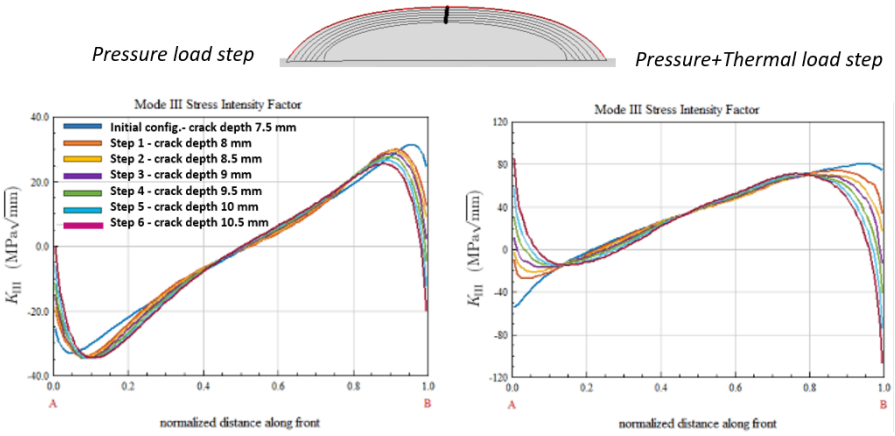

Figure 53 - Crack growth for the combined load case (K_{III})

Figure 54 shows the *SIF* during propagations at the crack front point whose normalized distance is equal to 0.05, because here K_I gets the highest values during the crack growth in the *combined* load case.

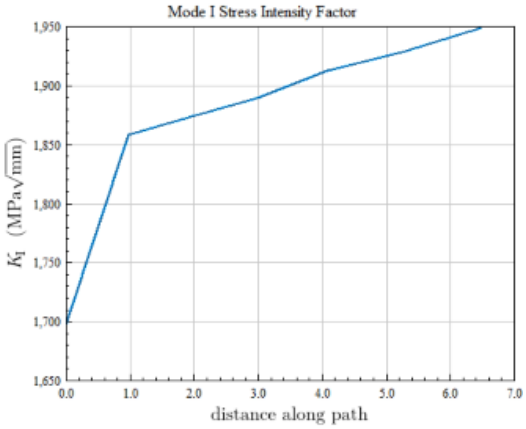

Figure 54 - Peak values of K_I along the crack front (2nd load step)

5.Divertor lifetime assessment

5.1 Methodology

The final phase of the study is dedicated to an assessment of the necessary cycles to determine the analyzed crack growth in the component, with the aim of estimating its reliability under realistic operating conditions. The analysis is conducted in a simplified form, considering the cyclic effect of the thermal load or the pressure load independently. In the pressure load case, only on/off cycles of the applied pressure are analyzed, while in the thermal load case, the analysis focuses exclusively on the on/off application of the thermal load. Starting from the *SIF* values calculated in the crack growth simulations, the corresponding ΔK is determined, i.e., the stress intensity factor range associated with the load cycle. This parameter represents the key variable for predicting the crack propagation rate under fatigue conditions.

5.2 Reference material data

For modeling the phenomenon, eq. 9 is used, where *da/dN* is the crack growth rate per cycle, ΔK is the stress intensity factor range, and *C* and *m* are material-dependent coefficients:

$$\frac{da}{dN} = C \cdot (\Delta K)^m \tag{9}$$

In this study, the *C* and *m* parameters were identified from the literature for the material *Eurofer97* (*Table 2*), which is one of the reference structural materials for the divertor components.

In the following study [31], the fatigue crack growth data were initially calibrated in the near-threshold region, corresponding to the initial portion of the Paris curve. This calibration was performed according to the modified law (eq. (10)):

$$\frac{da}{dN} = C \cdot (\Delta K - \Delta K_{th})^m \quad (10)$$

where:

- ΔK_{th} is the value below which no crack growth occurs.

To relate these results to the classical Paris law, without the additional threshold term, the curves reported in the article were first plotted using the modified-law coefficients (eq. (10)). The growth law parameters were then recalibrated in the linear region of the Paris curve, where da/dN vs. ΔK exhibits a linear relation in a log-log scale. The resulting Paris law was finally applied in *FRANC3D* and used to evaluate crack growth rates within the operative range of ΔK for the modeled components.

The *Eurofer97* fracture toughness value is significantly higher than the maximum value obtained in the present analyses, e.g. exceeding 8000 MPa·√mm at 20 C° as shown in ref. [32]. In a first, simplified analysis, the fatigue lifetime under individual load cases (pressure or thermal) was evaluated by assuming a stress ratio equal to zero, corresponding to a pure "on–off" operating condition. Subsequently, the combined load case, in which the two load steps previously described are superimposed, was analyzed.

Figure 55 shows the Paris curves in log-log scale related to the *Eurofer97* calculated with the computed parameters of *Table 2*, for the reference temperatures.

R [-]	Temperature [°C]	ΔKth [MPa·√mm]	C [(mm/cycles)/(MPa·√mm)^m]	m [-]
0.1	RT	285.2374	3.67E-07	0.8285
	300	247.9226	2.67E-12	2.556
0.5	RT	149.5757	6.57E-12	2.436
	300	165.3871	3.73E-11	2.222

Table 2 – Paris coefficients depending on temperature and stress ratio

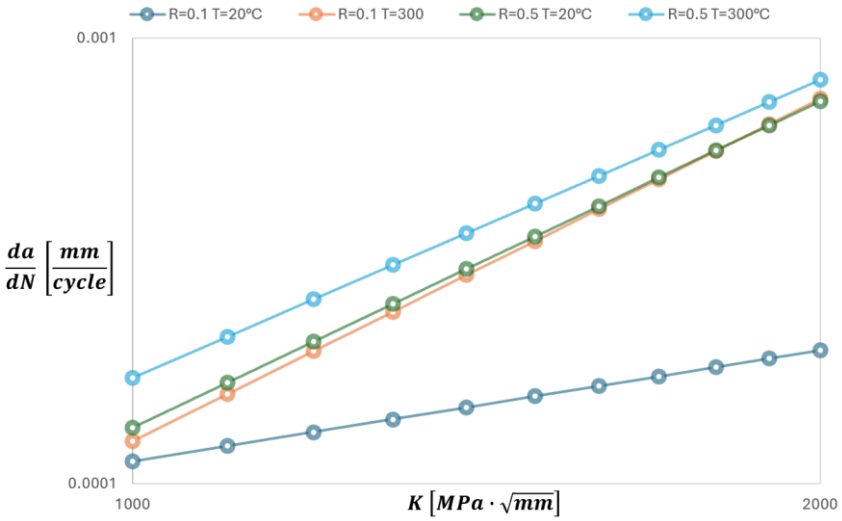

Figure 55 – Eurofer97 Paris curves in correspondence of different stress ratios (R) and temperatures

5.3 Paris law application

The critical crack for the thermal load case is in a zone characterized by a temperature of approximately 180°C. The application of Paris' law, calibrated at such temperature, allowed estimating the number of cycles required for the crack to grow to the sizes calculated and indicated in the previous chapters. The results obtained from the crack propagation studies under the pressure and thermal load cases are reported below (*Figure 56*).

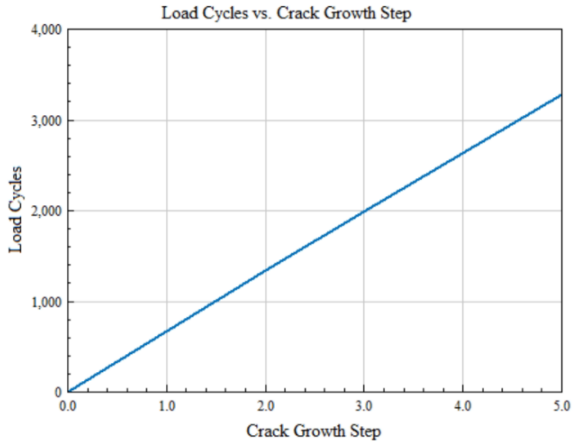

Figure 56 – Number of loading cycles required to grow the original crack by 1 mm (thermal load case)

When considering the *Paris law* parameters calculated at 20 °C for the material, the relatively low loads such as those in the pressure load case result in slow crack growth. Consequently, the number of cycles required for 1 mm propagation (*Figure 57*) is quite high and equal to about 15500 cycles instead of 3200.

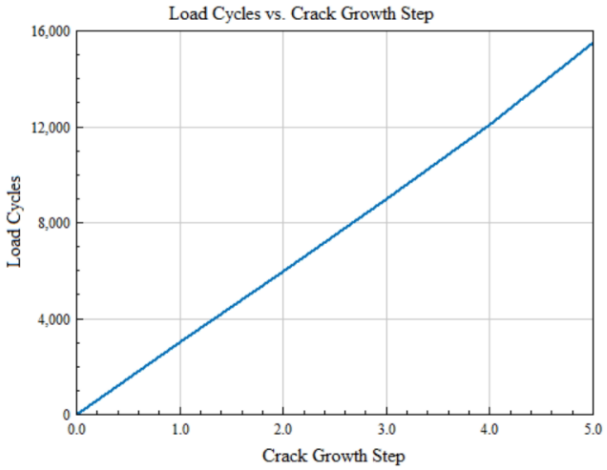

Figure 57 – Number of loading cycles required to grow the original crack by 1 mm (pressure load case)

Based on the sub-model derived from the combined load case, the initial cracked configuration was subsequently defined. Using *FRANC3D*, it was then possible to extract the stress ratio and temperature conditions along the front of the introduced crack (*Figure 58* and *Figure 59*).

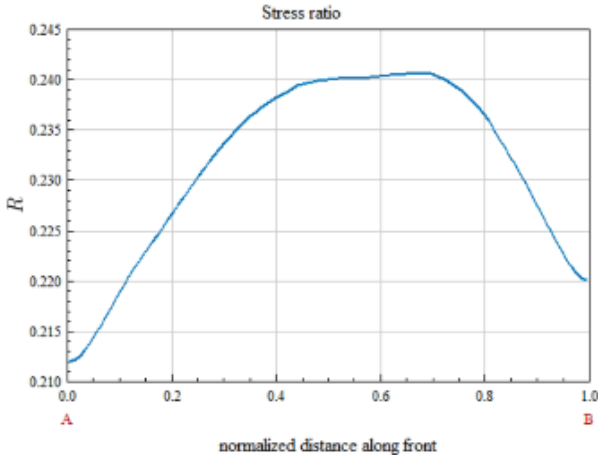

Figure 58 – Stress ratio along the starting crack front

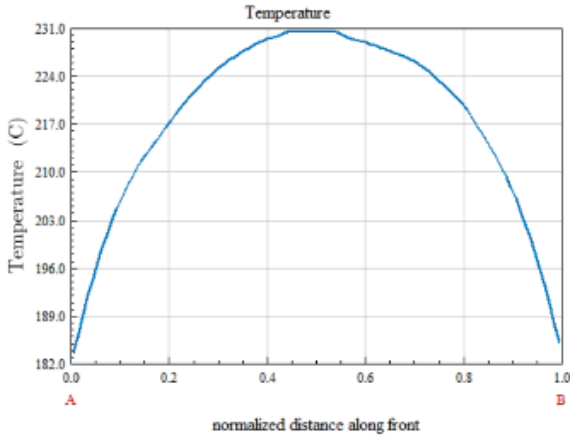

Figure 59 – Temperature along the starting crack front

The results of the lifetime assessment in the combined load case that determines a growth of 3 mm from 7.5 to 10.5 mm is reported in *Figure 60*. In this case, the Paris law calibration was adapted to account for the local temperature and stress ratio, both varying along the crack front and during the propagation.

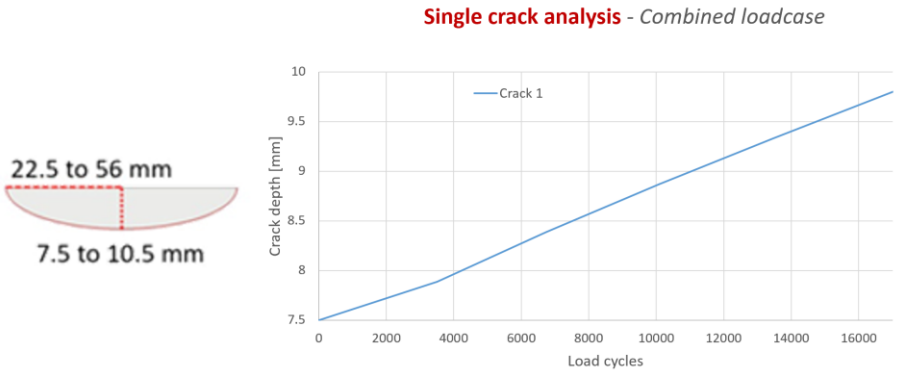

Figure 60 – Number of loading cycles required to grow the original crack by 3 mm (combined load case)

A possible future development of this work concerns extending the analysis to non-proportional loading, in which the different load components vary over time with different phases and amplitudes. Such conditions, which are typical of many real operating scenarios, can significantly influence both the crack propagation direction and rate. As discussed by Nöhring et al. [33,34], investigating non-proportional loading under combined static-cyclic

multiaxial conditions allows for a more realistic description of fatigue behavior in structural components, thereby improving the accuracy of residual life and structural reliability predictions.

6.Multiple crack analysis

In this chapter, the simultaneous propagation of two cracks located in a critical position of the *IVT* under the combined load case is analyzed. Building upon the single crack studied in node 33231 (as presented in the paragraph §4.1.3), an additional crack is introduced at node 21421 (*Figure 61*) to investigate potential interaction effects. The following procedure is similar to that adopted by Giannella et al. [35] who demonstrated that introducing multiple cracks can significantly influence the fatigue life and crack growth paths due to stress redistribution and crack shielding effects. Their results highlight the importance of considering more than a single defect in realistic structural assessments, particularly in regions prone to complex stress states.

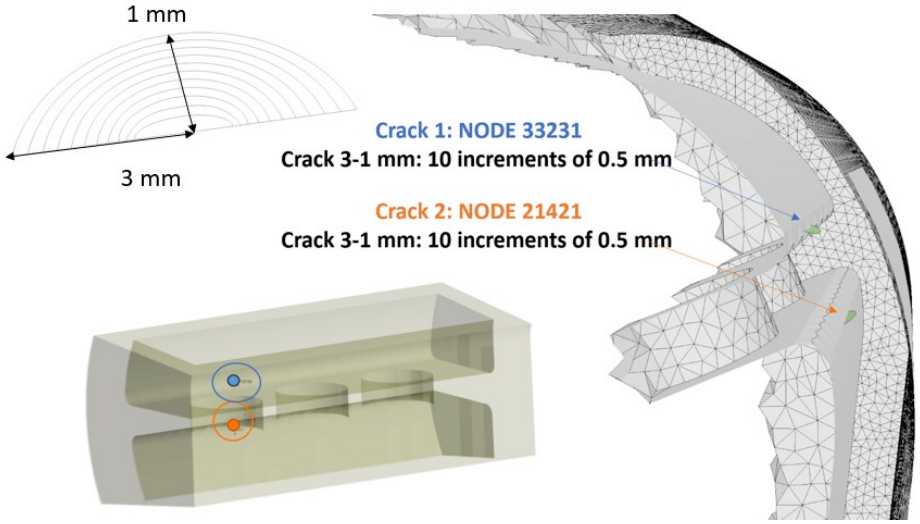

Figure 61 – Starting configuration of the multiple crack analysis

The two load steps applied to the divertor are the same as before: load step 1, with only the internal pressure applied, and load step 2, where the thermal contribution is added.

Both cracks are modeled as elliptical, with an initial size of 3 mm in width and 1 mm in depth. Crack propagation is evaluated incrementally in 10 steps of 0.5 mm, until a final depth of 6 mm is reached in one of the two cracks.

Crack growth is driven by the maximum stress intensity factor developed along the fronts of both cracks during load step 2, when both thermal and pressure loads are active. The *SIFs* along the two crack fronts under load step 1, when only the pressure load is applied, are presented in *Figure 62*, while the results for load step 2 are shown in *Figure 63*.

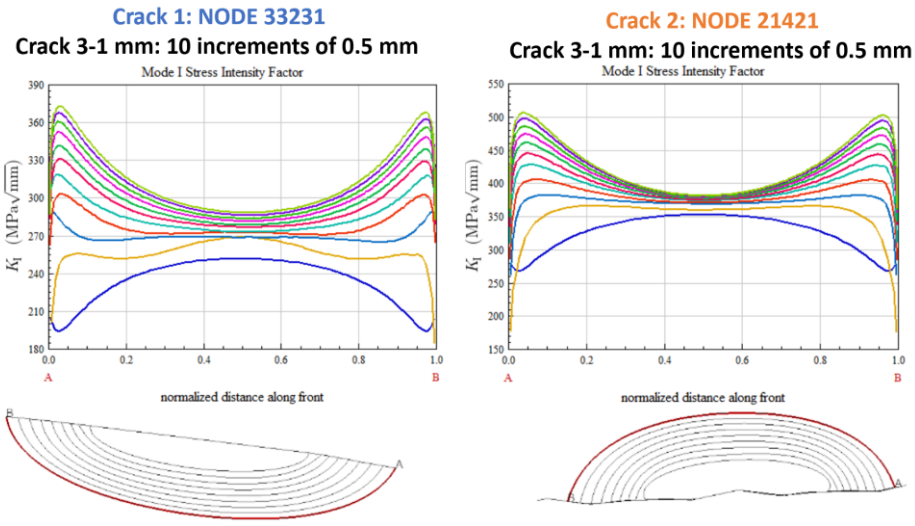

Figure 62 – Stress intensity factors evaluated for both cracks at the first load step and crack growth detail

Multiple crack growth

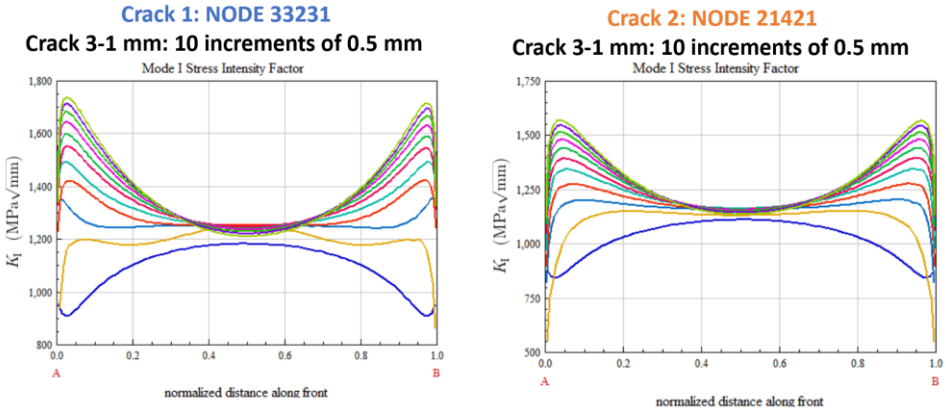

Figure 63 - Stress intensity factors evaluated for both cracks at the second load step

Since the stress intensity factors developed are comparable, the two cracks exhibit almost identical propagation. In *Figure 64*, the estimated number of cycles required for the crack to grow from 1 mm to a total depth of 6 mm is reported.

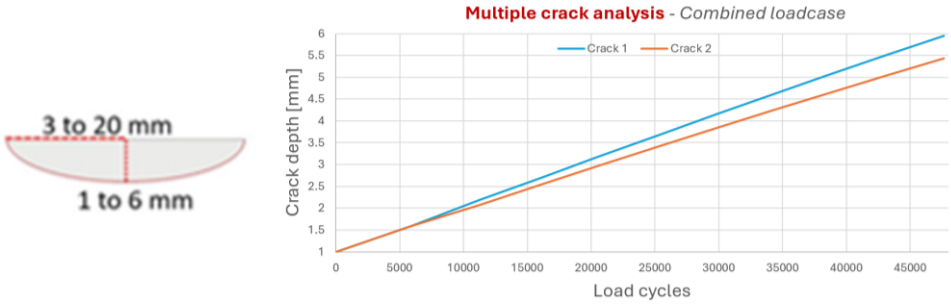

Figure 64 – Crack depth versus number of cycles for the two modeled cracks (see Figure 61) for the combined load case

7.Plastic material model

7.1 Introduction and objectives

In the previous chapters, the structural behaviour of the *DEMO* divertor, particularly of the *IVT*, was investigated under different loading conditions, primarily within the framework of *LEFM*. The analyses assumed an elastic material response, which is valid as long as the stress field around the critical regions remains below the yield limit of the structural material (*Eurofer97*).

However, due to the combined action of pressure and thermal loads, some localized yielding phenomena cannot be excluded. Evaluating the extent of these plasticized regions is essential to validate the applicability of the *LEFM* approach adopted in the previous chapters. For a more accurate assessment, Amato et al. [36] provide a detailed methodology for investigating crack-tip plasticity in hollow-cylindrical specimens, demonstrating how numerical analyses can be used to quantify local yielding and define the limits of LEFM applicability under complex loading conditions. Their approach highlights the importance of considering plastic zones to ensure that linear elastic assumptions remain valid in structural integrity evaluations.

The updated material definition includes the temperature-dependent plastic properties, implemented through tabulated true stress–plastic strain data [37] reported in *Figure 65*;

Plastic material model

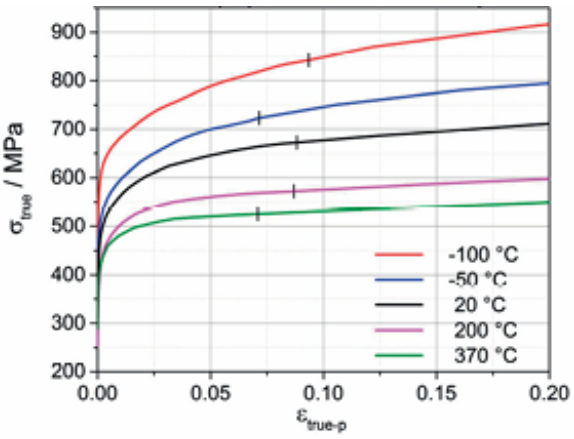

Figure 65 – Eurofer97 complete curves at different temperatures

7.2 Results overview

Initially, the results from the sub-model (*Figure 66*) of the *combined* load case described in §3.3.4 are presented, outlining the reference elastic response of the component.

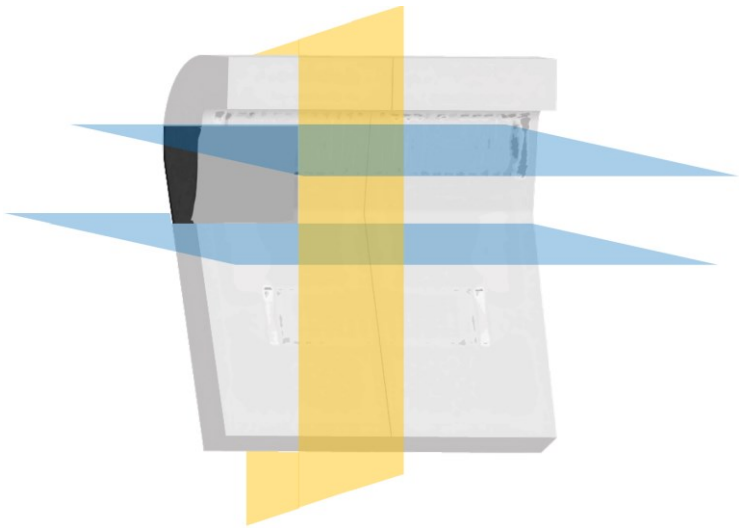

Figure 66 – Section plane applied to the IVT and sub-model extraction

In *Figure 67* and *Figure 68*, after applying the plastic material models to all divertor components made of *Eurofer97*, namely to the global model, it is evident that the component exhibits a surface region approaching the onset of plastic yielding.

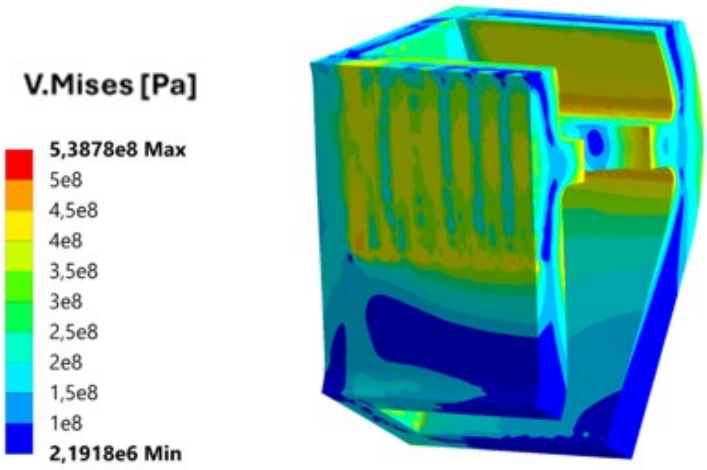

Figure 67 – Von Mises stresses for the combined load case under elastoplastic material behaviour

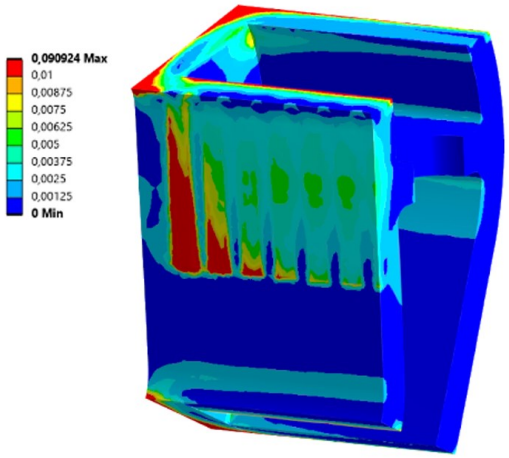

Figure 68 – Equivalent plastic strains for the combined load case under elastoplastic material behaviour

In *Figure 69* a crack corresponding to the one adopted in the paragraph §3.3.4 is inserted in the *IVT* model with plasticity.

Plastic material model

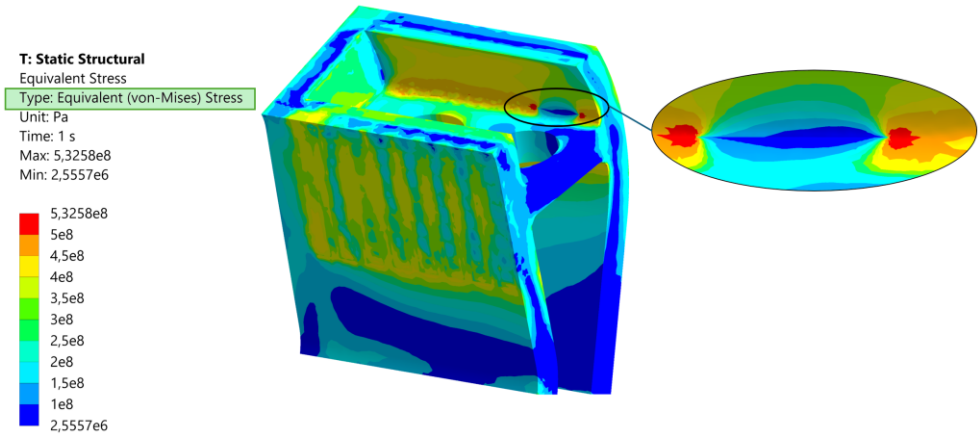

Figure 69 - Von Mises stresses for the cracked combined plastic load case

To better assess whether the material undergoes plastic deformation in the analyzed region, the distribution of equivalent plastic strain is reported in *Figure 70*.

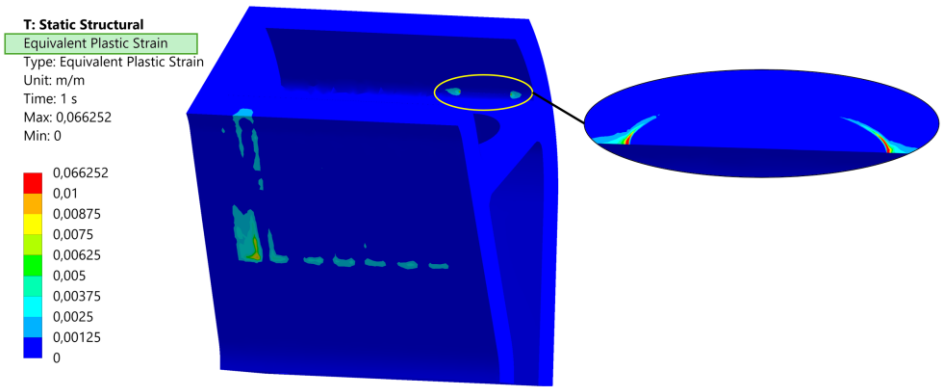

Figure 70 – Equivalent plastic strains for the cracked model in the combined load case

It can be observed that only a very small region around the crack front adjacent to break through points undergoes appreciable plastic deformation. This localized yielding occurs on the external surface, where the temperature is higher than in the inner volume, resulting in a locally reduced yield strength.

Such localized yielding turns out to be sufficiently limited to make applicable the LEFM for the considered load case and crack configuration.

Chapter 1

PART 2:

REMOTE MAINTENANCE SYSTEM FOR THE DEMO BREEDING BLANKET

8.Introduction and problem statement

The purpose of this work is to analyze and evaluate the thermal phenomena affecting the *remote maintenance system* (*RM*) for the *DEMO Breeding Blanket*. The activity arises from the need to have a reliable characterization of the *heat transfer mechanisms* involving *actuators* and *support structures* during the installation and removal phases of the blanket modules. To this end, *FE models* were developed, accompanied by *analytical models* for validation purposes, useful to describe the *thermal behavior* of the system under different *operating conditions*. The main objective is to provide:

- a clear understanding of the *assumptions made* and the *models employed*;
- the *validation* of the *complex FE models* used to analyze the remote maintenance system named *HKM* (hybrid kinematic manipulator) mechanism;
- the identification of *critical design parameters*;
- the development of a more *detailed and realistic model*;
- support for future design decisions, regarding the safety and reliability of the RM system and the need for any active cooling system.

The project falls within the scope of remote maintenance activities for the *DEMO* reactor, with reference to the breeding blanket (*BB)* handling and replacement systems. The thermal management of actuators and mechanical structures is a critical aspect to ensure the reliability of the system during the installation and removal of blanket modules, as these components might be subjected to significant thermal loads in a high-temperature environment.

To address these issues, an analysis pathway was developed that combines simplified models and *FE* simulations (with increasing level of complexity and detail), aiming to understand the heat transfer dynamics between the main components (mover, *BB*, and environment), validate the initial assumptions, and identify possible thermal risk mitigation strategies. *UKAEA* requested, for this purpose, the development of a reference model for analyzing the thermal behavior of the *RM system actuators*, particularly the mover used for the handling of *BB* segments.

The identified requirements are:

- verify, using both simplified and *FE analysis* approaches, the reliability of the assumptions and the system sensitivity to the main design input parameters;
- assess the system's ability to dissipate the heat generated internally by the mechanical actuators;
- assess the heat transferred through contact with the hot *BB* (≈ 130 [°C] initial);
- analyze the temporal evolution of the mover temperature until equilibrium conditions with the environment are reached (≈ 80 [°C]);
- understand the influence of natural convection through an in-depth analysis of the film coefficient;
- study mitigation scenarios through the introduction of insulating layers.

The final objective is to ensure that the *RM* system maintains safe operating conditions, avoiding overheating phenomena that could compromise the functionality of the actuators, reduce the strength of the structure and the success of maintenance operations.

The *FE* software package used in this work is *Abaqus/CAE 2024*. The simplified geometry was created and analyzed directly in *Abaqus/CAE 2024*, while the more realistic *3D CAD* geometry was analyzed in Abaqus.

In addition, the software *Matlab* was employed to perform a parametric study of the analytical and simplified models, enabling sensitivity analyses and supporting the validation of the *FE* results obtained with *Abaqus*.

Different *BB* movers have been proposed in the last years, each one characterized by a specific design concept, mechanical characteristics, advantages and disadvantages. Although the mechanical design and analysis of these concepts have been verified in different stages of the project development (and up to a detailed analysis phase), little work has been done

so far to understand the thermal behavior of the system in the foreseen maintenance environmental conditions. The reference scenario to be considered for heat transfer analysis has been defined by *UKAEA*. Concerning the *RM* mechanical concept, it has been agreed to refer to the *HKM* design, which has been studied in detail in the past and thus all required information is readily available.

The following section describes the layout of the *BB HKM* mover and outlines the motivations behind its development. To give an idea of the concept's scale, the *RM* is approximately 10 [m] high, positioned vertically inside the vacuum vessel and connected to the Upper Port by means of a massive interface flange. The total mass of the mechanism is about 70000 [kg], of which the interface plate accounts for roughly 30000 [kg] (the effectively actuated mass is therefore ~40000 [kg]). The mechanism attaches to and manipulates the Breeder Blanket Segments, which are ~10 [m] tall and have a mass of about 80000 [kg] each.

The final configuration of the structure analyzed in this work (*HKM* mechanism) is shown in *Figure 71*. The component consists of the following main parts:

- Gimbals: spherical hinges that allow the main frame of the mover to rotate with two degrees of freedom (poloidal and toroidal rotations).
- Prismatic joint: located on the central axis, it allows guided translational motion and enables small linear displacements for alignment and adjustment phases.
- Upper spherical joint (Mainbody): located on the central axis, below the gimbals, it allows free three-dimensional rotation while evenly distributing loads.
- Cylindrical joints: two symmetrically placed side joints that allow rotation around an axis combined with sliding along it, thus enabling adjustments during blanket handling.
- Upper main actuators, responsible for tilt and translational movements.
- Kinematic connections transmitting movements to the lower arms.
- Lower rods, which connect directly to the interface plate with the Blanket.
- Lower contact plate, the terminal part directly connecting to the Breeding Blanket.

In addition to the main actuators, the mechanism includes a set of connection plates, joints (spherical, cylindrical, prismatic, and hinge), and

rods that constitute the load-transmission structural elements. The plates act as interfaces between the different subassemblies, the joints provide the degrees of freedom required for motion, and the rods connect the actuators to the lower contact plate with the Breeding Blanket.

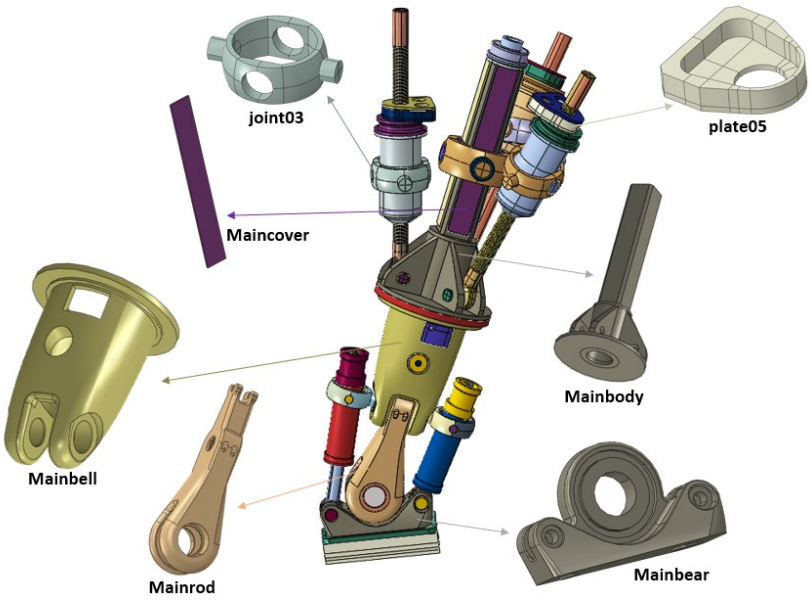

Figure 71 – General components of the FE model (HKM mechanism)

9. Theoretical and Numerical simplified analysis

9.1 Methodology

An analysis pathway was defined in order to develop simplified models and *FE* simulations (with increasing level of complexity and detail), aiming to understand the heat transfer dynamics between the main components (mover, *BB*, and environment), validate the initial assumptions.

The methodology used in this work can be summarized as it follows:

- A simplified lumped mass analytical model (0D model) has been developed, to provide a first rough estimate of the expected maximum temperatures and their temporal evolution, see §9.4 and §9.5.1. Both steady-state and transient simulations have been done, including a sensitivity analysis to the main design parameters, see §9.7;
- The results provided by the lumped mass model are limited to those cases where the temperature inside each part is nearly constant (this condition is satisfied when the reference Biot number is small). If this limitation is not fulfilled, the results are less accurate and more refined modelling is needed. To overcome these limitations, a *1D* heat transfer analytical model has been set, see §9.5.2;
- The lumped mass model has been refined, by removing the hypothesis of fixed temperature imposed to the *BB*: thus, convection to the ambient has been simulated on both the *RM* and *BB* parts, see §9.5.3;
- In addition, a 1D *FE* model has been developed. This model has been used to investigate in detail the impact of several design parameters, running steady state and transient numerical simulations, see §9.6.2 and §9.6.3;

Theoretical and numerical simplified analysis

- A set of parametric *FE* analyses were carried out using as input the original parameters reported in *Table 3*. In particular, variations were considered in the material density, the addition of an insulating layer, and the treatment of the convective heat transfer coefficient h as a function of temperature, see §10.
- Finally, the results achieved in the previous steps have been used to develop the heat transfer model of the *HKM* system. This approach has the goal to predict the expected behavior of a real world manipulator system, subjected to the environmental conditions foreseen for this kind of application. The results provided by the simplified analytical and *FE* models have been used to validate the results produced by this complex, *3D FE* model, see §11.

9.2 Reference data for the thermal analysis

A first approach to the heat transfer analysis of the system involves the creation of a simplified scheme (*Figure 72*), useful for gaining an initial understanding of the behaviour of the system under examination. Thanks to the development of simplified analytical models, solved using *Matlab* software, it was possible to verify the reliability of the results obtained from the more detailed and complex *FE* models.

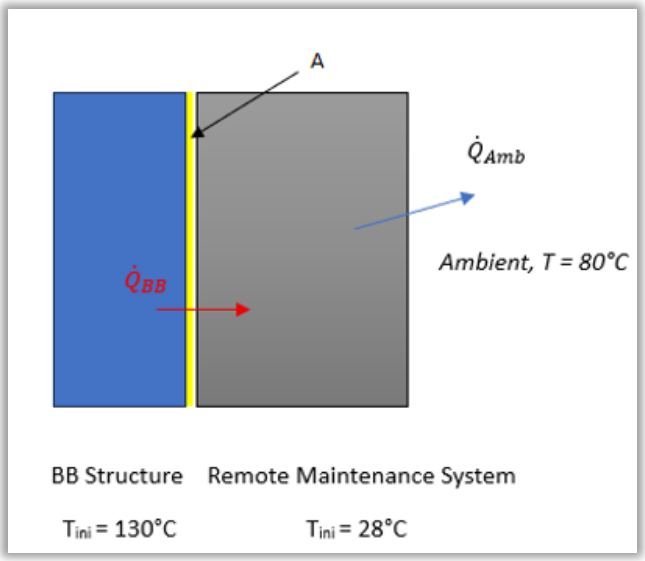

Figure 72 – Initial and simplified model scheme

The *RM* is represented as a block characterized by a uniform temperature and placed in contact with the block representing the *BB,* set at 130 °C. The analysis considers two types of heat transfer: convective exchange between *RM* and the external environment, and conduction occurring at the interface between the two blocks.

Some reference data provided by the *UKAEA* concerning the geometry and material of the components involved are reported below (*Table 3*).

ID	Assumption	Implementation in *FE* Model
1	Mover is a vertical cuboid	Length = 10 m Width = 1 m Thickness = 1 m
2	BB is a vertical cuboid	Length = 10 m Width = 1.5 m Thickness = 1.5 m
3	BB mass 80'000 kg	BB mass = 80'000 kg
4	Mover and BB material is *Structural steel*	Mover density = 7850 kg/m^3 Specific heat capacity = 485 J/kg°C Thermal conductivity = 51.5 W/m°C
5	Initial Mover temperature is 28°C	Initial Mover temperature = 28°C
6	BB temperature is fixed to 130°C	BB temperature = 130°C
7	Ambient temperature is 80°C	Ambient temperature = 80°C

Table 3 – Reference data

9.3 1D FE model description

As a first step, a simplified 1D *FE* study is carried out, designed to provide an initial estimate of the system's thermal behavior. This preliminary approach makes it possible to gain a qualitative understanding of the expected results and to identify potential critical issues before proceeding with the implementation of a more realistic and detailed model. As specified in *Table 3*, the *BB* and the *RM* are modeled in the *FE* as cuboids positioned in contact

with each other (*Figure 73*), and the material chosen for both is structural steel, whose characteristic parameters are reported.

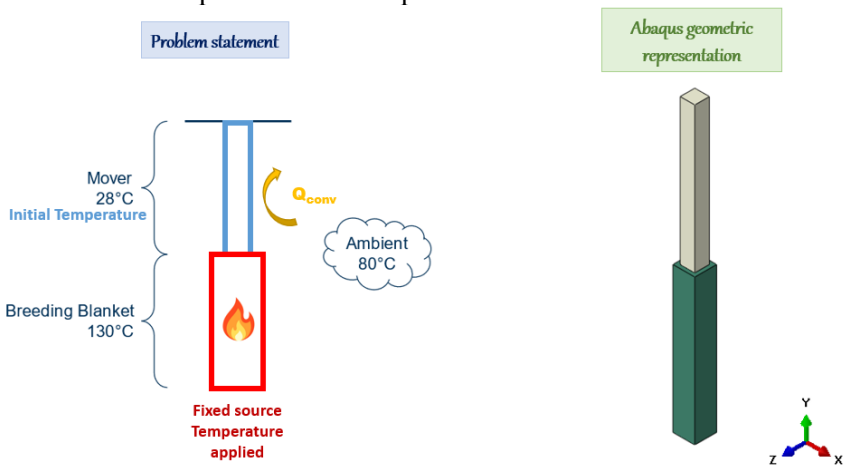

Figure 73 – FE Representation of the baseline problem

The scheme just presented requires the implementation of boundary conditions (*BC*) and initial conditions (*IC*) in the *FE* model. *Figure 74* shows the *BCs* and ICs for the *BB*, while Figure 75 shows those for the *RM*. The temperature of the *BB* block is fixed at 130 [°C], while convection is applied on the top square surface of the *RM* block. In addition, the initial temperature of the *RM* block is set to 28 [°C].

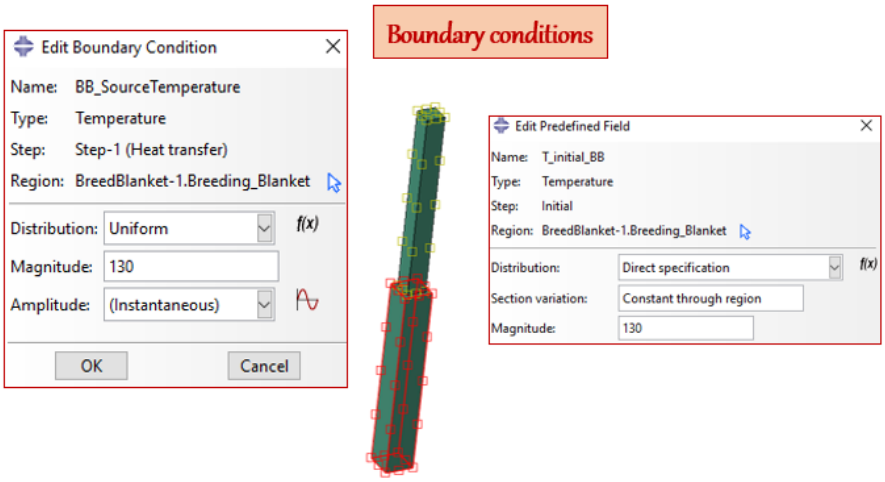

Figure 74 – BC and IC scheme for the Breeding Blanket

Figure 75 – IC scheme for the Remote Maintenance

A thermal conductance (*Figure 76*) is applied at the interface between the two blocks to represent the thermal contact. However, no specific information is available to set a realistic value of thermal resistance at this interface, thus a very high TCC value has been used to basically have the same temperature at both sides of the connection. The natural convection interaction, on the other hand, is shown in *Figure 77*, where a value for the coefficient h of $10\left[\frac{W}{m^2 \cdot K}\right]$ was chosen, considered appropriate as a first attempt based on values commonly used in the literature for free convection. The temperature of the surrounding environment in contact with the body is set to 80 [°C].

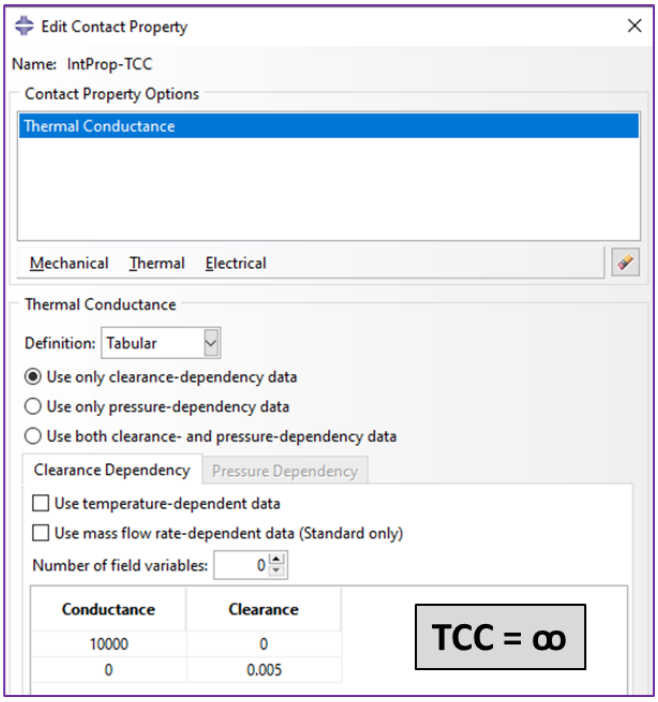

Figure 76 – Thermal conductance set in the FE model

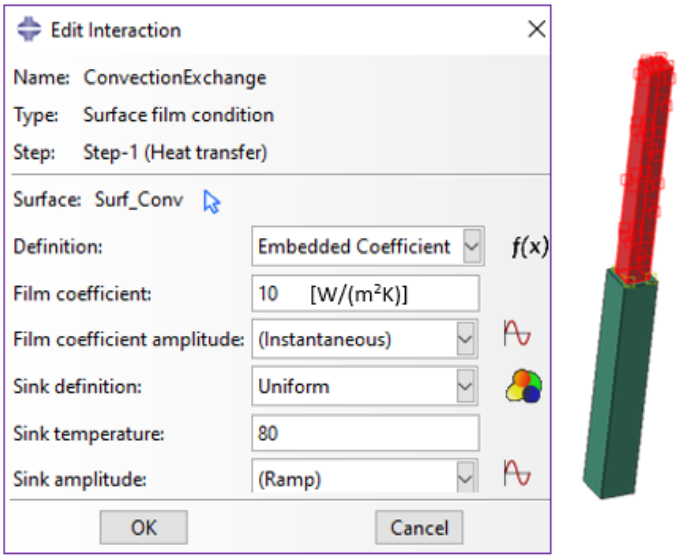

Figure 77 – Natural convection condition set in the FE model

9.4 Steady-state analytical 0D-model

The goal of the analysis consists in verifying the accuracy of the finite element model used to calculate the steady-state temperature of the *RM*. This type of calculation represents the ultimate condition of the system, that is, the thermal equilibrium state established after a sufficiently long time, when transient effects have largely dissipated. Under this condition, the system no longer undergoes significant temperature changes over time and maintains nearly constant values, determined by the balance between incoming and outgoing heat fluxes. The objective of this phase is therefore to analyze the steady-state temperatures predicted by the *FE* model, which the real system will tend to reach and maintain.

The thermal behavior of the *RM* system was investigated using progressively more refined models. The analysis begins with a stationary *lumped* analytical model: in this approach, the body is assumed to be isothermal, meaning that it is assumed that it does not exhibit significant temperature gradients, so its entire mass is represented by a single temperature that evolves over time. The analysis considers the balance between two types of heat transfer mechanisms (eq.(11)) [38]: convective exchange between the *RM* and the external environment, and conduction at the interface between the two blocks.

$$\dot{Q}_{BB} = \dot{Q}_{Amb} \tag{11}$$

The above equality can be represented by the following equation, which describes the energy balance under steady-state conditions (eqs. (12-15)):

$$\frac{k \cdot A}{s} \cdot (T_{BB} - T_{RM}) = h \cdot A_{tot} \cdot (T_{RM} - T_{amb}) \tag{12}$$

$$T_{BB} = T_s \tag{13}$$

$$\frac{k \cdot A}{s} \cdot T_s - \frac{k \cdot A}{s} \cdot T_{RM} = h \cdot A_{tot} \cdot T_{RM} - h \cdot A_{tot} \cdot T_{amb}) \tag{14}$$

$$T_{RM} \cdot \left(h \cdot A_{tot} + \frac{k \cdot A}{s}\right) = \frac{k \cdot A}{s} \cdot T_s + h \cdot A_{tot} \cdot T_{amb}) \tag{15}$$

Expressing everything in terms of the unknown, it is calculated (eq. (16)):

$$T_{RM} = \frac{\frac{k \cdot A}{s} \cdot T_s + h \cdot A_{tot} \cdot T_{amb}}{\left(h \cdot A_{tot} + \frac{k \cdot A}{s}\right)} \tag{16}$$

Theoretical and numerical simplified analysis

- $\frac{k \cdot A}{s} \cdot (T_{BB} - T_{RM})$ is the heat flux by conduction from the *BB* body to the *RM* body [W].
- k is the thermal conductivity of the material connecting *BB* and *RM* [W/(m·°C)]
- A = contact area between *BB* and *RM* [m^2]
- s = thickness of the contact material [m]
- T_s = *BB* Temperature = Sink Temperature [°C]
- $h \cdot A_{tot} \cdot (T_{RM} - T_{amb})$ represents the heat flux by convection between *RM* and the environment [W].
- h = convection coefficient [W/(m^2·K)]
- A_{tot} = total surface area of *RM* exposed to the environment [m^2]

9.5 Transient analytical models

This paragraph analyzes the transient thermal behavior of the bodies, that is, the evolution of temperature over time prior to reaching the steady-state condition. Unlike the steady-state regime, where temperatures are independent of time, during the transient phase temperatures change continuously. To validate the *FE* model used for the transient calculation and the corresponding results, two simplified analytical models are developed.

9.5.1 Analytical lumped 0D model

The study of the thermal transient is then carried out to describe the system's temporal evolution. In this case as well, a lumped approach has been applied. The equation constituting the model used is reported below (eq. (17)):

$$\rho \cdot V \cdot c \cdot \frac{dT}{dt} = \frac{k \cdot A}{s} \cdot (T_{BB} - T_{RM}) - h \cdot A_{tot} \cdot (T_{RM} - T_{AMB}) \qquad (17)$$

By solving the equation numerically (finite difference method) and isolating the unknown on the left-hand side, the following formulation is obtained (eq. (18)):

$$T_{n+1} = T_n + \frac{\Delta t}{\rho \cdot V \cdot c} \cdot \left[\frac{k \cdot A}{s} \cdot (T_{BB} - T_{RM}) - h \cdot A_{tot} \cdot (T_{RM} - T_{AMB})\right] \qquad (18)$$

9.5.2 Analytical heat transfer 1D model

For more detailed analyses, it is necessary to develop a refined *1D* transient analytical model, capable of more realistically describing the ramp-up phase and the spatial temperature distribution. For this purpose, a second analytical model was developed, which numerically solves the heat equation while

simultaneously accounting for both the temporal and spatial dependence of temperature (the latter is not considered in the lumped model). In this case, reference is made to the following differential equation, accompanied by two boundary conditions and one initial condition (eqs. (19-22)):

$$\frac{\partial T}{\partial t} = \alpha \cdot \frac{\partial^2 T}{\partial x^2} \tag{19}$$

$$-k\frac{\partial T}{\partial x}(L,t) = h(T(L,t) - 80) \quad W/m^2\,,\ \forall t \tag{20}$$

$$T(x,0) = 28\,°C\,,\ 0 < x < L \tag{21}$$

$$T(x=0)\ t = 130\,°C\,,\ \forall t \tag{22}$$

9.5.3 Transient model: convection applied to *RM* and *BB*

By removing the prescribed temperature constraint on the *BB*, both blocks are subject to convective heat exchange, and thus their respective temperatures become unknowns. The reference scheme is shown in *Figure 78*. The analytical model therefore requires the solution of two coupled equations (eqs. (23-24)) to simultaneously calculate the temperatures of the two blocks over time.

$$\rho \cdot V_{RM} \cdot c \cdot \frac{dT_{RM}}{dt} = \frac{k \cdot A}{s} \cdot (T_{BB} - T_{RM}) - h \cdot A_{tot} \cdot (T_{RM} - T_{AMB}) \tag{23}$$

$$\rho \cdot V_{BB} \cdot c \cdot \frac{dT_{BB}}{dt} = \frac{k \cdot A}{s} \cdot (T_{BB} - T_{RM}) - h \cdot A_{BB,tot} \cdot (T_{BB} - T_{AMB}) \tag{24}$$

Solving these equations simultaneously, (using the finite difference method) (eqs. (25-26)):

$$T_{RM,n+1} = T_{RM,n} + \frac{\Delta t}{\rho \cdot V_{RM} \cdot c} \cdot \left[\frac{k \cdot A}{s} \cdot (T_{BB,n} - T_{RM,n}) - h \cdot A_{tot} \cdot (T_{RM,n} - T_{AMB,n})\right] \tag{25}$$

$$T_{BB,n+1} = T_{BB,n} + \frac{\Delta t}{\rho \cdot V_{BB} \cdot c} \cdot \left[-\frac{k \cdot A}{s} \cdot (T_{BB,n} - T_{RM,n}) - h \cdot A_{tot} \cdot (T_{BB,n} - T_{AMB,n})\right] \tag{26}$$

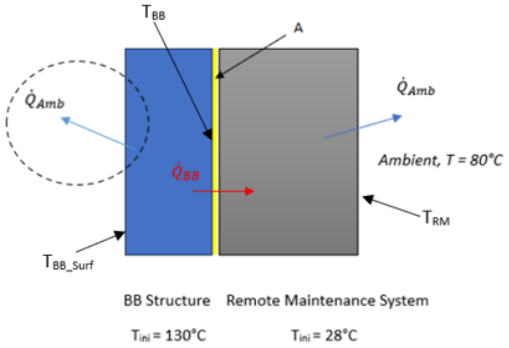

Figure 78 – Double convection model scheme

9.6 Model validation

9.6.1 Adopted parameters for model validation

The masses involved in the model are very large, so the temperature variations of the two blocks require long times (in the order of hours) to achieve steady state conditions. Therefore, during the validation phase, the tabulated density value was reduced by a factor 1000 in order to observe the transient evolution toward steady-state conditions within shorter and more manageable times (thus reducing the calculation time needed to get the results).

The so-called lumped transient models (i.e. each component is described by just one temperature value) correctly reproduce the general trend of the *RM* heating process, but they maintain good accuracy only for small bodies with negligible internal thermal gradients, which ensures compliance with the following inequality eq. (27) [38]:

$$Biot\ number = Bi = \frac{h \cdot L}{k} < 0.1 \tag{27}$$

Where k is the thermal conductivity of the material, h the film coefficient and L represents a characteristic length of the geometry affected by convection; in this case (to place the model in the most critical conditions), L was chosen equal to the block height, i.e., 10 [m]. In the validation phase, the characteristic parameters of the model were adjusted so that the *Biot* number satisfies the required inequality. The total area subjected to convection, A_{tot}, was artificially reduced from a value of 41 [m²], corresponding to the entire lateral surface, to 1 [m²], corresponding only to the top square surface, to represent the one-dimensional behavior more explicitly in the *FE*. Consequently, the convection heat transfer coefficient was set to 41 [W/(m²·K)]. Based on the order of magnitude of the product $h \cdot L$, an arbitrary conductivity value of 10000 [W/m·K] was chosen to satisfy the inequality. The starting idea was to preserve the same product between the area A_{tot} and the convective coefficient h in order to represent the same heat flux of the original model. However, this would have required h to be equal to 410 [W/ m²·K] (i.e. ten times higher than the one used in the following calculations), which would have not satisfied the inequality of the Biot number.

In *lumped* models, it is necessary to clarify the definition of the body's characteristic dimension. The actual height of the *RM* body is 10 meters, but in the lumped model an effective value of 5 meters is used. This is because the lumped model calculates an average temperature over the body's volume, assuming that the temperature is not uniformly distributed, unless the Biot

number assumes very small value. Using half the real height allows for a more realistic representation of the spatial average of the temperature on the body, without considering local details of the thermal distribution. A summary of the points discussed in this paragraph is presented in *Table 4*.

Specific heat capacity ***c*** **[J/kg°C]**	**Characteristic length** ***L*** **[m]**	**Convection Area** A_{tot} **[m²]**	***RM*** **height** ***s*** **[m]**
485	10	1	5
Thermal conductivity ***k*** **[W/(m·K)]**	**Convection coefficient** ***h*** **[W/(m²·K)]**	**Material density ρ [kg/m³]**	
10’000	410	7.85	

Table 4 – Parameters used during the validation phase

From the combination of values, the Biot number is equal to 0.041 [-].

9.6.2 Steady-state results comparison

Due to the considerable size of the components involved, the substantial difference between the contact area of *BB* and *RM* and the surface area of *RM* exposed to convection, the equilibrium temperature of *RM* in the steady-state case is expected to be only slightly higher than the ambient temperature, *i.e.*, $T_{amb} = 80$ [°C].

This, however, does not occur in the *1D FE* models, because of modifications made to the operating parameters, in particular the assignment of a remarkably high value to the parameter *k*, which results in a significant conduction effect. Consequently, the *RM* temperature reaches, according to the analytical calculation (eq. (16)), the value $T_{RM} = 121.49$ [°C].

It can be observed from *Figure 79* that the steady-state *FE* result at the highlighted point, representative of the *RM* midpoint, is nearly identical to that predicted by the analytical model. Indeed, the steady-state *FE* analysis yields a temperature of 121.84 [°C].

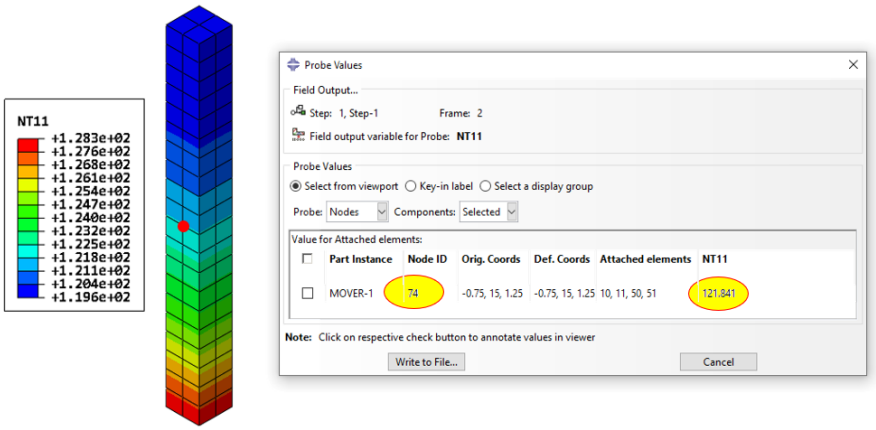

Figure 79 – Nodal temperature [°C] computed by the steady-state analysis

9.6.3 Transient results comparison

The good agreement between the results of the lumped (§9.5.1) and distributed (9.5.2) analytical models and those obtained from the *FE* analysis confirms the validity of the simplified *FE* approach for transient predictions (*Figure 80*).

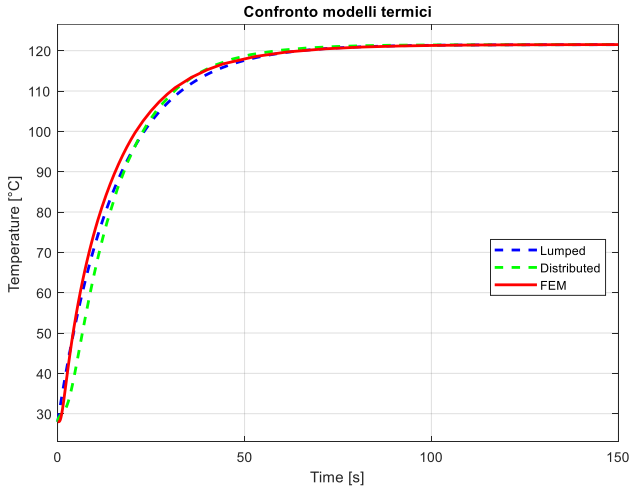

Figure 80 – Nodal temperature [°C] resulting by the transient analysis and extracted in the RM midpoint

This matching of the results was made possible by manipulating the input parameters (§9.6), which allowed the lumped model to be used while satisfying the *Biot* number inequality (eq. (27)). The *1D* distributed heat transfer analytical model basically gives the same results as the 1D *FE* model.

9.6.4 Double convection transient results comparison

In the *FE* model, the only modification concerns the prescribed temperature boundary condition at the interface between the two blocks (*Figure 74*). This is replaced by extending the second boundary condition, which will apply convective heat transfer to the *BB* surface as well (*Figure 81*).

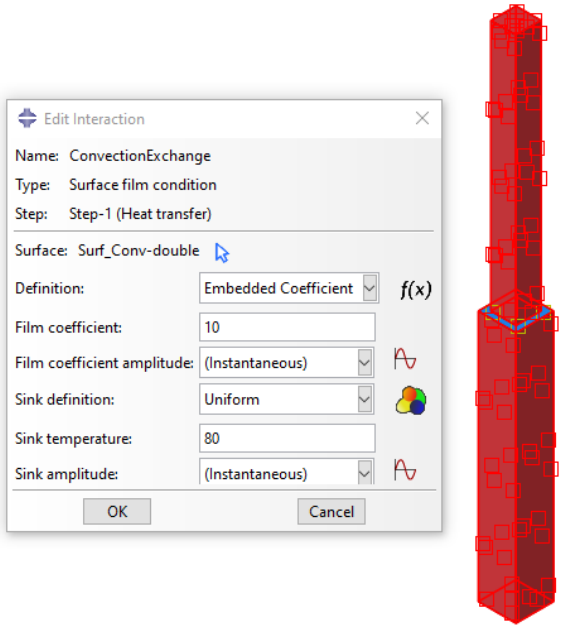

Figure 81 – Detail of the external surface exposed to convection

In this analysis, the total area exposed to convection was no longer modified since the focus is on the overall temperature variation of both the bodies, so the original value of $h = 10$ [W/ m²·K] was set.

The lumped analytical solution shown below (*Figure 82*) indicates that the temperatures of the two blocks converge toward 80 [°C]. This result was largely expected, as the only heat source present in this model configuration is the ambient temperature. Furthermore, the curves show a slight deviation from those obtained from the simplified *FE* model, which tends to diminish as the *Biot* number decreases.

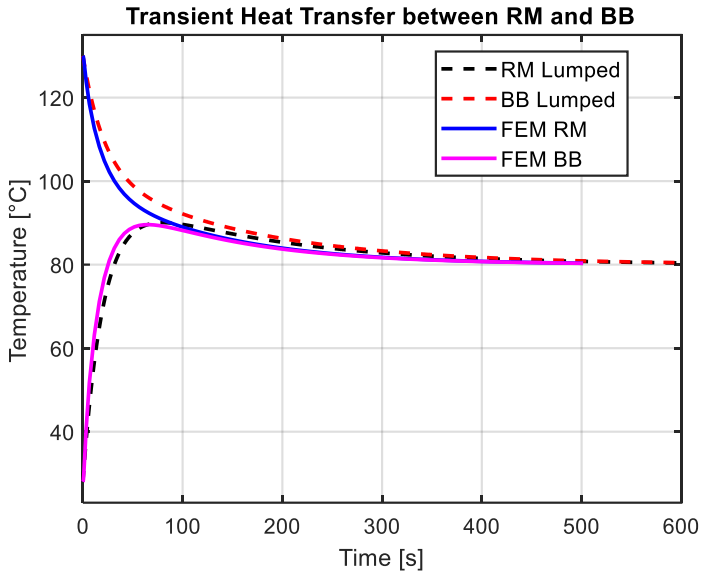

Figure 82 – Comparison of the obtained results during the transient phase between analytical model and FE model

9.7 Sensitivity analysis

After developing the simplified steady-state models, a sensitivity analysis was conducted on the main parameters influencing the model's energy balance, particularly the behavior of the *RM*. The aim of this phase is to assess how and to what extent uncertainties in the input data (*e.g.*, heat transfer coefficients, thermal conductivity, contact areas, etc.) can affect the steady-state temperature of the mover. In other words, this step evaluates the robustness of the model and identifies the parameters to which the results are most sensitive, thus highlighting which require particular attention during the design phase or in subsequent model refinements. The analysis has been carried out by using the simplified lumped mass heat transfer model.

Initially, the thermal conductivity was varied (*Figure 83*) over a wide range, from 20 to 150 [W/mK]. This range covers typical values of structural materials commonly used in industrial applications, such as titanium, steel, or aluminum. The purpose is to verify how the material's heat transfer capability influences the mover's equilibrium temperature. The results show a linear dependence on this parameter.

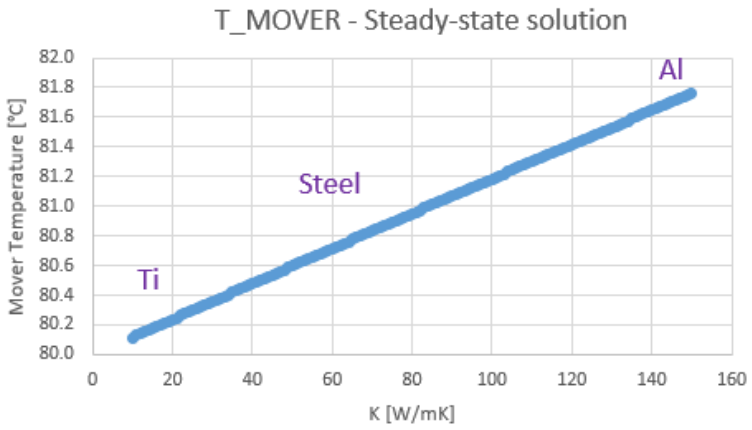

Figure 83 – Influence of the parameter K on the steady-state temperature of the RM

In the second scenario (*Figure 84*), the system's behaviour was analysed as a function of the surface convective heat transfer coefficient *h*, over a range that includes typical values for natural convection. This parameter controls the effectiveness of heat exchange between the mover and the environment, and its variation allows for the evaluation of how much convection can affect the final temperature, whether natural or forced. As can be observed, the value of *h* has little influence on the results. This is because convective heat transfer is already very high compared to conductive transfer, and even relatively small values of *h* tend to bring the *RM* temperature close to the ambient temperature.

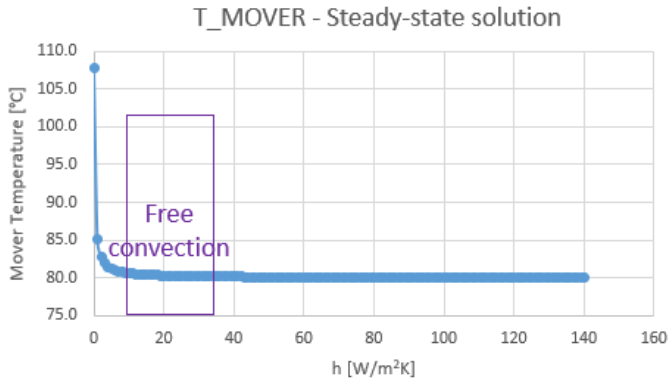

Figure 84 - Influence of the parameter h on the steady-state temperature of the RM

Subsequently (*Figure 85*), the value of s, the characteristic distance between the two bodies appearing in the denominator of the conductive term kA/s, was varied. This parameter represents, in a simplified form, the resistance to heat transfer by conduction between the mover and BB: larger values of s correspond to higher resistance and thus a lower conductive heat flux. The analysis allows evaluating the sensitivity of the mover's temperature to uncertainties associated with this characteristic distance. The largest variations are observed for low values of s.

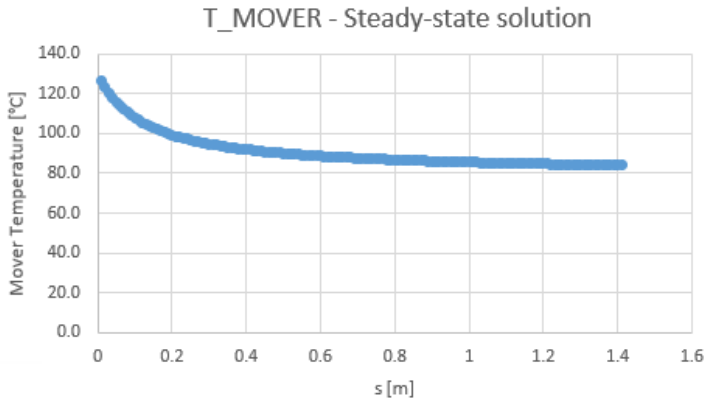

Figure 85 - Influence of the parameter s on the steady-state temperature of the RM

In addition, the effect of the external surface area exposed to convective heat transfer was studied (*Figure 86*). The reference case considers a value of 41 [m²], calculated from the previously reported geometric dimensions. As the wetted surface area increases, the convective resistance decreases and the mover's temperature tends to converge toward the ambient temperature, highlighting the role of geometry in enhancing heat dissipation.

A very pronounced effect is due to the variation of the contact area at the interface between the two components (*Figure 87*). As the area increases, the mover's steady-state temperature rises significantly, since the incoming heat flux from the *BB* (whose temperature is fixed at 130 [°C] in the steady-state case) increases.

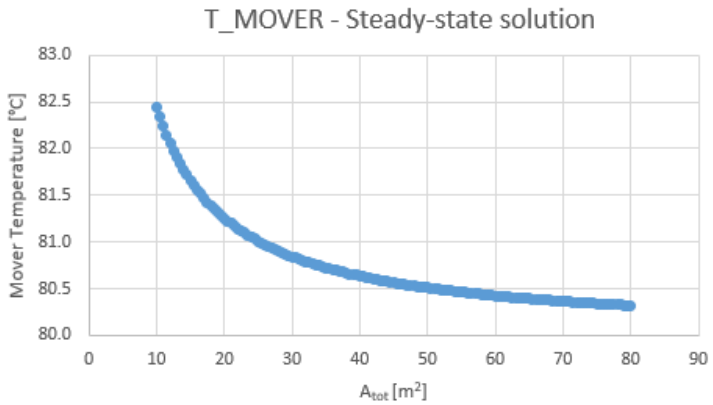

Figure 86 - Influence of the parameter A_{tot} on the steady-state temperature of the RM

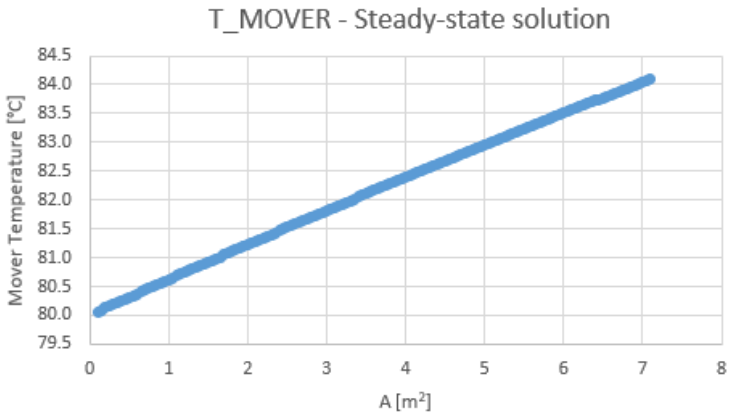

Figure 87 - Influence of the parameter A (contact area) on the steady-state temperature of the RM

Finally, starting from eq. (16) and adding on the right side the term related to internal heat generation in the mover (eq. (28)), the heating effect generated by the actuator motors—which in the real case enable the regular operation of the mover—is studied (*Figure 88*).

$$T_{RM} = \frac{\frac{k \cdot A}{s} T_s + h \cdot A_{tot} \cdot T_{amb}}{\left(h \cdot A_{tot} + \frac{k \cdot A}{s}\right)} + \frac{\dot{Q}_{int}}{\left(h \cdot A_{tot} + \frac{k \cdot A}{s}\right)} \tag{28}$$

It can be observed that, as the generation increases, the mover's temperature naturally rises, showing a linear trend. In this case, the value of $\dot{Q}_{int}$ is expected to be around 2500 [W]. This value was estimated by

considering 50% of the stall power deliverable by the motor. This approach has been agreed in accordance with guidelines by *UKAEA*. The overall effect in terms of temperature increase results in a few degrees.

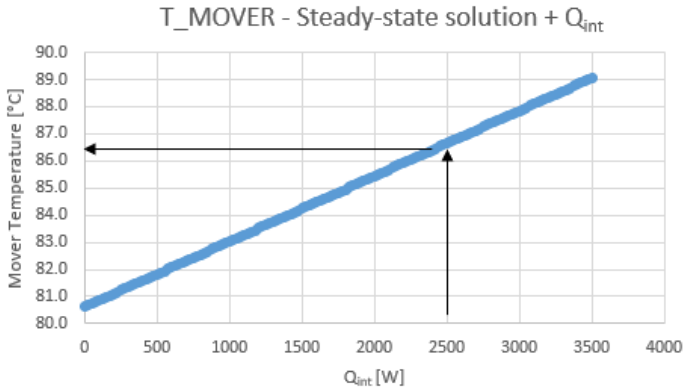

Figure 88 - Influence of the parameter Q_{int} on the steady-state temperature of the RM

10. FE 1D simplified model analyses

Once the simplified *1D FE* model was validated through comparison with analytical calculations and sensitivity analyses, a series of tests was initiated to explore the thermal behavior of the system under different operating configurations. In the previous chapter, ad hoc coefficients were employed in the various analyses to validate the model, whereas in this chapter the realistic design data shown in *Table 3* are used.

First, a steady-state analysis was conducted, followed by parametric *FE* tests to study the model's response under different configurations. The first test varied the density of the material constituting the *RM*, aiming to evaluate the effect of a potential increase in component mass on the thermal transient and equilibrium temperature. Subsequently, the role of the convective heat transfer coefficient was investigated, estimated more accurately as a function of the surface temperature involved, according to correlation models available in the literature for a vertical plate in natural convection. This approach allowed overcoming the initial assumption of a constant h, providing a more realistic representation of the phenomenon. Finally, analyses were performed varying the thickness of an insulating layer inserted between the *RM* and the external environment. Three different insulation thicknesses were considered, in order to investigate the effectiveness of each solution in limiting conductive heat transfer and thereby altering the heating dynamics of the mover.

The simulations were carried out over a transient period of 30 hours, aiming to identify the times at which the *RM* temperature exceeds the established limit of 40 [°C]. This threshold temperature was selected by *UKAEA* as a critical limit, since any exceedance could compromise the performance of the motors.

10.1 Steady-state analysis

In the previous chapter §9, geometric and material parameters were adjusted to validate the analytical models used. In this chapter, however, once the accuracy of the developed model was ensured, all analyses are performed using the parameters of the actual system. The steady-state analysis yields the results shown in *Figure 89*, indicating that the average temperature of the mover will stabilize around 80 [°C].

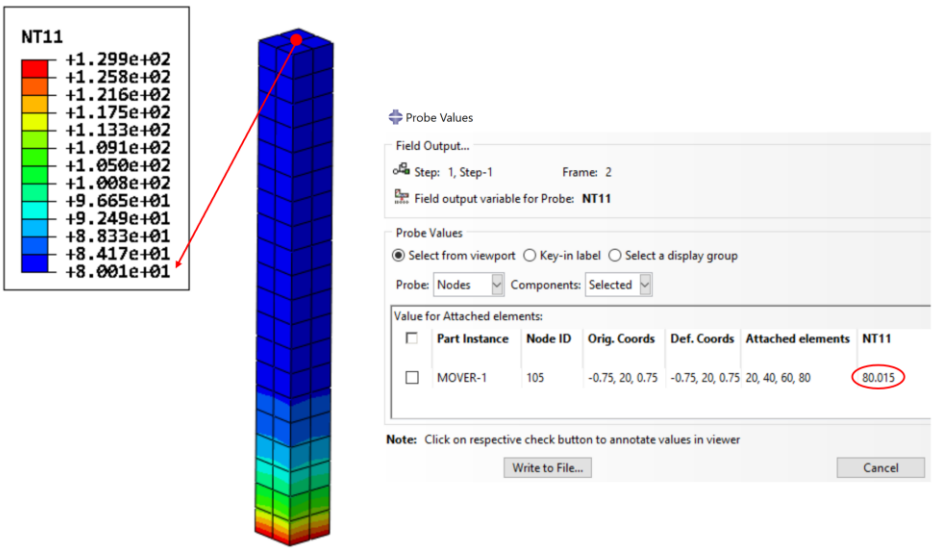

Figure 89 – Steady-state analysis results

10.2 Transient Analysis

The transient analysis, on the other hand, shows the temperature distribution depicted in *Figure 90*, with a focus on the *RM*. Temperatures range from 62 to 130 [°C], while the temperature at the midpoint of the model reaches 63 [°C]. After 30 hours of transient, this configuration still shows results far from steady-state conditions, as indicated by the increasing trend of the curve.

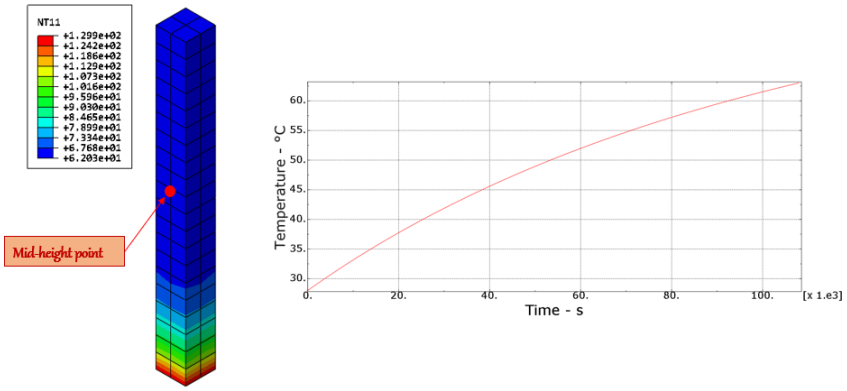

Figure 90 – Distribuzione termica [°C] per l'analisi transitoria sul RM

10.3 Comparison with heat transfer analytical model

This paragraph presents the results obtained from the analytical models, both steady-state and *1D* transient. *Figure 89* shows the result of the steady-state *1D FE model*, in which the parameters from *Table 3* were used: the result at the top of the mover is T = 80.015 [°C], a value slightly lower than that predicted by the lumped model (§9.4), which is 80.62 [°C]. This discrepancy is due to the fact that, when using the original parameters from *Table 3*, the *Biot* number does not satisfy the inequality of (eq. (27)) and the accuracy of the lumped model starts degrading. However, it is worth noting that even a very simplified calculation based on a lumped model is fully capable of predicting the steady-state temperature of the mover (when a sufficient distance from the interface with the *BB* is considered). For the same reason, the transient model (§9.5.1) fails to provide the correct results of *Figure 90*: in this case the temperature ramp-up phase calculated by the lumped model shows even a larger discrepancy.

The *1D* analytical model (§9.5.2) was developed to improve the accuracy of the analytical predictions and validate the simplified *FE* presented in §9.3. For this purpose, a model was considered in which convection was applied only to the upper square surface of the mover. The same procedure was applied in this case: by reducing the convection area from 41 to 1 [m²], the inverse adjustment was made for *h*, which was increased from 10 to 410 [W/m²·K] (so that the product convective area times *h* remains the same).

From the *1D* analytical model, using the original model parameters, the results shown in *Figure 91* were obtained together with the corresponding *FE* results. The figure shows the path of nodes from which the results were extracted after 30 hours of transient simulation, and the two curves, *FE* and

analytical, are almost identical. In *Figure 92* the evolution of the *RM* temperature at its midpoint is reported from both the *FE* and the *1D* analytical solution, showing very similar results with only a negligible difference.

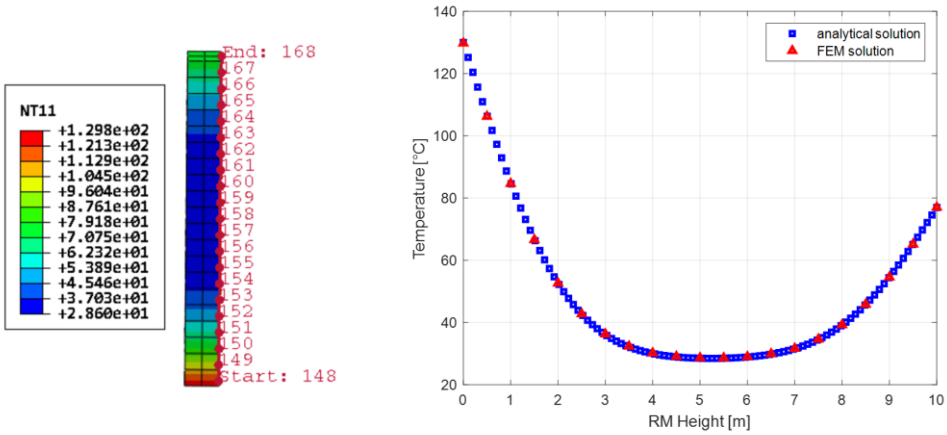

Figure 91 – Comparison between the FE and analytical 1D resulting RM temperature along the red vertical path

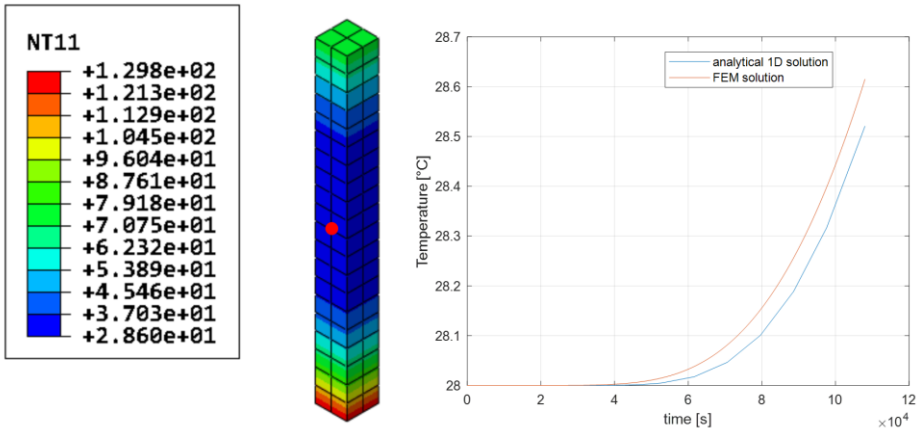

Figure 92 – RM Temperature variation exhibited in the midpoint

10.4 Double convection and Film coefficient analysis

Among the various geometric configurations considered in the literature for external natural convection, the case of a flat vertical plate at uniform temperature is one of the most studied reference scenarios, both for its geometric simplicity and for its relevance in numerous engineering applications. The vertical plate in natural convection serves as a reference

model particularly close to the case analyzed in this work: indeed, the *RM* block exchanges heat with the environment primarily along its vertical side surfaces.

10.4.1 Vertical plate model and h(t) calculation

In the literature, the convective behaviour of a flat vertical plate at uniform temperature has been extensively studied using empirical correlations based on dimensional analysis and experimental data. Among these, one of the most widely used and versatile is the correlation proposed by *Churchill and Chu* [39], which allows estimating the convective heat transfer coefficient h as a function of both the surface temperature and the surrounding ambient temperature (air properties in [40]). This correlation has the advantage of being applicable to any flow regime, without limitations on the Rayleigh number range (eq. (29)), providing a continuous description of the transition from laminar to turbulent convection. In this way, a more realistic assessment of the dependence of h on the temperature difference $\Delta T = T_{wall} - T_{amb}$, can be obtained, overcoming the simplified assumption of a constant convective coefficient. Specifically, the formulation proposed by *Churchill* and *Chu* provides the average *Nusselt* number (eq. (30)) for a vertical plate of characteristic height L as a function of the Rayleigh number and the *Prandtl* number Pr (eq. (31)):

$$Ra_L = \frac{g \cdot \beta \cdot (T_{wall} - T_{amb}) \cdot L^3}{\nu \alpha} \tag{29}$$

$$Nu_L = \left[0.825 + \frac{0.387 \cdot {Ra_L}^{1/6}}{\left((1 + (\frac{0.492}{Pr}))^{\frac{9}{16}} \right)^{8/27}} \right]^2 = \frac{\bar{h} L}{k} \tag{30}$$

$$Pr = \frac{\mu \cdot c_p}{k} \tag{31}$$

Where:

- g = gravitational acceleration *[m/s²]*
- β = air thermal expansion coefficient *[1/K]*
- $T_{wall} - T_{amb}$ = temperature difference between surface and external ambient *[°C]*
- L = characteristic length of the plate *[m]*
- ν = fluid kinematic viscosity *[m²/s]*
- α = thermal diffusivity of the fluid *[m²/s]*
- c_p = specific heat at constant pressure *[J/(kg·K)]*
- μ = air dynamic viscosity *[Pa·s]*
- k = thermal conductivity of the fluid *[W/(m·K)]*.

Through the Rayleigh number, it is possible to determine the Nusselt number and thus the convective heat transfer coefficient *h* as a function of the surface temperature of the component under study (*Figure 93*). This formulation allows for an accurate description of the natural convection mechanism in the present case, where the *RM* block absorbs heat from the environment through its vertical side surfaces, ensuring a modelling approach consistent with the actual physical phenomena. The graph in *Figure 93* is derived from this modelling.

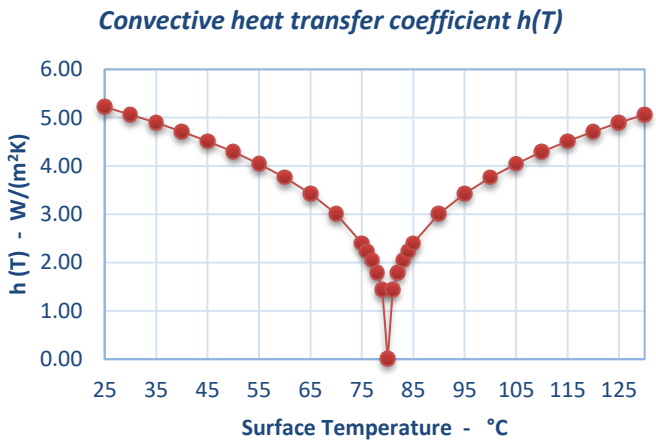

Figure 93 – Trend of the parameter h(T) as a function of the temperature of the surface involved in the exchange

It can be observed that at the point where the surface temperature equals the ambient temperature, the convective coefficient is predicted to be zero. Additionally, the coefficient *h* tends to increase as the surface temperature deviates from the value of the ambient temperature, i.e. 80 [°C].

10.4.2 FE Results - h(t) case

Figure 94 shows the results of the transient analysis in terms of nodal temperatures and the corresponding local values of the convective coefficient. It is worth noting that where the temperature contour plot appears green (around the ambient temperature of 80 [°C]), the convective coefficient is very low, represented by the blue-colored areas (*FILMCOEFF* plot). In *Abaqus*, the film coefficient *h* can be defined as temperature-dependent and is updated incrementally as the wall temperature evolves.

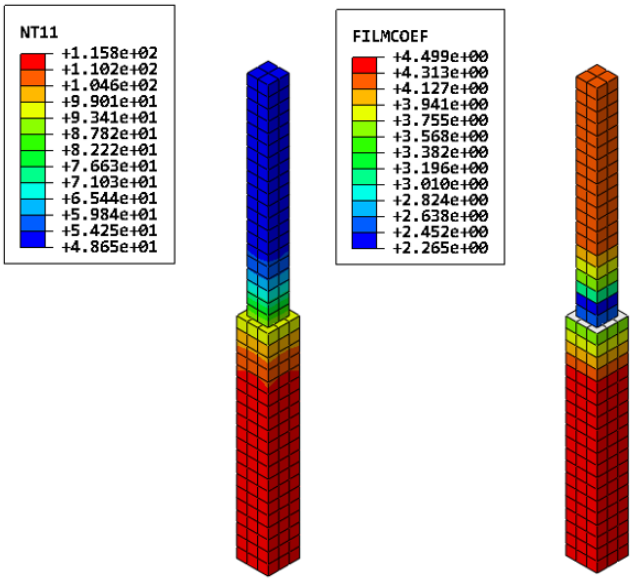

Figure 94 – Nodal temperatures [°C] and h(t) [W/m²K] resulting from the simplified FE analysis.

Figure 95 shows the results for the intermediate points of the two bodies, as illustrated in the previous chapter §9.6.2 during the validation phase. The blue curve represents the temperature of the *BB*, starting from 130 [°C] and cooling down. In contrast, the red curve represents the temperature of the Mover, increasing from the initial temperature of 28 [°C]. In *Figure 96*, the results obtained with a constant coefficient of $10\left[\frac{W}{m^2K}\right]$ are compared with those obtained using the approach $h = h(T)$. These results highlight that the mover's temperature takes approximately 14 hours to exceed 40 [°C] when using the temperature-dependent coefficient (blue curve), whereas it takes around 7 hours when using a constant h (red curve).

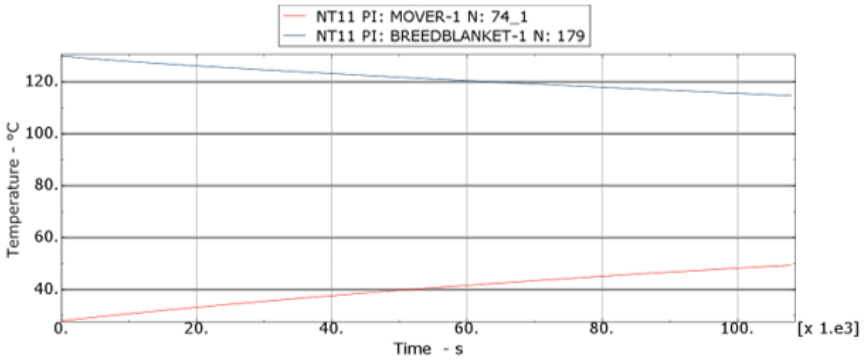

Figure 95 – Result obtained by extrapolating the values from the midpoints of the two bodies

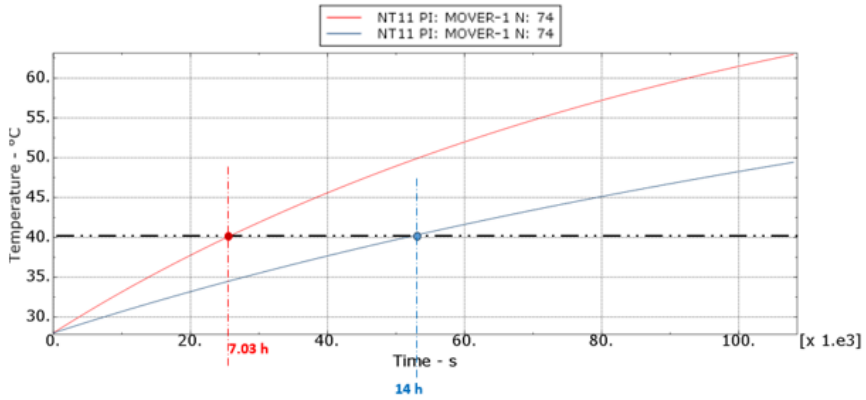

Figure 96 – Time required to exceed 40 [°C] in the two analyzed cases.

10.5 Double convection and scaled RM density analysis

The impact of material density on the resulting temperature of the Mover after a 30-hour transient was studied using the simplified model, focusing on the midpoint of the component. This approach allows understanding how variations in material properties influence the thermal behavior of the component over a prolonged period. In this specific case, decreasing the material density corresponds to using lighter materials. This reduces the volumetric heat capacity, so the less dense material stores less heat and heats up more quickly. *Figure 97* shows that, for analyses conducted with three different densities, the times required to reach the 40 [°C] threshold are 3.65 hours for a density of 4000 $\left[\frac{kg}{m^3}\right]$, 5.34 hours for a density of 6000 $\left[\frac{kg}{m^3}\right]$ and 7.03 hours when using the real steel density.

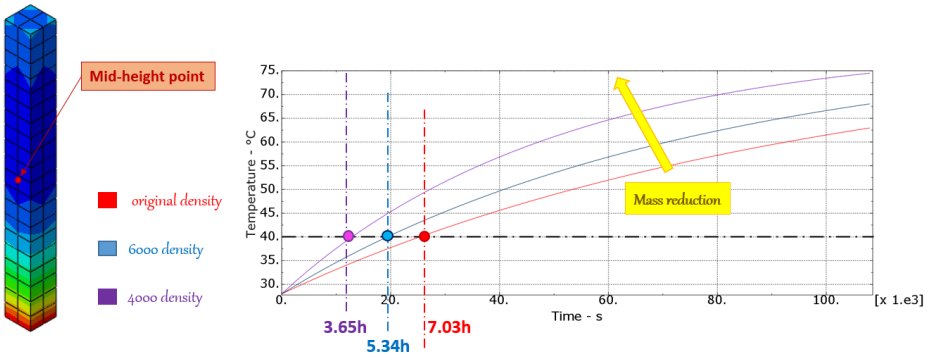

Figure 97 - Time required to exceed 40 [°C] in the three analyzed cases.

10.6 Double convection and insulation layer analysis

In the final configuration (*Figure 98*), an insulating layer was introduced in three different thicknesses: 2 [mm], 5 [mm], and 10 [mm]. The chosen material is *G-10-CR* (fiberglass), characterized by the following properties:

- Thermal conductivity: 0.8 $\left[\frac{W}{mK}\right]$
- Density: 1800 $\left[\frac{kg}{m^3}\right]$
- Specific heat: 1260$\left[\frac{J}{kg \cdot K}\right]$

The layer is positioned exactly at the interface between the *BB* and *RM* blocks and serves as an additional element between the components.

FE 1D Simplified model analyses

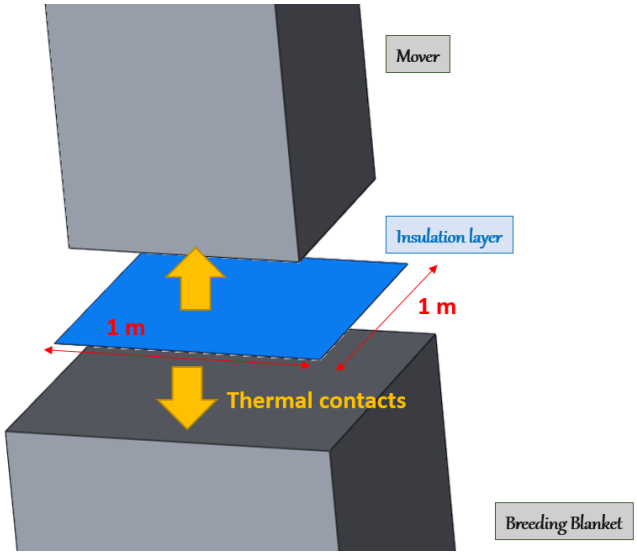

Figure 98 – Schematic representation of the model with insulating layer included

The thermal connection between the insulating layer and each block was modeled using thermal conductance (although the *TCC* has been set to a very high value), similarly to the previous simulations where direct contact existed between the two blocks. This configuration allows evaluating how the introduction of an insulating layer could affect heat transfer between the blocks and, consequently, the resulting temperature of the Mover. The analysis of the three thicknesses allows assessing the system's sensitivity to the additional thermal resistance introduced by the layer, highlighting the impact of insulating materials of different thicknesses on the overall thermal behavior. *Figure 99* shows that the application of the insulating layer delays the achievement of 40 [°C] by up to 30 minutes at the most thermally stressed point of the model.

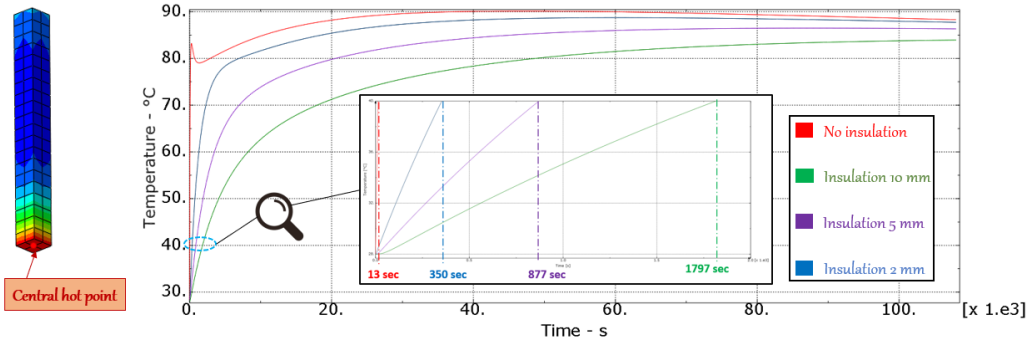

Figure 99 – Time required to exceed 40 [°C] in the four analyzed cases

The overall effect along the height of the Mover is rather small, as can be seen in *Figure 100,* with the intermediate region of the component stabilizing around 63 [°C] in all of the analyzed cases.

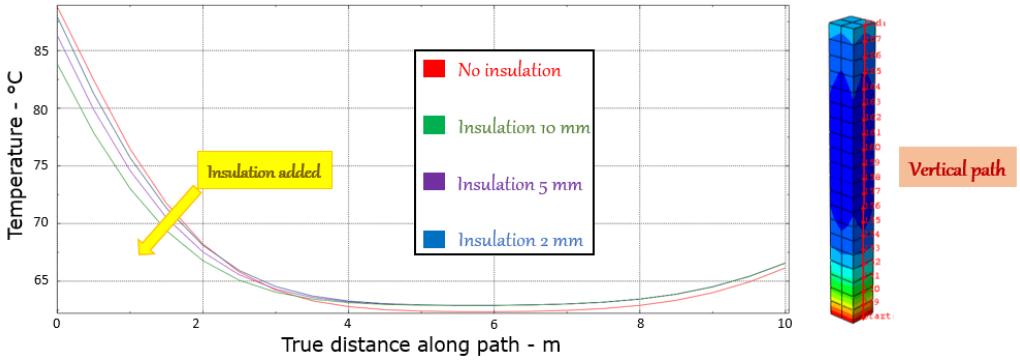

Figure 100 - Overall effect obtained following the addition of the insulating layer

10.7 Preliminary results summary

The analyses conducted, both through simplified *FE* models and analytical models (lumped mass and *1D* models), allowed a detailed understanding of the thermal behavior of the *RM-BB* system. The comparison between steady-state and transient analyses clearly shows that convection is the prevailing heat transfer mechanism, while conductive heat transfer plays a significant role mainly locally, next to the interface between the *RM* and the *BB*. This behavior is consistent and observed in the more sophisticated and complete model analyzed in the subsequent phase of the study, see chapter 11.

The scenario with low density material accelerates the heating of the *RM* due to the reduced volumetric heat capacity, whereas the introduction of an insulating layer between the blocks moderately delays the exceedance of the critical 40 [°C] threshold, without significantly affecting the overall temperature distribution along the component's height. Sensitivity analyses highlighted that certain parameters, particularly the contact area and internal heat generation, have the greatest impact on thermal behavior, providing useful guidance for potential design interventions aimed at optimizing heat dissipation.

Overall, the results confirm the validity of the simplified *FE* model as a reliable predictive tool for assessing the thermal dynamics of the *RM* under various operating conditions. Good correlation with the simplified analytical models developed in this study has been achieved.

FE 1D Simplified model analyses

11. HKM FE modelling: real case study

11.1 Overview

This *3D* analysis originates from the evolution of the previously developed simplified models, progressing toward a more realistic representation of the system composed of the *BB* and *RM* in contact (*Figure 101*). The detailed model considers the following hypotheses:

- the Blanket, initially treated as a constant-temperature source at 130 [°C] and subsequently as a body with a defined initial temperature;
- the Mover, starting from 28 [°C];
- the possible presence of an insulating layer made of G-10-CR, modeled with different thicknesses (2 [mm], 5 [mm], and 10 [mm]).

The FE analysis involves a series of key aspects:

- Components modeling;
- Loads modeling;
- Analysis of different configurations and scenarios (e.g. with or without internal heat generation);
- Calculation of the resulting temperatures in the different configurations.

The main objective of this analysis is to study in detail the temperature distribution within the Mover, in order to assess whether the system might reach critical conditions for the materials used or, alternatively, to estimate the

time, expressed in hours, required for the temperature to exceed the considered critical threshold. In this initial phase, a safety limit of 40 [°C] was set. Particular attention was given to two areas deemed significant: the contact plate with the *BB*, representing the most thermally stressed region, and a point in the central bell, identified as representative of the average behavior of the entire model.

11.2 Mesh description

Regarding the finite element discretization, the model components were geometrically simplified by removing holes, fillets, and small details that are negligible for *FE* analysis. This approach allowed for a reduction in model complexity without compromising the significance of the results. Thanks to this simplification, the main components were assigned a structured hexahedral mesh, using *DC3D8* solid elements, which ensure high accuracy in evaluating temperature distributions. For some components with more complex geometries, such as the "bell" and the component referred to as "main body" (*Figure 71*) a partially tetrahedral mesh was preferred. In these cases, at least partially, *DC3D4* tetrahedral elements were used, which allow easier discretization of irregular shapes while maintaining an adequate level of precision for thermal analysis.

Overall, the model is characterized by (*Figure 101)*:

- 937’450 DC3D4 tetrahedral linear elements
- 214’408 DC3D8 hexahedral linear elements

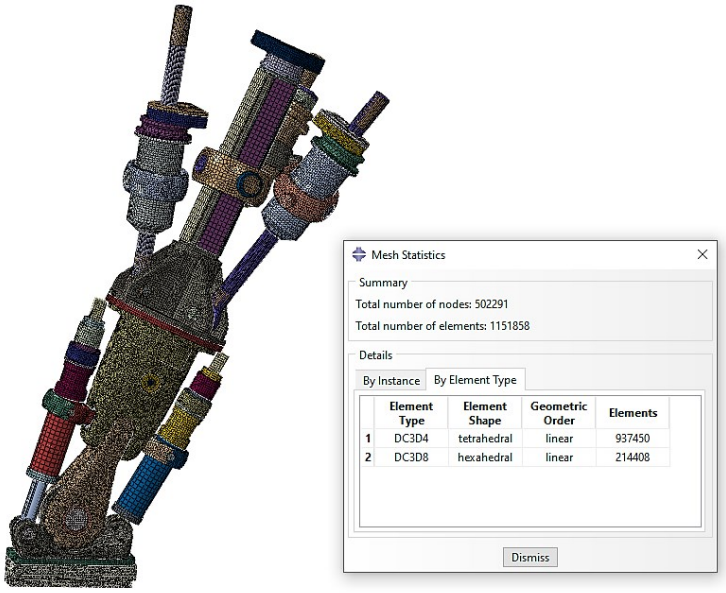

Figure 101 – Diagram of the actual 3D model analyzed

11.3 Material properties definition

Regarding the materials used in the model, three distinct types were employed (*Figure 102*).

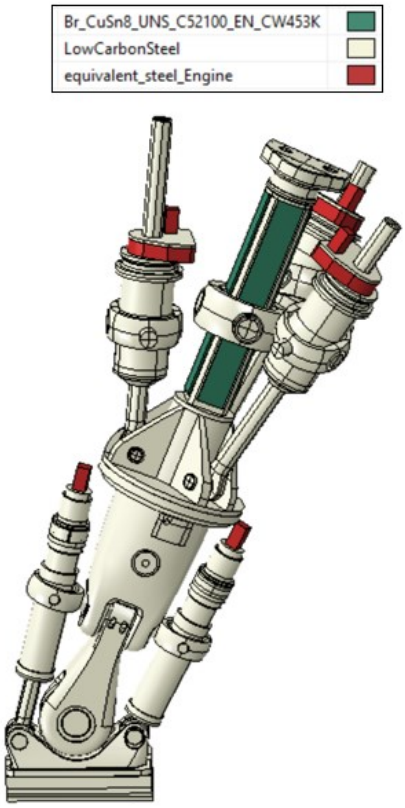

Figure 102 – Details of the materials characterizing the analysis

The vast majority of components were characterized as Structural steel, a material chosen for its mechanical and thermal properties suitable to accurately represent the structural and thermal behavior of the system. Exceptions are the plates on the central shaft of the model, for which bronze was used, as it better represents the real conditions due to its specific thermal conductivity and contact resistance properties, and the motor blocks, consisting of the motor and gearbox in the final stages of the analysis. For simplicity, the latter were modeled as parallelepiped blocks, and to ensure physical consistency in the modeling, an equivalent density was calculated such that the weight of each motor-plus-gearbox block equals 21 [kg] (as indicated in the manufacturer datasheet). In summary, the properties of the materials used are reported in the following *Table 5* [41]:

Material	Thermal Conductivity $\left[\frac{W}{m \cdot K}\right]$	Specific heat $\left[\frac{J}{kg \cdot K}\right]$	Mass density $\left[\frac{kg}{m^3}\right]$
Structural Steel	51.5	485	7850
Equivalent Steel Engine	51.5	485	3970
Bronze CuSn8	67	377	8790
G-10-CR	0.8	1260	1800

Table 5 – Material properties

11.4 Boundary conditions

Regarding the boundary conditions, the model was analyzed considering constraints designed to replicate the operational scenario as accurately as possible. In particular, the four spherical joints (Gimbals), located on the upper shafts of the Mover, were constrained to a support plate, which was not modeled in this analysis. This plate was assumed to be at an ambient temperature of 80 [°C], as it is in direct contact with the internal atmosphere of the vacuum chamber, from which it assumes its characteristic temperature.

Another key condition in the analysis concerns the contact plate at the base of the Mover: a temperature of 130 [°C] was applied to the lower surface of this plate, corresponding to the expected value for the Breeding Blanket with which the Mover is in direct contact. This choice allows for a realistic evaluation of the heat transfer from the Blanket to the Mover, identifying the most thermally stressed areas and monitoring the temperature evolution over time. *Figure 103* and *Figure 104* show the boundary conditions applied and the corresponding zones of application.

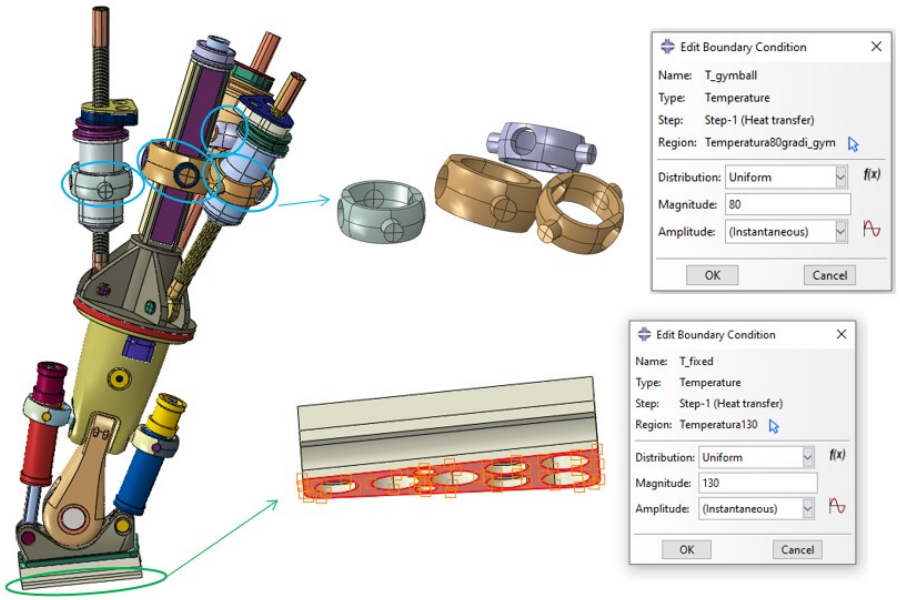

Figure 103 – BCs applied to the modeled components

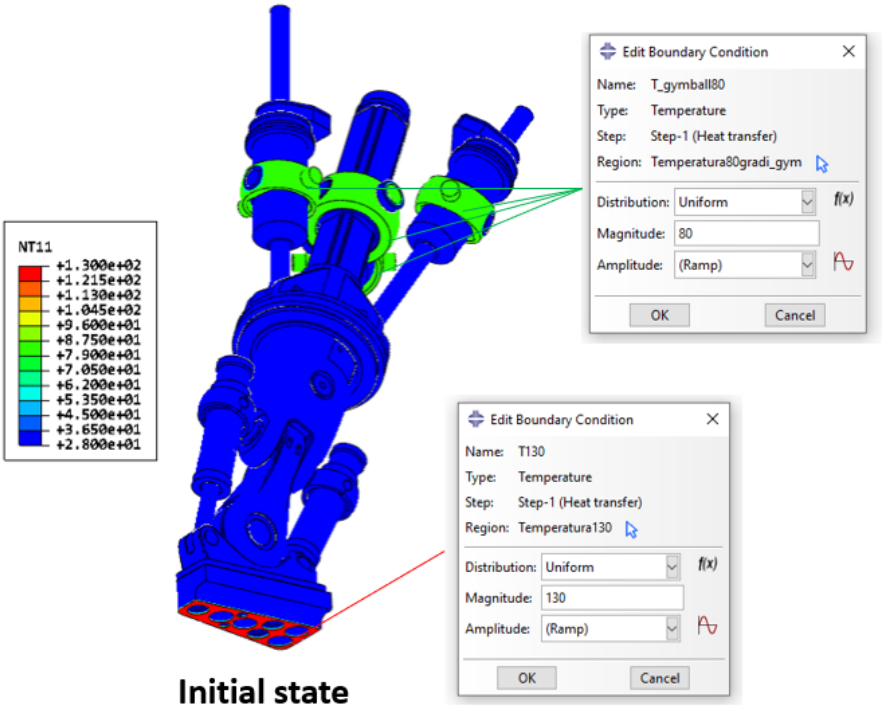

Figure 104 – BCs applied to the modeled components

11.5 Initial conditions

Finally, the rest of the Mover body was considered at 28 [°C], representing its starting condition at the time of insertion into the vacuum chamber.

11.6 Interactions

The model interactions were primarily implemented in the form of *TIE* contacts [42], which constrained the different parts of the Mover to behave as a single "rigid block". A contact classified as *TIE* is also known in the literature as a "*bonded contact*", meaning that the couples node have the same temperature. This is equivalent to a thermal contact having zero resistance at the interface between the surfaces in contact.

This approach was considered appropriate, considering that no *TCC* values are readily available to characterize the behavior of all the joints present in the model. Examples of some of these contacts are shown in *Figure 105* e *Figure 106*:

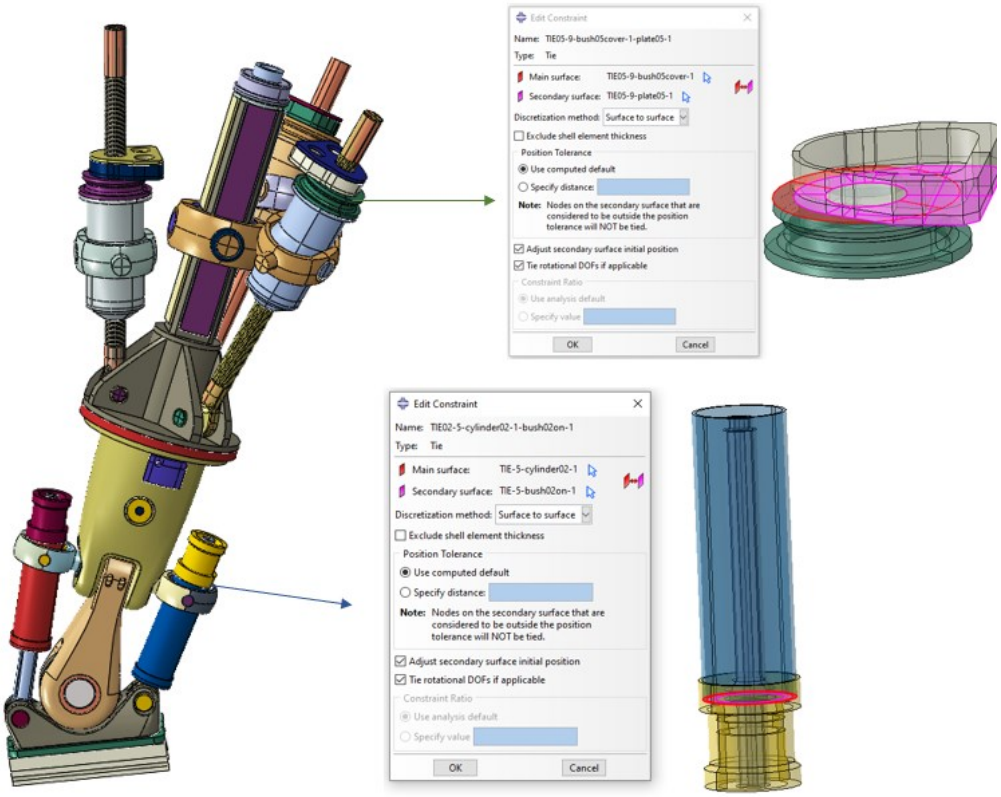

Figure 105 – Examples of TIE interactions between the actuators' subcomponents

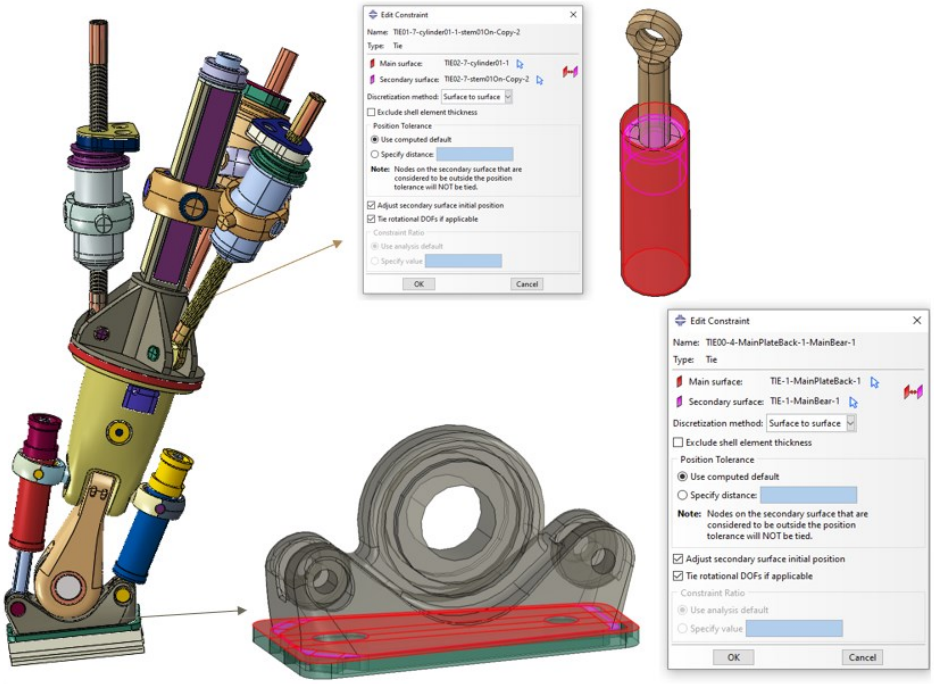

Figure 106 – Examples of TIE interactions between the bearing housing and the actuators' subcomponents (2)

Within this section, the convective condition was also defined, imposing a heat transfer coefficient initially set to 8 [W/m²K]. Although this value is slightly lower than that used in the simplified model (10 [W/m²K]), it was considered consistent with the real conditions and represents a first modeling approach. *Figure 107* shows the area of the Mover immersed in the vacuum chamber, subject to natural convection induced by the surrounding environment.

11.7 Loads

Regarding the thermal loads, the analysis considered exclusively the heat generation from the motors present in the model. These motors are located along the Mover's shafts, except for the central main shaft. In total, five motors were modeled in a simplified manner (*Figure 108*), one for each of the secondary shafts.

Two distinct scenarios were considered:

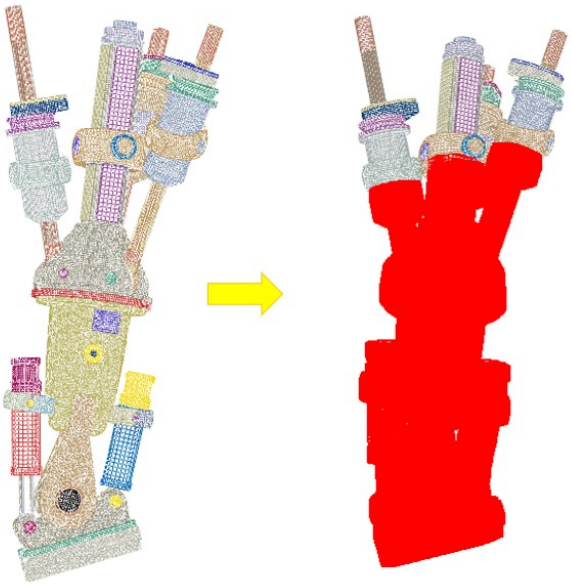

Figure 107 – Surface exposed to the convective heat exchange

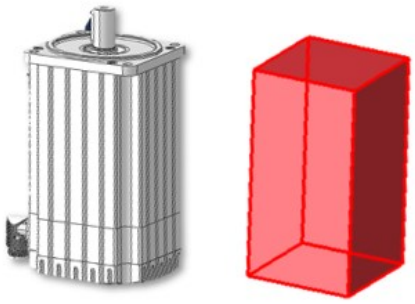

Figure 108 - Detail on the simplification performed regarding the generic engine block

- Case 1: the thermal power corresponding to half of the maximum power (5.03 kW) was uniformly distributed across the five motors;
- Case 2: the entire power was concentrated on a single motor, specifically on one of the two lower shafts, in order to analyze the localized effect of heat generation. This setup aims to represent the worst-case local thermal load on one shaft, allowing us to observe how heat builds up and transfers in that area.

These analyses are a direct continuation of the preliminary studies conducted in the previous chapters on the simplified model, where the model's sensitivity to heat generation was evaluated.

In conclusion, due to the lack of additional design data regarding the power output of the motors during the operational conditions of the *RM*, the simulations were carried out over a time span of 3 hours. During this period, the motors operated in alternating on-off cycles, each lasting 30 minutes. This approach was arbitrarily chosen to represent a more realistic operational cycle, as it would be unlikely for the motors to operate continuously (at max. Power) for several hours. However, the chosen cycle pattern is purely illustrative and does not yet reflect the actual operating strategy, which has not yet been defined. The temporal pattern of these cycles is illustrated in the *Figure 109*.

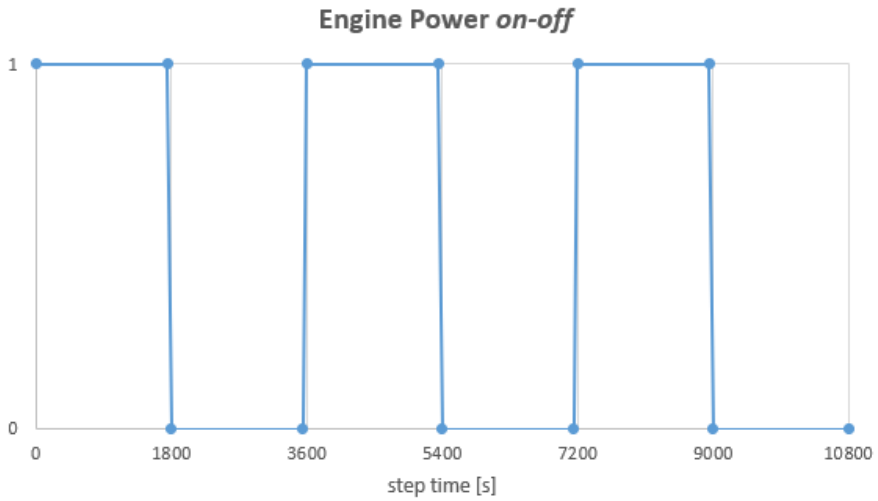

Figure 109 – Engine load cycles considered during the RM operating phase

11.8 Results

The *FE* analyses performed on the actual *RM* model produced results consistent with those expected from the preliminary analyses conducted on the simplified models, confirming the early predictions.

The main results of the simulations are described in the next paragraphs.

11.8.1 Steady-state analysis

Specifically, starting with the steady-state simulation of the problem (*Figure 110*): it can be observed that the area affected the most by heat

exchange with the Breeding Blanket (*BB*) is limited to the lower part of the *RM*, close to the contact zone. Overall, the Mover reaches a temperature of 80 [°C], as "imposed" by the convective condition, while the area closest to the BB tends toward 130 [°C].

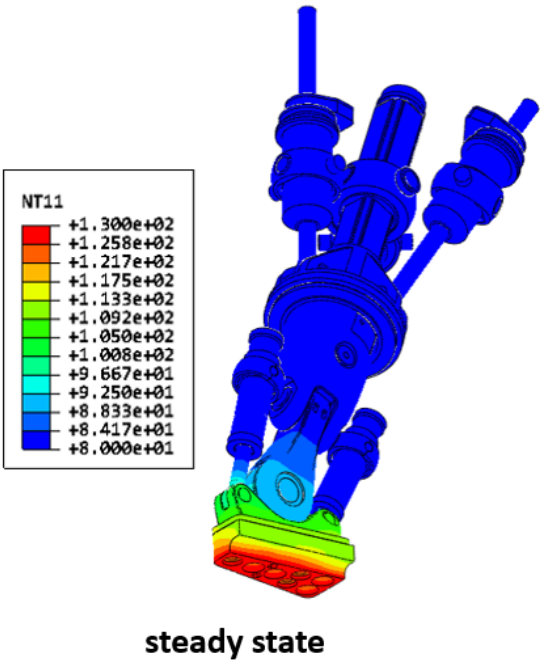

Figure 110 – Results in terms of nodal temperatures [°C] under steady-state conditions

11.8.2 3h Transient analysis

A first transient analysis was carried out over a duration of three hours for the model under study, and the results (*Figure 111*) do not yet show a completely uniform temperature distribution. *Figure 112* shows the temperature variation of the highlighted node, which represents an average temperature of the model. After three hours of exposure in the 80 [°C] environment, the temperature of the intermediate area of the *RM* is approximately 40 [°C].

An additional important piece of information is provided by *Figure 113*, which analyzes the thermal power entering the Mover as a result of prolonged contact with the *BB* at 130 [°C]. It can be observed that the power, initially increasing, reaches a maximum value of 3.26 [kW] at around 6000 seconds, and then begins to decrease. This delay in reaching the peak incoming heat

flux is due to the time required for the lower part of this component to heat up, while the subsequent decrease in power is caused by a slowdown in the increase of the average temperature, resulting in a reduced thermal gradient across the plate. This information could be crucial for future analyses aimed at designing a supplementary cooling system, thereby keeping the *RM* temperatures within lower and more acceptable ranges.

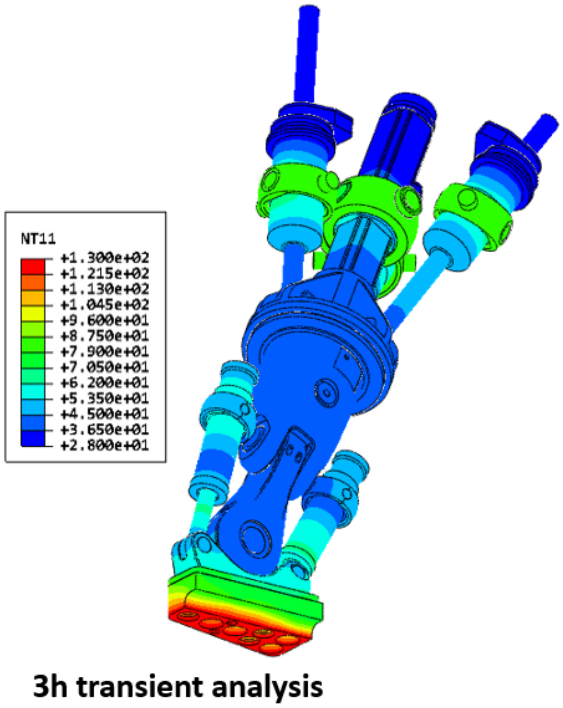

Figure 111 – Temperature distribution [°C] in the model following a 3 hour transient analysis

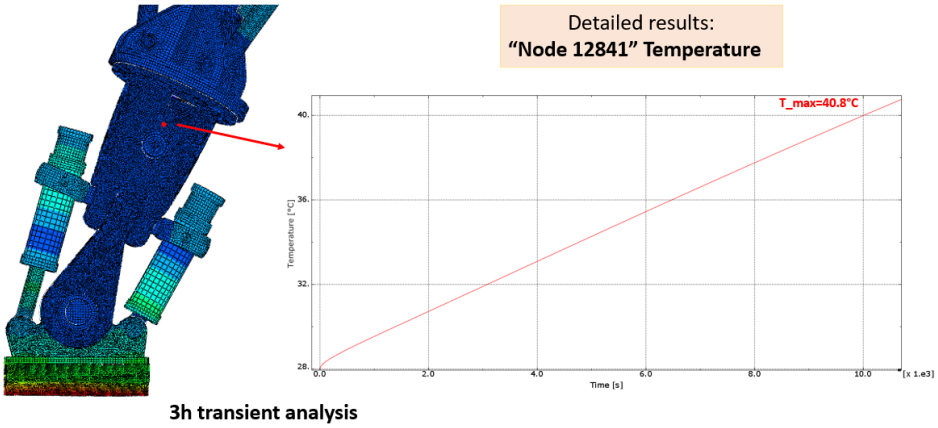

Figure 112 – Temperature distribution [°C] at the midpoint of the model

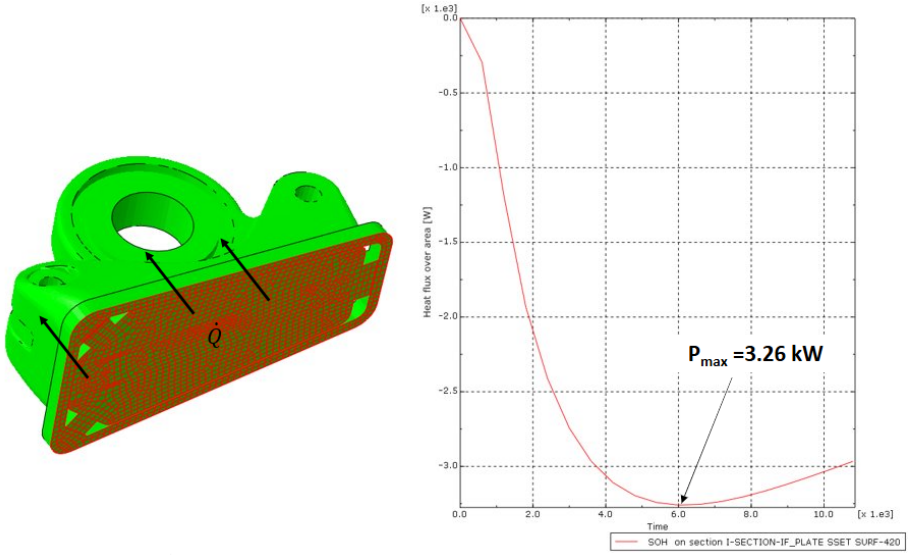

Figure 113 – Detail of the heat flux entering from the contact with the BB

11.8.3 0.5h Equivalent transient analysis

As was done in the previous chapters for the simplified model, the full model also employs significantly reduced mass densities to observe the evolution of the model's average temperature over time. This temperature, given the considerable distance from the contact area, will stabilize (as predicted by the steady-state analysis: §10.1) at a value slightly above 80 [°C], driven by the external environmental temperature. As expected, reducing the

mass density significantly shortens the temperature rise time, allowing the transient behaviour to be observed more quickly.

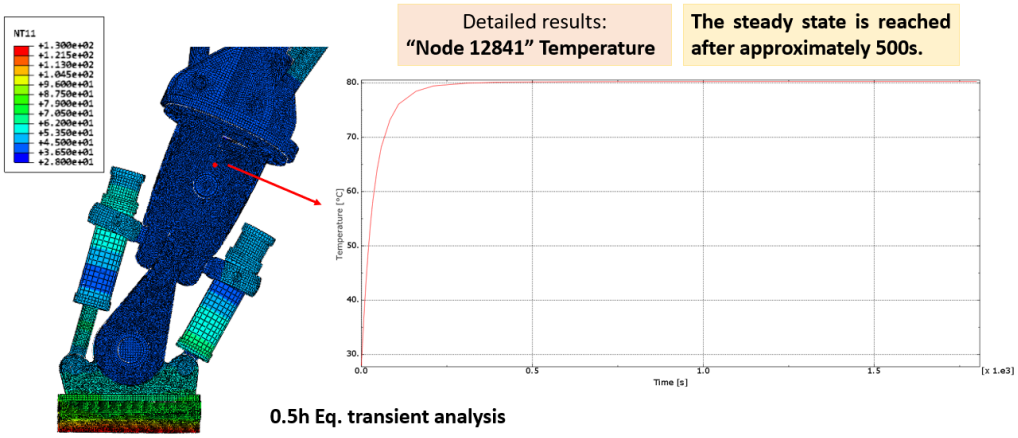

Figure 114 – Temperature distribution [°C] at the midpoint of the equivalent model

11.8.4 Film coefficient as a function of temperature

This section presents the results of the analysis carried out considering a temperature-dependent convective heat transfer coefficient (*Figure 115*), similarly to what was shown in §9. As a result of this modification, the convective heat transfer is slightly reduced, since the coefficient *h* takes lower values, compared to the 8 [W/m²K] used previously.

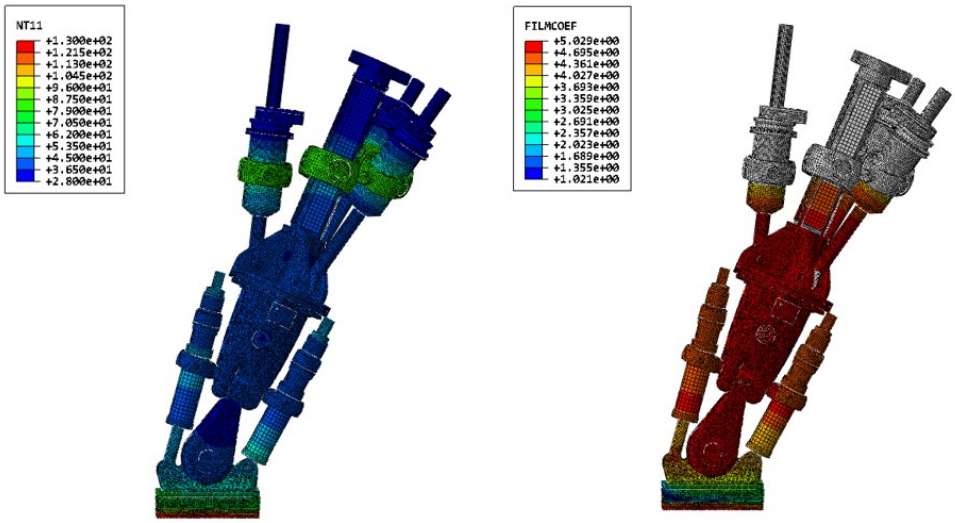

Figure 115 – Results in terms of nodal temperatures [°C] and h(T) [W/m²K]

At the midpoint of the central bell (shown in *Figure 112* and *Figure 114*) a slight decrease in temperature is observed, from 40.8 [°C] to 36.7 [°C] (*Figure 116*).

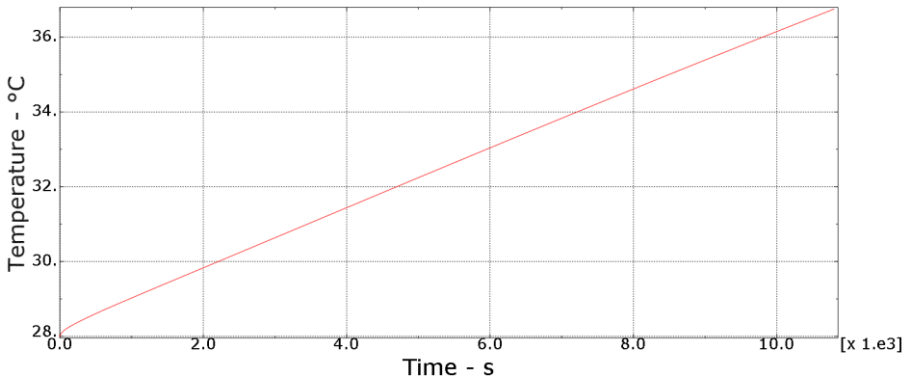

Figure 116 – Temperature evolution [°C] at the midpoint of the model

It should be noted that the results just presented are very similar to those shown in *Figure 95*, obtained from the simplified model.

11.8.5 Thermal Insulation Analysis

Figure 117 shows how the insulating layer is incorporated into the model and how the *BB* has been partially modeled. The layer is therefore positioned between the plate at the base of the *RM* and the component shown below, which represents a part of the *BB*. Two thermal contacts were modeled as already described in the chapter dedicated to the simplified analysis. The material used is G-10-Cr, a composite material based on epoxy resin reinforced with glass fiber, widely used in nuclear and cryogenic applications due to its excellent insulating properties (*Table 5*).

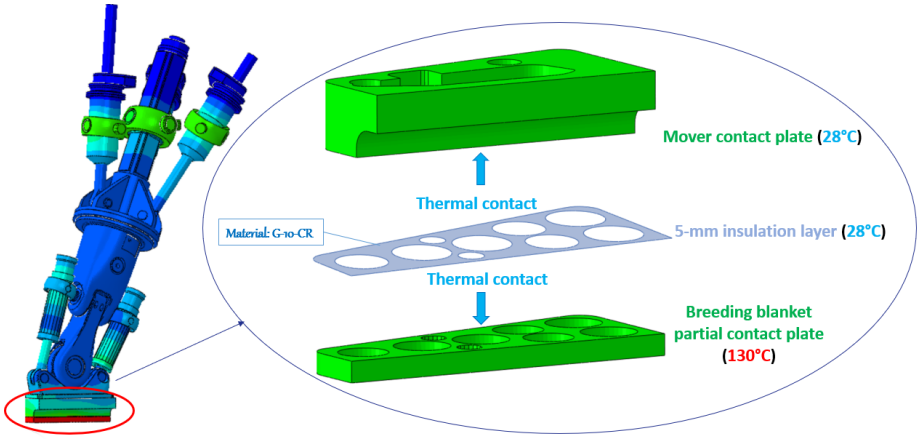

Figure 117 – Model configuration with the addition of the insulating layer

The *FE* analysis (*Figure 118*) shows that the effect of the 5 [mm] insulating layer is quite significant with respect to the temperatures developing in the contact plate. In fact, in the coldest area of the plate, the temperature decreases from approximately 64 [°C] to 48 [°C], considerably delaying its heating.

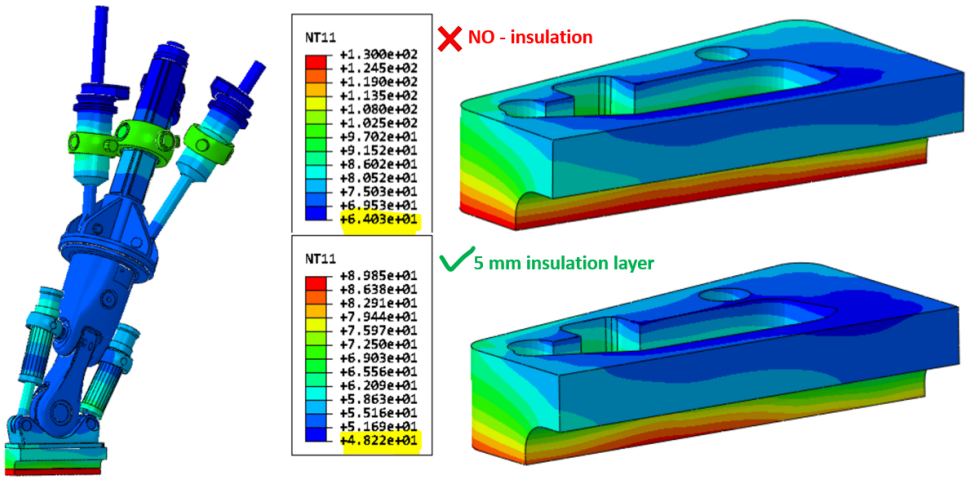

Figure 118 – Effect of the insulating layer on the local temperature [°C] of the contact plate

On a global level, however, this effect is not as significant, as predicted by the results in *Figure 100* and confirmed by the results in *Figure 119*. Here, the central bell and one of the two lower shafts are analyzed in detail. The

temperatures of these two components show ranges in which the minimum and maximum values are almost identical, with only very slight fluctuations.

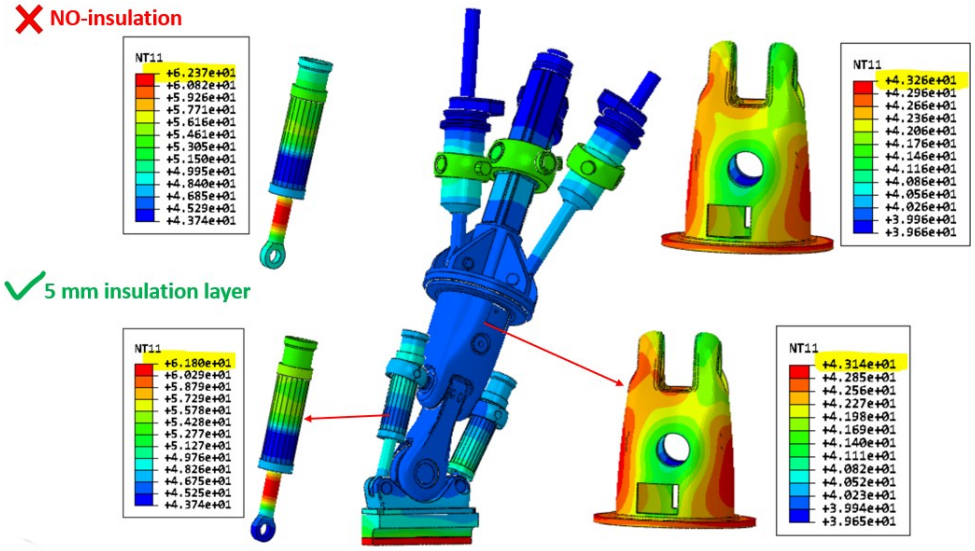

Figure 119 – Effect of the insulating layer on the overall temperature [°C] of the model

11.8.6 30h Transient analysis

Another simulation that confirms the predictions from the simplified analyses is the 30-hour transient analysis. From the graph in *Figure 120*, it can be observed that the curve representing the midpoint of the model reaches, after the indicated time, a temperature just below 70 [°C]. This result is fully consistent with what was previously calculated and shown in *Figure 90*, where the average temperature of the model reached 63 [°C]. The slight difference is due to the substantial difference in complexity between the two models, and because the point on the central bell considered as the midpoint of the real model was chosen arbitrarily, being in the central area of the model and far from the region where the *BCs* are applied.

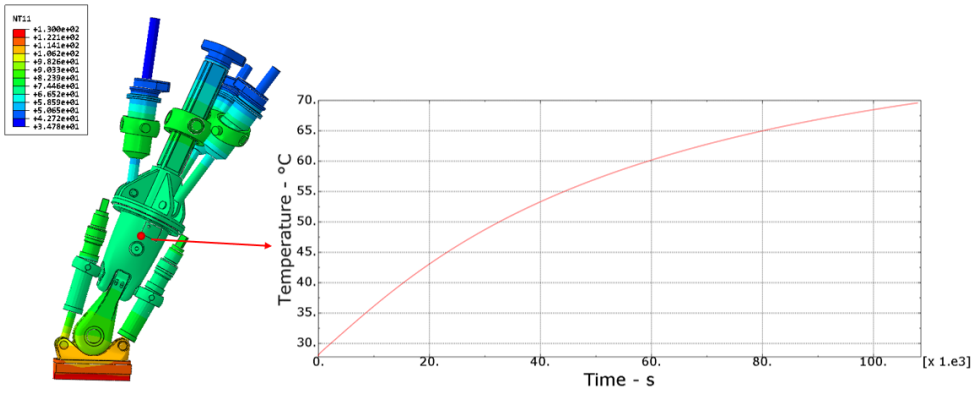

Figure 120 - Temperature distribution [°C] at the midpoint of the model

11.8.7 Analysis Including the motors' heat generation

In this final phase, the *RM* configuration including the blocks representing the motors of the various actuators was considered. Specifically, five motors were inserted: three on top of the three upper shafts and two above the lower shafts. Two different cases were studied, as introduced in §11.7. Before proceeding with the analysis of Case 1, in which the power is distributed across the various motors, a simple approximate calculation was performed to verify the validity of the simulation. With the motors still turned off, the heat power entering each motor block was evaluated by integrating the heat flux over the external surfaces of the motor. The results obtained from the *FE* analysis are reported in *Figure 121*. It can be observed that the curve spans negative values, which is understandable given that the motor tends to heat up due to convection in a high-temperature environment. Specifically, its midpoint reaches 55 [°C] after three hours. To confirm these results, the following calculation is performed (eq. (32)):

$$P = m \cdot c_p \cdot \Delta t = 21 \cdot 485 \cdot (55 - 28) = 25.4\ kW \qquad (32)$$

This simple calculation is in good agreement, on average, with the *FE* model output showed in *Figure 121*, confirming the reliability of the simulation approach. This calculated value represents the energy entering the engine block per unit of time and thus provides an estimate of the magnitude of the heat fluxes that must be removed by any auxiliary cooling circuits to prevent a temperature rise.

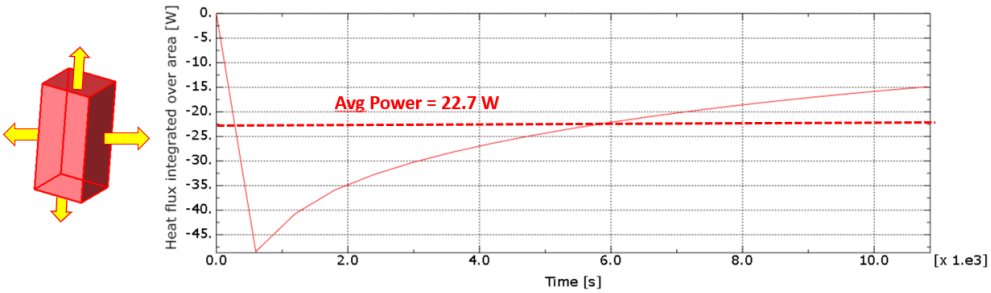

Figure 121 – Power output from a single engine block in the case without heat generation

Proceeding with the calculation of the model with distributed heat generation across the five motors, the results are reported in *Figure 122*.

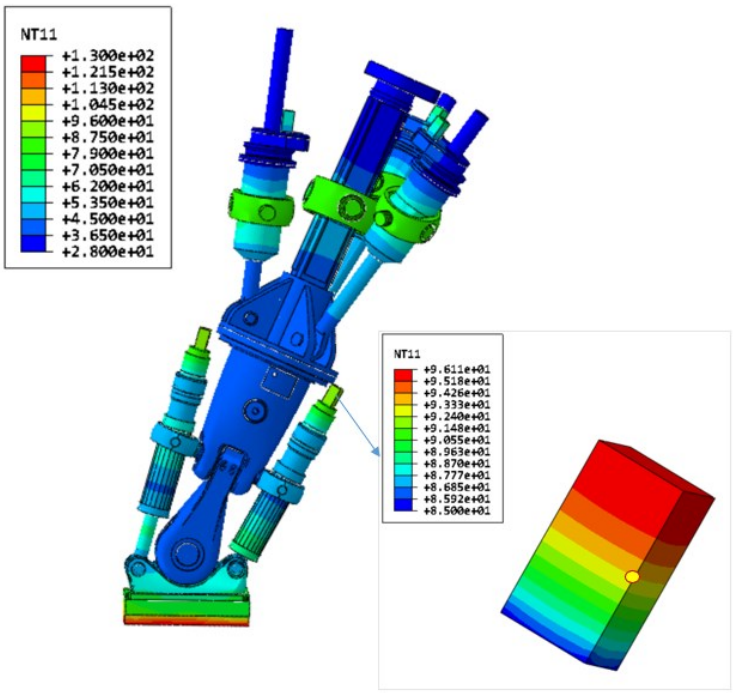

Figure 122 – Results in terms of temperatures [°C] obtained in the configuration with distributed power

From the figure, it can be seen that over the course of three hours, and according to the load profile shown in *Figure 109*, the motor exhibits a temperature ranging between 85 and 96 [°C]. The point of interest is located at mid-height of the motor and highlighted in yellow, representing its

midpoint: extracting the temperature at this point over the three-hour load period, *Figure 123* shows the comparison with the initial configuration, which did not account for the motor's heat generation

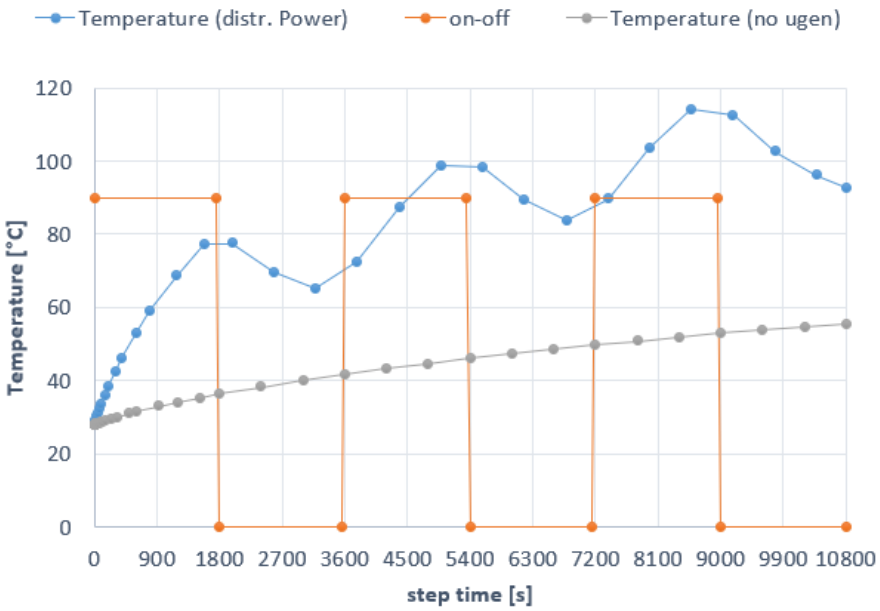

Figure 123 – Comparison of temperatures at the midpoint of the motor for the distributed power case and the initial case without heat generation

Following the first 30 minutes load cycle, for example, the temperature rises from 28 to 78 [°C]. During the motor shutdown phase, since the temperature is close to that of the surrounding environment, the convective heat flux is very low, and conduction predominates, resulting in a heat flow leaving the engine and directed toward the cooler components in contact with it. Consequently, the engine block undergoes natural cooling down to approximately 65 [°C].

The effect of distributed heat generation at the global level has virtually no impact, and the temperature evaluated at the midpoint of the central bell (*Figure 124*) remains almost unchanged compared to the case without heat generation (*Figure 112*).

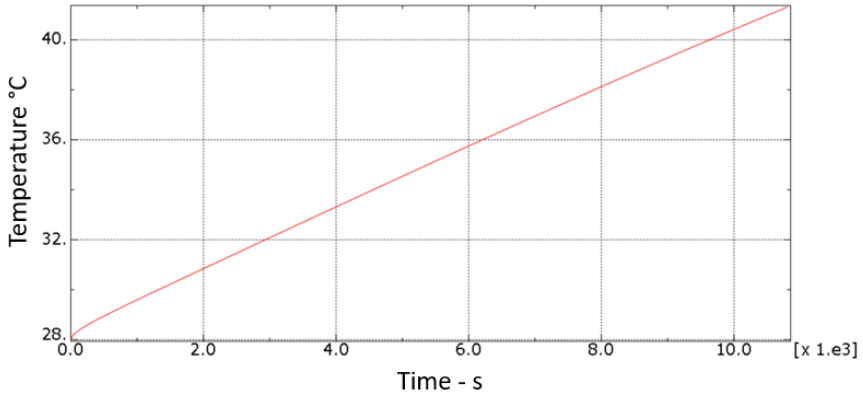

Figure 124 – Temperature evolution at the midpoint of the central bell housing (distributed power case)

Subsequently, the case in which the overall generation is localized in a single motor block was analyzed. The results are shown in *Figure 125*. After the three-hour transient, the temperatures locally reached as a result of the application of the thermal "*on-off*" cycles are excessively high (over 250 [°C]).

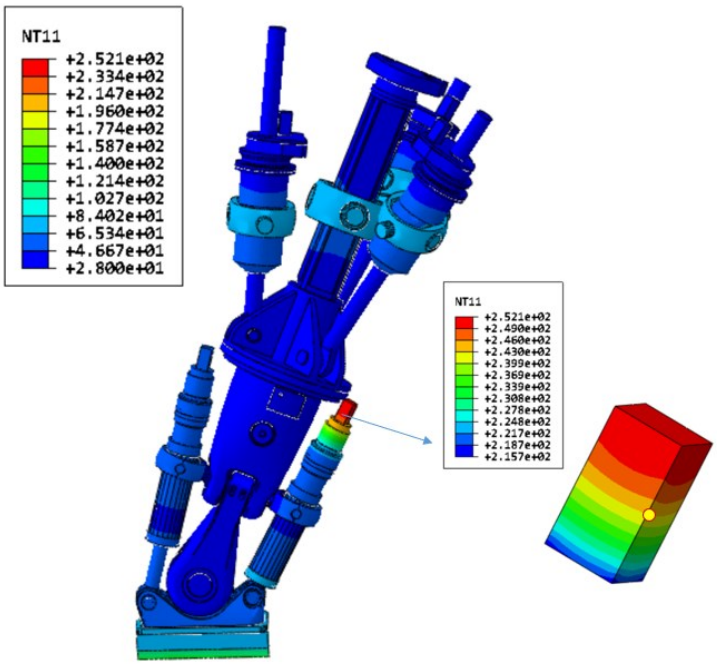

Figure 125 - Results in terms of temperatures [°C] obtained in the configuration with localized power

Below, similarly to what was done for the calculation with distributed power, the comparison graph with the case in which the model is not affected by thermal generation is reported (*Figure 126*). It can also be observed that the temperature peaks reached over the three-hour period exceeded 350 [°C], making this configuration non-functional and unrealistic.

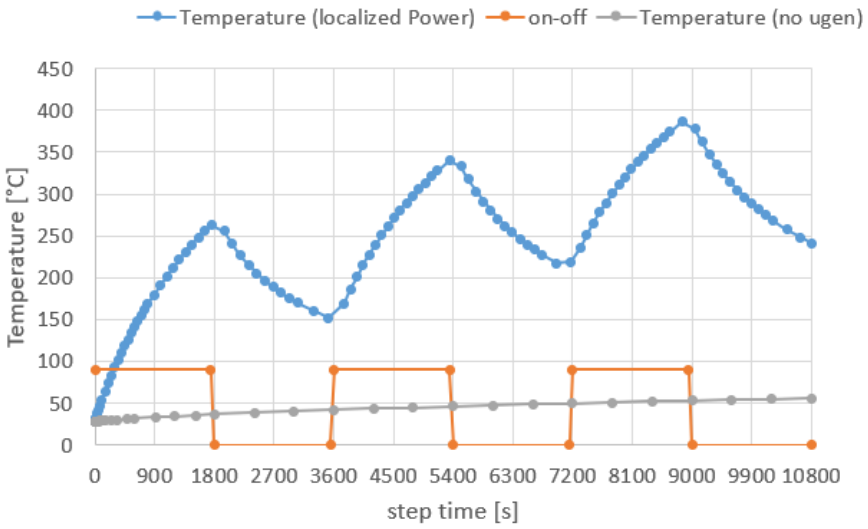

Figure 126 - Comparison of temperatures at the midpoint of the engine for the localized power case and the initial case without heat generation

Even in the case where the power is localized, no temperature increase is observed at the midpoint of the central bell, so the issue to be addressed concerns only the area adjacent to the engine block.

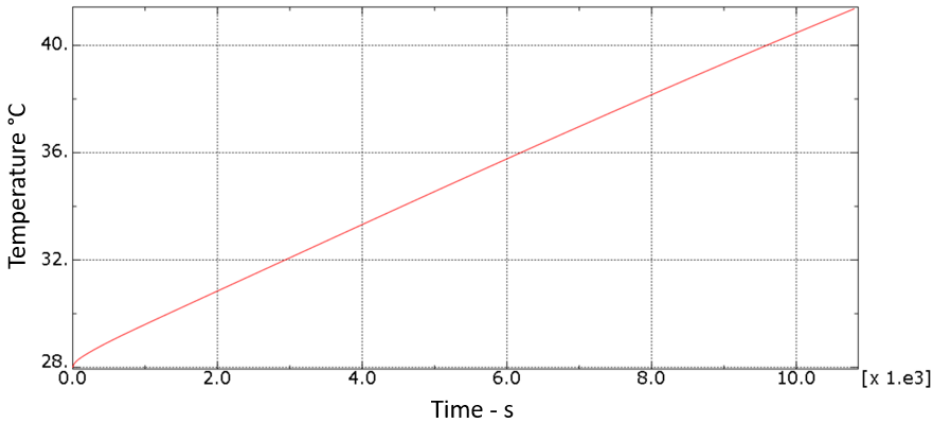

Figure 127 – Temperature evolution at the midpoint of the central bell housing (localized power case)

These analyses represent preliminary approaches useful for gaining an understanding of the thermal loads involved. With a view to the potential design of an auxiliary cooling circuit for the *RM* under study, it is in fact important to be aware of the temperatures reached by the operating system both under standard operating conditions and in more critical scenarios. It should be noted that the on–off cycle considered is purely arbitrary. The results suggest that the motors should not operate at full power for extended periods without adequate cooling.

12. Conclusions

In this work, two complementary methodological developments were carried out in support of the structural and thermal assessment of *DEMO* reactor components.

In the first part, a numerical procedure for the structural and fracture assessment of the *DEMO* divertor in unirradiated conditions was developed. The approach combined global *FE* modelling and submodeling techniques implemented in *ANSYS* with Linear Elastic Fracture Mechanics (*LEFM*) simulations performed using *FRANC3D*.

A preliminary analysis on representative single load cases allowed the identification of potentially critical regions characterized by high principal stress concentrations and, therefore, susceptible to crack initiation. Among the scenarios investigated, the thermal load case proved to be the most demanding, leading to significantly higher *SIF* values compared to the pressure load case.

Subsequently, a *combined* load case was analyzed, accounting for both thermal and pressure effects. The first load step considered only the pressure contribution, whereas the second also incorporated the thermal load. This configuration shows that the structure experiences a constant *SIF* induced by the pressure load, superimposed with an alternating thermal component.

The subsequent fatigue analysis, performed using Paris' law, indicated that several thousand on–off cycles would be required for a crack to propagate by only one millimeter, confirming the structural robustness of the divertor under the investigated conditions in the single load cases. Nevertheless, this outcome must be interpreted cautiously, as it is based on partial loading conditions and assumes a pre-existing critical crack with a depth equal to one quarter of the

reference wall thickness. The combined load case is then evaluated in a larger crack range until 3 millimeters of depth.

An additional analysis performed on the *IVT* of the *DEMO* divertor investigated the effect of multiple cracks in two potentially critical adjacent zones, showing comparable *SIF* values at both locations and, consequently, similar crack growth behaviour.

The study thus provides a first methodological framework for more refined assessments, to be further extended to include irradiation effects, more complex combined load cases, and different crack geometries or more detailed multiple-crack configurations.

In the second part, a dedicated thermal analysis methodology was developed for the *HKM* of *DEMO*, aimed at evaluating its operational reliability and supporting future design optimization.

In this study, a thermal analysis methodology was developed for the *BB* handling system of the *DEMO* reactor, with the aim of assessing its operational reliability and supporting its future design. The adopted approach followed a progressive path, starting from simplified analytical models up to three-dimensional *FE* simulations, allowing for the validation of the initial assumptions and the quantification of thermal phenomena under realistic conditions. The main results can be summarized as follows:

Model validation: The simplified analytical models provided predictions in good agreement with the *FE* simulations, confirming the robustness of the methodological approach.

Identification of critical times: Transient analyses showed that the mover's average temperature exceeds the critical threshold of 40 [°C] (critical to achieve the performance of the mechanical actuators) after about 7 hours, when considering a constant convective coefficient, while the same threshold is only reached after 14 hours when using a more realistic temperature-dependent heat transfer coefficient. After 30 hours of exposure to the *VV* ambient, the average temperature tends to stabilize around 60–70 [°C], well above the initial value of 28 [°C] imposed to the *RM*. Here too, the results obtained from the simplified and the realistic model are very similar, with only negligible deviations due to the different level of complexity of the two models. The effect of the RM's mass variation is the most significant among all the parameters analyzed.

Effect of the motors: The introduction of internal heat generation highlighted contrasting scenarios. While awaiting a more precise definition of

the actual motor load cycles to better estimate the resulting local and global heating, a first approach was carried out with analyses assuming motors operating at 50% of the stall power (5 [kW]) distributed over five units: the resulting temperatures remained limited, locally exceeding about 100 [°C]; conversely, concentrating the same power on a single motor the local temperature peaks above 350 [°C], which is entirely incompatible with the required performance and clearly indicates the need for dedicated cooling systems.

Mitigation through insulation: the addition of a 5 [mm] insulating layer, made of fiberglass material (G-10-CR or similar) reduced local temperatures in the *BB* contact area from about 64 [°C] (no insulation, metal to metal contact) to 48 [°C], significantly delaying the thermal rise, while having a limited impact on the overall behavior (average *RM* temperature ≈ 40.8 [°C]).

Effect on the structural strength of the *RM* components: the max. temperature values calculated for the operating scenarios considered in this work are compatible with the typical range considered acceptable for structural steel. Only a minor strength reduction shall be accounted for in the worst-case scenario.

These findings have not only clarified the operating thermal conditions of the system but have also provided objective criteria for its design optimization. In particular, the results offer concrete support for defining safety margins, assessing the need for auxiliary cooling systems, and selecting the most suitable materials or geometric configurations. In perspective, this work thus provides a solid methodological and numerical basis for future developments, such as thermo-structural analyses, evaluations under dynamic conditions, and long-term reliability studies. The proposed approach therefore contributes to enhancing the robustness of the remote maintenance system and, more generally, to improving the safety and efficiency of *DEMO* reactor maintenance operations.

13. References

[1] World Economic Forum (2024) Fostering effective energy transition 2024. World Economic Forum.

[2] TotalEnergies (2024) Energy Outlook 2024: TotalEnergies sets out its vision for energy transition by 2050.

[3] ITER Organization (2023) Advantages of fusion energy.

[4] ITER Organization. (2023). About ITER. ITER.

[5] International Atomic Energy Agency. (2021). *Magnetic fusion confinement with tokamaks and stellarators*. IAEA Bulletin.

[6] F. Romanelli and others, A Roadmap to the Realisation of Fusion Energy. 2012.

[7] Credit © ITER Organization, http://www.iter.org/

[8] Luce, T. (2021) ITER powers ahead. CERN Courier, 3 Nov.

[9] ITER Organization (2013) Korea aims at completing a DEMO by 2037.

[10] Federici, G. et al. (2017) European DEMO design strategy and consequences for materials. Nuclear Fusion, 57(9), 092002.

[11] Eade, T. et al. (2017) Activation and decay heat analysis of the European DEMO blanket concepts. Fusion Engineering and Design, 124, 1241–1245.

[12] You, J. H. et al. (2022) Divertor of the European DEMO: Engineering and technologies for power exhaust. Fusion Engineering and Design, 175, 113010.

[13] Fursdon, M., Li, M. and You, J. H. (2019) Towards reliable design-by-analysis for divertor plasma facing components - Guidelines for inelastic assessment (part I: unirradiated). Fusion Engineering and Design, 147, 111234.

[14] Fursdon, M. and You, J. H. (2020) Towards reliable design-by-analysis for divertor plasma facing components - Guidelines for inelastic assessment (part II: irradiated). Fusion Engineering and Design, 160, 111831.

[15] Muscat, M., Mollicone, P., Mantel, N. and You, J. H. (2025) Insight into the structural integrity assessment of the European DEMO fusion reactor divertor (Part I: General discussion). University of Malta.

[16] De Meis, D. and Mazzone, G. (2016) Application of Eurofer97 steels for DEMO divertor cassette irradiated at temperature below 350 °C. ENEA Report RT-2016-21-ENEA

[17] Pitike, K. C., Robin, I. K., El Atwani, O., Setyawan, W. et al. (2025) Computational design of ductility and phase stability in W–Ti–V–Cr refractory multiprincipal element alloys for fusion applications. Scientific Reports, 15, 40057

[18] Gilbert, M. R., Dudarev, S. L., Nguyen-Manh, D., Zheng, S., Packer, L. W. and Sublet, J.-Ch. (2013) Neutron-induced dpa, transmutations, gas production, and helium embrittlement of fusion materials. Journal of Nuclear Materials, 442, S755–S760

[19] Castrovinci, F. M. et al. (2025) Thermofluid-Dynamic Assessment of the Dual Cooling Scheme EU-DEMO Divertor Cassette. Fusion Engineering and Design, 214, 114903

[20] Marzullo, D. et al. (2024) Selection of EU-DEMO divertor operating condition: design space and power exhaust capabilities. Fusion Engineering and Design, 203, 114467.

[21] Maffucci, A. (2022) Electromagnetic Analysis for Divertor Assembly.

[22] AFCEN (2022) RCC-MRx design and construction rules for mechanical components of nuclear installations.

[23] SDC-IC, ITER (2013) Appendix A, Materials Design Limit Data.

[24] Mantel, N. (2023) DIV-DEMO.S.1-T026-D001 Preload assessment of divertor cassette.

[25] Giannella, V., Campagnolo, A., Citarella, R. and Meneghetti, G. (2024) Crack propagation simulations in steel welded joints for off-road vehicles. Procedia Structural Integrity, 66, 71–81

[26] You, J. H., Li, M. and Zhang, K. (2021) Structural lifetime assessment for the DEMO divertor targets: Design-by-analysis approach and outstanding issues. Fusion Engineering and Design, 164, 112203.

[27] FRANC3D (2021) V7 Training Part 7: Crack Growth.

[28] Wawrzynek, P. A., Carter, B. J. and Banks-Sills, L. (2005) The M-Integral for Computing Stress Intensity Factors in Generally Anisotropic Materials. NASA/CR-2005-214006.

[29] Erdogan, F. and Sih, G. C. (1963) On the Crack Extension in Plates Under Plane Loading and Transverse Shear. Journal of Basic Engineering, 85(4), 519–525.

[30] Zhang, K., Mantel, N. and You, J.-H. (2023) Dynamic structural response of DEMO divertor under electromagnetic loading. Fusion Engineering and Design, 187, 113375

[31] EUROfusion (2020) Materials property Handbook – EUROFER97

[32] Spätig, P. et al. (2007) Plastic flow properties and fracture toughness characterization of unirradiated and irradiated tempered martensitic steels. Journal of Nuclear Materials, 367–370, 527–532.

[33] Nöhring, W. et al. (2025) Prediction of the crack propagation direction in combined static-cyclic multi-axially loaded cruciform specimens. Engineering Fracture Mechanics, 325, 111296

[34] Amato, D., Mayrhofer, L., Robl, C., Dhondt, G. and Citarella, R. (2023) Prediction of the crack growth propagation direction in non-proportional mixed-mode missions. International Journal of Fatigue, 166, 107233

[35] Giannella, V. et al. (2025) Fatigue life assessment of steel specimens with weld ends and complex cracking scenarios by crack propagation numerical analyses. International Journal of Fatigue, 200, 109125.

[36] Amato, D., Federico, L., Armentani, E. and Citarella, R. (2024) Limits of applicability of LEFM: numerical investigation on the crack-tip-yielding in a hollow-cylindrical specimen. Procedia Structural Integrity, 52, 1–11.

[37] Knitel, S. (2018) Investigations and numerical modeling of mechanical properties of tempered martensitic steel Eurofer97 at various loading rates, temperatures and after spallation irradiation. Doctoral thesis, École Polytechnique Fédérale de Lausanne, EPFL

[38] Incropera, F. P., DeWitt, D. P., Bergman, T. L. and Lavine, A. S. (2007) Fundamentals of Heat and Mass Transfer, 6th Edition, Chapter 5 – Transient Conduction.

[39] Incropera, F. P., DeWitt, D. P., Bergman, T. L. and Lavine, A. S. (2007) Fundamentals of Heat and Mass Transfer, 6th Edition, Chapter 9 – Free Convection

[40] Incropera, F. P., DeWitt, D. P., Bergman, T. L. and Lavine, A. S. (2007) Fundamentals of Heat and Mass Transfer, 6th Edition, Appendix A – Thermophysical properties of matter, Table A.4, p.941.

[41] Aurubis AG (2024) Material Datasheet CuSn5 (C51000 / PNA 285). Aurubis AG

[42] Dassault/Simulia Abaqus (2020) - Analysis User's Guide